AFRL-RB-WP-TR-2008-3031

UNIFIED KINETIC APPROACH FOR SIMULATION OF GAS FLOWS IN RAREFIED AND CONTINUUM REGIMES

Vladimir Kolobov, Robert Arslanbekov, Sami Bayyuk, Vladimir Aristov, Anna Frolova, Sergey Zabelok, and Filix Tcheremissine

CFD Research Corporation

JUNE 2007
Final Report

THIS IS A SMALL BUSINESS INNOVATION RESEARCH (SBIR) PHASE II REPORT.

STINFO COPY

AIR FORCE RESEARCH LABORATORY
AIR VEHICLES DIRECTORATE
WRIGHT-PATTERSON AIR FORCE BASE, OH 45433-7542
AIR FORCE MATERIEL COMMAND
UNITED STATES AIR FORCE

NOTICE AND SIGNATURE PAGE

*//Signature//

Eswar Josylua

//Signature//

MATTHEW BURKINSHAW, CAPT USAF
Deputy Chief
Computational Sciences Branch

//Signature//

Michael J. Stanek, Ph.D.
Technical Advisor
Aeronautical Sciences Division

CFDRC

**Better Decisions, Better Products
Through Simulation & Innovation**

Mr Eswar Josyula
AFRL/VAAC, Bldg. 146, Room 225
2210 Eighth Street, Area B
Wright-Patterson AFB, OH 45433

Subject: Contract Number FA8650-04-C-3404, Phase II SBIR

Dear Mr. Josyula:

CFD Research Corporation hereby waives its SBIR Data Rights to all contents of the final report
for subject contract. The Government is granted an unlimited nonexclusive license to use,
modify, reproduce, release, perform, and display or disclose this report and the data contained
herein.

The report has been reviewed and we grant approval for public release, distribution unlimited.

Sincerely,

Dr Ashok Singhal,
President

REPORT DOCUMENTATION PAGE			*Form Approved* *OMB No. 0704-0188*

1. REPORT DATE *(DD-MM-YY)*	2. REPORT TYPE	3. DATES COVERED *(From - To)*
July 2007	Final	01 July 2004 – 01 July 2007

4. TITLE AND SUBTITLE	5a. CONTRACT NUMBER
UNIFIED KINETIC APPROACH FOR SIMULATION OF GAS FLOWS IN RAREFIED AND CONTINUUM REGIMES	FA8650-04-C-3404
	5b. GRANT NUMBER
	5c. PROGRAM ELEMENT NUMBER 0605502, 602201

6. AUTHOR(S)	5d. PROJECT NUMBER
Vladimir Kolobov, Robert Arslanbekov, Sami Bayyuk, Vladimir Aristov, Anna Frolova, Sergey Zabelok, and Filix Tcheremissine	A02W
	5e. TASK NUMBER
	5f. WORK UNIT NUMBER 0G

7. PERFORMING ORGANIZATION NAME(S) AND ADDRESS(ES)	8. PERFORMING ORGANIZATION REPORT NUMBER
CFD Research Corporation 215 Wynn Drive Huntsville, AL 35805	8572-F

9. SPONSORING/MONITORING AGENCY NAME(S) AND ADDRESS(ES)	10. SPONSORING/MONITORING AGENCY ACRONYM(S)
Air Force Research Laboratory Air Vehicles Directorate Wright-Patterson Air Force Base, OH 45433-7542 Air Force Materiel Command United States Air Force	AFRL/RBAC
	11. SPONSORING/MONITORING AGENCY REPORT NUMBER(S) AFRL-RB-WP-TR-2008-3031

12. DISTRIBUTION/AVAILABILITY STATEMENT
Approved for public release; distribution unlimited.

13. SUPPLEMENTARY NOTES
This is a Small Business Innovation Research (SBIR) Phase II report. A letter waiving SBIR data rights is on file, and a digitally scanned copy is included in this report. Report contains color. PAO Case Number: WPAFB 07-0761, 21 Dec 2007.

14. ABSTRACT
This report was developed under a SBIR contract.

The objective of this effort was to develop a computation fluid dynamics tool for air and space flight. Flow fields characterized by the simultaneous presence of *continuum* and *rarefied* regimes arise in many important applications, ranging from re-entry of aerospace vehicles to micro-fluidics. In this Phase II SBIR Project, we have developed a Unified Flow Solver with adaptive mesh and algorithm refinement based on direct numerical solution of the Boltzmann equation coupled to kinetic schemes of gas dynamics. Our strategy allowed easy coupling of the continuum and Boltzmann solvers in a hybrid code with automatic domain decomposition. We have demonstrated the UFS capabilities for several one-component gas flows and have confirmed that the hybrid method results in significant savings by limiting expensive kinetic solutions only to the regions where they are needed. The UFS could automatically introduce or remove kinetic patches to maximize accuracy and efficiency of simulations. We have extended UFS to molecular gases with rotationally and vibrationally degrees of freedom and to multi-component reactive gas mixtures. It was demonstrated that the UFS methodology could provide an efficient solution to practical problems of polyatomic gas mixtures of different degrees of rarefaction.

15. SUBJECT TERMS
SBIR Report, Rarefied Gas Dynamics, Boltzmann Transport Equation, Direct Numerical Solution, Conservative Splitting Method, Automatic Domain Decomposition, Navier-Stokes Equations, Euler Equations, Re-Entry Problem, Upper-Atmospheric Flight, Microfluidics

16. SECURITY CLASSIFICATION OF:			17. LIMITATION OF ABSTRACT:	18. NUMBER OF PAGES	19a. NAME OF RESPONSIBLE PERSON (Monitor)
a. REPORT Unclassified	**b. ABSTRACT** Unclassified	**c. THIS PAGE** Unclassified	SAR	98	Eswar Josyula **19b. TELEPHONE NUMBER** *(Include Area Code)* (937) 904-4044

i

TABLE OF CONTENTS

LIST OF FIGURES

1. SUMMARY

This SBIR Phase II Project has produced a Unified Flow Solver (UFS) for Rarefied and Continuum Gas Flows by collaborative efforts of CFD Research Corporation and Dorodnizyn Computing Center of the Russian Academy of Sciences. The UFS separates the rarefied and continuum flow domains and selects appropriate solvers to combine the efficiency of continuum models with the accuracy of kinetic models. The Direct Numerical Solution (DNS) of the Boltzmann Transport Equation (BTE) is used in rarefied regions, while kinetic schemes of continuum fluid dynamics (CFD) are used elsewhere. Using similar numerical methods for the BTE and CFD solvers, employing adaprive mesh refinement technique and intelligent model selection algorithms attain the efficiency and numerical stability of the UFS.

This Final Report for Phase II work describes the UFS architecture, demonstrates the capabilities of the UFS for monatomic gas flows and UFS extensions to molecular gases and reactive gas mixtures. Using adaptive mesh and algorithm refinement methodology enables easy coupling of the kinetic and continuum models within a hybrid code. Using kinetic schemes for the continuum equations further facilitates the coupling. Several criteria for the continuum breakdown and domain decomposition into kinetic and continuum subdomains have been tested. The UFS code was parallelized using dynamic domain decomposition and dynamic load balancing among multiple processors and tested at several multi-processor systems.

We have demonstrated the UFS capabilities for several one-component gas flows and have confirmed that hybrid method can result in significant savings by limiting expensive kinetic solutions only to the regions where they are needed. During the simulation process, the UFS can automatically introduce or remove kinetic patches to maximize accuracy and efficiency of simulations. We have demonstrated the UFS capabilities for a wide range of applications from hypersonic external flows to low speed (subsonic) flows driven by temperature gradients.

We have extended the UFS to molecular gases with rotationally and vibrationally degrees of freedom and to multi-component reactive gas mixtures. Initial testing for mixtures of molecular gases has been performed. With further development, the UFS can offer an efficient solution to practical problems of polyatomic gas mixtures of different degrees of rarefaction.

The results of this project have been presented at several conferences and published in two journal articles. The UFS User Manual and several Tutorials have been prepared and can be delivered to potentials users.

2.   INTRODUCTION

A variety of gas flow problems are characterized by large variations in the density and other macroscopic characteristics of the gas. Examples of such problems include a gas in the gravitational field of a planet, where the density may vary by several orders of magnitude across the atmosphere, and a gas rotating at high speed in a spinning cylinder, with large density variations in the radial direction. Another class of flows is characterized by the presence of layers of relatively small extent that are embedded in larger (near-continuum) flow regions. In these layers, which are associated, for example, with shock waves, contact discontinuities, or shear or boundary layers, the state of the flow changes drastically over a relatively small distance. For space flight problems, the reduced density of the ambient gas at high altitudes increases the mean free path to such an extent that it becomes comparable to the dimensions of the space vehicle. During the reentry phase, such a vehicle encounters different flow regimes. At altitudes of 90 km and above, the Knudsen number is large, corresponding to a rarefied-gas regime. At altitudes below 70 km, the Knudsen number is smaller and the flow is well approximated by the continuum model using the Euler or Navier Stokes equations. For intermediate altitudes, in the transitional regime, the continuum flow equations cease to be valid in the boundary layers, but remain adequate in the far-field flow.

Whenever the characteristic length of the system (or the distance over which a gas state changes appreciably) becomes comparable with the mean free path, the classical continuum hydrodynamic description of gas flow becomes invalid. The non-equilibrium kinetic state that exists in those circumstances requires a full kinetic treatment, by solving the Boltzmann transport equation. Simulation of rarefied gas flows remains a challenging task. The rarefied gas dynamics is the synthesis of several fundamental problems such as molecular collision dynamics and energy transfer phenomena in collisions, gas-surface interactions, condensation and evaporation, plume and expansion flows, and many others. All these problems are related to practical issues that can be conventionally divided into two groups. The first group covers the questions related to hypersonic flight of vehicles at high altitudes (mainly external flows). The second group is mainly represented by problems that involve material processing, micromechanical devices, and microelectronics (mainly internal flows with length scales that are comparable with the mean free path). Substantial difficulties arising in studies of both groups of problems are caused not only by the rarefaction of the gas but also by the presence of chemical reactions.

Currently, there are several numerical approaches for solving problems of rarefied gas dynamics, and the choice of a particular approach depends usually on the flow rarefaction, the dimensions of the problem, and the presence of real gas effects. For weakly rarefied flows, it is usually adequate to account for the effects of rarefaction by using slip-velocity and temperature-jump boundary conditions within the standard Navier-Stokes (NS) equations. The NS equations can be derived from the Boltzmann equation by assuming small deviations of the distribution function from the equilibrium distribution. Therefore, the NS equations become unsuitable for studying rarefied flows with finite Knudsen numbers where the distribution function deviates appreciably from the equilibrium distribution. The extension of continuum models to rarefied flows by using the Burnett equations based on the second term of the Chapman-Enskog expansion has difficulties related to the correct formulation of the boundary conditions, and the linear instability of these equations to short-wave disturbances.

For strongly non-equilibrium flows, one should consider using the Boltzmann equation and operating within the framework of the kinetic approach. The Boltzmann equation is a nonlinear integral-differential equation for a one-particle distribution function [1]. The quadratic nonlinearity of the collision integral, the dependence of the integrand function on post-collision velocities, and the high multiplicity (equal to five) of the integration are the main reasons for the mathematical complexity of the Boltzmann equation, which distinguish it from other known gas dynamics equations and complicates the use of classical numerical methods for its solution. In the transitional regime, the continuum approach is typically not adequate everywhere, but kinetic simulations are too expensive because traditionally they require the size of the computational cells to be comparable with the local

mean free path.

The two main approaches that have been used for numerical solution of the Boltzmann equation for practical applications are: Direct Numerical Solution (DNS) and Direct Simulation Monte Carlo (DSMC). Historically, DNS is one of the first methods of solving the Boltzmann equation [2]. It usually consists of two basic steps: the evaluation of the collision integral and the numerical integration of the differential part of the Boltzmann equation. The major advantages of DNS are uniform accuracy of computing both the low- and high-density regions of the flow, and an easy and effective parallelization of the computational code. The limitations of the method are mainly related to dependence of the computational cost on the dimensionality of the problem and the resulting high computational cost for modeling three-dimensional problems [3].

The DSMC algorithm is based on the assumption that a small number of representative "computational particles" can accurately capture the dynamics of the dilute gas described by the Boltzmann equation [4]. The DSMC method also splits the motion of particles into two sequential stages: free-molecular advection and collision relaxation. Implementation of the DSMC method also requires dividing the computational domain into a grid of computational cells. The size of these cells should be sufficiently small so that the change in gas dynamic properties across each cell is small. This size is usually selected as the minimum value of the mean collision time and the mean residence time, so that the molecules do not cross more than one cell during one time step.

The DSMC method has become de facto the main computational tool for studies of complex, multidimensional rarefied flows [5,6]. This is primarily because of its relative simplicity, the possibility of using various models of gas particle interactions and chemical reactions without substantial complications in the computational algorithm, and possibility of effective use of parallel computers. Compared to DNS approaches, the computational cost of DSMC methods is of the order of the number of particles. However, the method becomes too expensive for near-continuum flows because its accuracy depends on the resolution of the collisional length and the collisional time scale. Also, owing to its statistical nature, DSMC methods often yield low-accuracy and noisy results relative to DNS methods, and their convergence in general is quite low.

Aristov has presented a comparison of DNS and DSMC methods in a recent book [3]. It was shown that errors from the use of a uniform velocity grid can be smaller than statistical errors in DSMC. The use of DSMC can lead to a small number of particles representing "tails" of the distribution function, giving rise to appreciable fluctuations, for example, in chemical reaction rates. DNS in principle does not have this disadvantage. Implicit schemes in DNS can be used to study flows at small Knudsen numbers where the explicit schemes are rather slow in convergence. In the traditional DSMC, explicit solution schemes are typically used. For DNS one can use the difference schemes of the second (or higher) order of accuracy, whereas accomplishing higher order schemes with DSMC is not simple. Another advantage concerns the multiprocessor computations: due to uniformity of grids in velocity space, the parallelization of DNS is simple and effective.

Efficient solution of the Boltzmann equation can be obtained using a spatially non-uniform grid in physical space. In the Knudsen layers, one can use a grid with cell sizes smaller than the characteristic mean free path. In the continuum flow regions, one can use the cell sizes much larger than the mean free path. In this respect, using DNS offers a great advantage in comparison with the DSMC methods, which as a rule have to use computational cells smaller than the mean free path, even in the continuum flow regions. Our experience in using DNS for two-dimensional and three-dimensional problems allows us to consider it as a competitive method for simulating multi-dimensional gas flows over a wide range of Knudsen numbers.

For several classes of problems, DNS is strongly preferable to DSMC. The first class of these problems involves subsonic gas flows. Using DSMC for simulations of subsonic flows is very expensive because any perturbations propagate with the speed of sound (~300 m/s), whereas the gas flow velocity could be much smaller (of the order of, say, 1-10 m/s). Using DNS allows one to

separate the equilibrium part and to obtain the solution more efficiently. The second class of problems involves gas mixtures with small fractions of some species. The DSMC method would give large fluctuations in the calculation of the macroscopic properties of these species. Finally, DNS seems preferable for the development of hybrid solvers covering a wide range of *Kn* numbers because both kinetic and continuum parts are described in a similar fashion in terms of partial differential equations and finite volume numerical schemes.

Looking beyond computational methods for rarefied flow problems, an even greater challenge is the development of efficient schemes for practical problems in which the local Knudsen number varies by several orders of magnitude within a computational domain, such that regions of continuum and rarefied flows simultaneously exist in the domain. In such problems, the kinetic treatment is only necessary in the rarefied parts of the domain, and a continuum approach is adequate for the other parts. Since the kinetic treatment is much more expensive than the continuum one, one should use the former only when really needed. That is why numerical techniques based on the combined use of continuum and kinetic models are currently being actively developed.

In seeking a "unified" solution technique, one is confronted with several problems. First, one has to formulate the conditions under which a hydrodynamic description (which is valid for Kn<<1) is tolerable. Second, one has to select a proper way to describe strongly non-equilibrium flows. In the extreme case of free molecular flow, with Kn>>1, one deals with a simpler problem. It is the description of the transition regime, with Kn~1, and its coupling to the continuum regime, with Kn<<1, which becomes the main challenge. Different methods of combining and coupling kinetic and continuum models that have been developed or proposed to date can be classified into three categories:
- Domain decomposition in physical space. In this category, the computational domain is decomposed into kinetic and continuum sub-domains using certain criteria [7],[8].
- Domain decomposition in velocity space. In this category, one performs decomposition in velocity space to describe differently fast particles and slow particles [9].
- Hybrid models. In this category, one solves both the kinetic and the continuum equations in the entire domain and uses the distribution function to compute transport coefficients for the fluid equations [10], [11].

The goal of this Project is to develop a Unified Flow Solver (UFS) for simulation of gas flows across the entire range of *Kn* numbers from the free-molecular regime, to the continuum regime. In particular, we develop a hybrid code that switches automatically from a continuum fluid dynamic solver to a Boltzmann solver and vice versa. The feasibility of such an approach has been demonstrated in several recent papers [12],[13],[14]. When coupling the Boltzmann and continuum equations via domain decomposition, two problems have been identified: proper criteria for domain decomposition into kinetic and fluid regions and suitable numerical algorithms for coupling the different equations. Most works decompose the domain a-priori. They assume a Boltzmann domain in the vicinity of boundaries and a fluid domain away from the boundaries. However, during a simulation, the different domains do not remain fixed, and cannot generally be accurately predicted a-priori. Therefore, one needs criteria for automatic domain decomposition such as those proposed in [15],[16].

The uniqueness of our approach consists in using DNS for simulations of the kinetic domain. Using DNS instead of DSMC offers several advantages for building a hybrid code for multi-scale atomistic/continuum simulations of gas flows. One of the major problems with coupling DSMC and continuum solvers is related to strong fluctuations of the moments calculated from the DSMC's velocity distribution functions. The problem of connecting the two regions is generally overshadowed by rather severe stability problems when DSMC data are handed over to the NS solver at the interface of the kinetic and continuum domains. These fluctuations result in irregular boundaries. Using DNS allows much more manageable interactions between the continuum and kinetic solvers.

The structure of this Report is as follows. Section 3 describes the UFS architecture and key components. Section 4 is devoted to UFS validation and demonstration for monatomic gas flows. Section 5 describes UFS extensions to molecular gases and gas mixtures. Summary of the work is given in Section 6. The list of publications and presentations about UFS is listed in Section 7.

3.   UFS ARCHITECTURE

The key components of the UFS are shown in Figure 1. The main component is a Boltzmann solver. For reasons described above, the DNS method has been selected for the solution of the Boltzmann equation implemented in this project. Another component of the UFS is a continuum (Computational Fluid Dynamics) solver. It is preferable for such a solver to use numerical algorithms similar to the Boltzmann solver. From this point of view, the recently introduced kinetic CFD schemes are very attractive [17],[18] and have been selected in this work. The remaining components of the UFS include criteria for domain decomposition into kinetic and continuum parts and coupling algorithms.

The open source Gerris Flow Solver (GFS) [19] was selected as a framework for the UFS. The original GFS code contained a binary tree-based incompressible flow solver with a dynamically adaptive grid and support of complex boundaries [20]. The semi-structured quadtree/octree meshes offer a good compromise between the flexibility of unstructured meshes and the computational efficiency of structured meshes. Using the GFS framework, we have added all the UFS components, first for a single component gas, then for gas mixtures and molecular gases with internal degrees of freedom of the molecules. The UFS generates Cartesian mesh around embedded solid boundaries (defined through standard files), performs dynamic adaptation of the mesh to the solution and geometry, detects kinetic and continuum domains and selects appropriate solvers based on continuum breakdown criteria. Below we describe the key components of the UFS in detail.
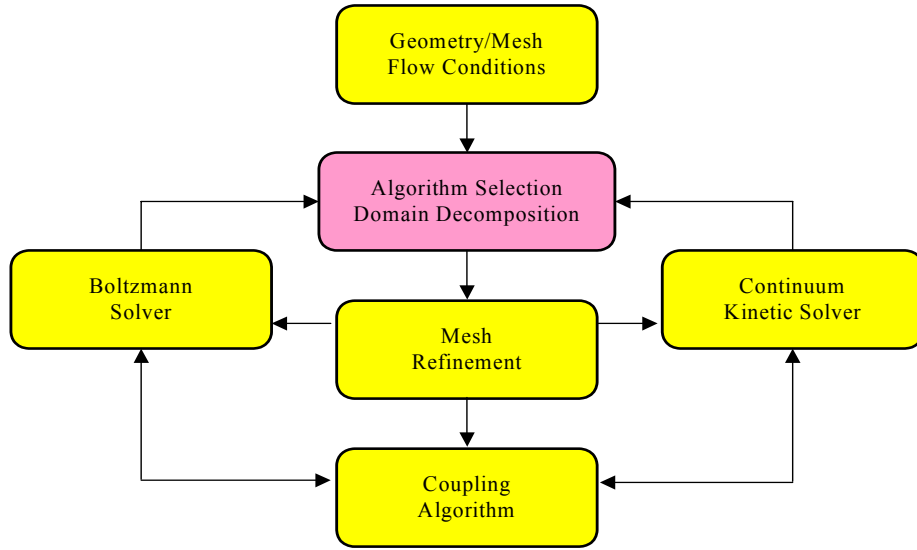
Figure 1 Key UFS components

3.1.   <u>Boltzmann Solver</u>

The Boltzmann transport equation (BTE) describes the evolution of a particle distribution function *f* in a six-dimensional phase space [21]

$$\frac{\partial f}{\partial t} \; + \; \nabla_r \cdot (\xi f) \; = \; I(f,f) \tag{1}$$

Here **r** is a position vector in physical space, ξ is the velocity vector, and *t* is time. The right hand side of Eq. (1) contains an integral operator describing binary collisions among particles. For elastic collisions in a monatomic gas, it has the following form

6

$$I(\xi) = \int_{S^2} d\omega \int_{R^3} (f(\xi_1^{'})f(\xi^{'}) - f(\xi_1)f(\xi))g\sigma(g,\chi)d\xi_1 = -\nu f + G. \quad (2)$$

Here ν is the collision frequency, G is the inverse collision integral, $g = |\xi_1 - \xi|$ is the relative velocity of the colliding particles, ω is a vector on a unit sphere S^2 in velocity space, and $d\omega$ is an element of the area of the surface of this sphere, $\sigma(g,\chi)$ is the differential collision cross section, and χ is the scattering angle. The post-collision velocities (ξ', ξ_1') and the pre-collision velocities (ξ, ξ_1) satisfy the momentum and energy conservation laws

$$\xi + \xi_1 = \xi' + \xi_1',$$
$$|\xi|^2 + |\xi_1|^2 = |\xi'|^2 + |\xi_1'|^2 \quad (3)$$

This integral (2) can also be written in the form

$$I(\xi) = \int_0^{2\pi} d\varepsilon \int_0^{b_m} db \int_{R^3} (f(\xi_1^{'})f(\xi^{'}) - f(\xi_1)f(\xi))gbd\xi_1 \quad (4)$$

Here b is the impact parameter (defined as the distance of the closest approach of the trajectories) usually bounded by a certain value b_m, and ε is the azimuth impact angle. The scattering angle $\chi(g,b)$ depends on scattering potential of inter-atomic interactions. For the Hard Sphere (HS) molecules of diameter d, the scattering is isotropic and $b = d\sin\theta$ where $\theta = (\pi - \chi)/2$. For the Variable Hard Sphere (VHS) models frequently used in DSMC simulations, the scattering is also isotropic and $g\sigma = C_k g^{1-4/k}$, where k is the exponent in the intermolecular potential. For other commonly used scattering potentials, these relationships can be found in [22].

We have implemented the following scattering models: i) the HS model, ii) the inverse power repulsive potential, iii) the Lennard-Jones potential, iv) the Coulomb potential, and v) the BGK model. For 2D simulations, the BGK model was implemented in a reduced form in which the 2D velocity space with averaging in the z-direction. Besides mentioned potentials it is possible to use in the future some modern potentials such as the Tang-Toennies potentials [23].

For the numerical solution of Eq. (1), a Cartesian mesh in velocity space is introduced with a cell size $\Delta\xi$ and nodes ξ_β. Using this velocity grid, Eq. (1) is reduced to a system of linear hyperbolic system of transport equations in physical space with a nonlinear source term

$$\frac{\partial f_\beta}{\partial t} + \nabla_{\mathbf{r}} \cdot (\xi_\beta f_\beta) = I(f_\beta, f_\beta) \quad (5)$$

Introducing computational grid in physical space, we split the solution of (6) into two stages: free flow and relaxation. For the free flow, we used an explicit finite volume numerical scheme

$$\frac{f_{i\beta}^{*k} - f_{i\beta}^{k-1}}{\Delta t} + \xi_\beta \frac{f_{i+1/2,\beta}^{k-1} - f_{i-1/2,\beta}^{k-1}}{\Delta x} = 0, \quad (6)$$

Here, the star * denotes the intermediate level, $f_{i+1/2,\beta}^{k-1}$ is the value of the function on the cell face. $i = (i_x, i_Y, i_z)$ is the 3D spatial index, Δx is the 3D spatial step $(\Delta x, \Delta y, \Delta z)$, and $\beta = (\beta_x, \beta_Y, \beta_z)$ is the

velocity index. The calculation of the face values of the distribution function we use standard interpolation schemes. For the first-order scheme,

$$f_{i+1/2,\beta}^{k-1} = (f_i^{k-1} + f_{i+1}^{k-1})/2 - sign(\xi_\beta)(f_{i+1}^{k-1} - f_i^{k-1})/2. \qquad (7)$$

The second-order scheme has also been implemented using three options: i) no limiter option, ii) the so-called minmod limiter (default), iii) Van Leer limiter. For stationary problems, the first-order scheme in time with time step selected from appropriate CFL criterion is found to be adequate.

The relaxation stage has the form

$$\frac{f_{i\beta}^k - f_{i\beta}^{*k}}{\Delta t} = -v_{i\beta}^{*k} f_{i\beta}^{*k} + G_{i\beta}^{*k}. \qquad (8)$$

Currently, we use an explicit scheme with automatic selection of the time step. It is also possible to use implicit or explicit-implicit schemes for the relaxation stage to increase the time step that may be important for small Knudsen numbers. It is also possible to solve the system (6) without splitting into collisionless flow and relaxation and use any other scheme for solving a hyperbolic system with a nonlinear source term.

We use the Gerris framework [19] to generate dynamically adaptive Cartesian mesh in physical space. The boundary conditions specified at the surface of solid objects imbedded in the computational domain provide the distribution function of the reflected particles as a sum of diffuse and specular reflections with accommodation coefficient α

$$f(\xi) = \alpha f_M(n,T) + (1-\alpha)f_r. \qquad (9)$$

The specular reflection term is $f_r = f(\xi_r)$ where ξ_r is the velocity of an incoming molecule towards the boundary, which after specular reflection transforms into $\xi_r = \xi - 2(\xi \cdot \mathbf{w})\mathbf{w}$ where $\mathbf{w}$ is a unit vector normal to the boundary. The diffuse reflection term contains Maxwellian distribution $f_M(n,T)$ with a zero mean velocity, T is the temperature of the boundary, and the density n is calculated to ensure zero particle flux at the boundary at a given point.

At the boundaries of the computational domain, for most of problems, the distribution function can be assumed a Maxwellian $f_M(n,\mathbf{u},T)$ with a mean velocity $\mathbf{u}$ for $(\xi \cdot \mathbf{w}) > 0$. For the parts of boundary with $(\xi \cdot \mathbf{w}) < 0$, the distribution function is found as a result of the solution.

The computational domain in velocity space is selected as a box in such a way that the values of the distribution function outside of the box are negligible. For 2D (in physical space) problems, half of the box ($\xi_z > 0$) can be used.

3.1.1 Calculation of the collision integral

The main problem in solving the Boltzmann equation consists in evaluating the collision integral [24]. The calculation of the five-fold integrals (2) or (5) represents a challenge with respect to efficiency and precision. We used the discrete analog of the collision integral having the following properties:

i)   The integral should be equal to zero for a Maxwellian distribution, $I(f_M, f_M) = 0$.

ii)   The distribution should remain positive for all nodes in velocity space when the relaxation problem (8) is solved.

iii)   For the collision invariants, $\psi(\xi) = (1, \xi, \xi^2)$, the conservation laws should be satisfied

$$\int_{R^3} \psi I(f,f)d\xi = 0 \tag{10}$$

Below, we review different methods of calculating the integral and explain the choice of the method used in this paper.

The NtN method

The first type of methods can be called Node to Node (NtN). This method has been used by Goldstein [25], Buet [26], Rogier and Schneider [27], Varghese [28] and Frolova [2]. To illustrate the essence of the method, Figure 2 shows a collision sphere in velocity space. This sphere with center $\xi_0 = (\xi_i + \xi_j)/2$ and radius $|g|/2$ is wrapped around pre- and post collision velocities due to energy and momentum conservation, see Eqs (4). The NtN method takes into account only those post-collisional velocities that fall exactly into nodes of the velocity grid. Therefore all properties (1-3) are satisfied automatically. The NtN method is conservative and deterministic, and requires no interpolation of the velocity distribution function. The drawback of the method is that only for defined scattering angles $\chi(g,b)$, the post-collision velocities distributed over collisional sphere fall exactly at the velocity grid and the method is applicable only for VHS-like models with isotropic scattering. The NtN method cannot be extended for more general potentials of intermolecular interactions and for non-uniform grid in velocity space because only selected post-collisional velocities are used. Also, extensions to gas mixtures with arbitrary ratio of the molecular mass is impossible.

For the numerical calculation by the NtN method, the integral (2) can be written in a symmetric form [28]

$$I(\zeta) = \frac{1}{4} \int_{S^2} d\omega \int_{R^3}\int_{R^3} (\delta(\xi_1' - \zeta) + \delta(\xi' - \zeta) - \delta(\xi_1 - \zeta) - \delta(\xi - \zeta)) f(\xi) f(\xi_1) g \sigma(g,\omega) d\xi d\xi_1 \tag{11}$$

where $\delta(\xi)$ is the delta-function. The advantage of this representation for the numerical evaluation is that direct and inverse collisions are treated symmetrically and microscopic reversibility is satisfied. For the numerical evaluation of the 8-fold integral (11) the integral is written in the form

$$I = \frac{\Delta\xi^6}{4\pi} \sum_i^N \sum_j^N f_i f_j \int_{S^2} d\omega \left[\Delta_i + \Delta_j\right] g_{ij}\sigma_{ij}(\omega) \tag{12}$$

where $\Delta\xi$ is the cell size in velocity space, $\Delta_i = \delta(\xi_i' - \xi) - \delta(\xi_i - \xi)$, $\Delta_j = \delta(\xi_j' - \xi) - \delta(\xi_j - \xi)$, and N is the total number of nodes in velocity space.

To evaluate the remaining integral over the unit sphere ensuring the exact energy conservation, the NtN method takes into account only those post-collisional velocities that fall into the collisional sphere (see Figure 2)

$$\int_{S^2} d\omega \left[\Delta_i + \Delta_j\right] \sigma_{ij}(\omega) = \sum_l^{M_{ij}} w_{ijl} \left[\Delta_i + \Delta_j\right] \tag{13}$$

where M_{ij} is the total number of such points (for each i and j) and w_{ijl} are their weights. For the VHS-like models, the number and position of nodes on the collisional sphere can be determined *a priory* and the calculation of weights is simple, $w \sim 1/M$. For more general potentials, the angle

9

between direct and inverse collisions is a function of relative velocity and these calculations become cumbersome.

The NtN method is conservative, micro-reversibility of collisions is satisfied, and no interpolation of the distribution function is required. For good accuracy, a rather dense mesh has to be used in velocity space. If all velocity nodes of the grid are used the method is deterministic. The evaluation of integral in this case requires $O(N^2)$ computations. To reduce this number of computations it is possible to select collisions using Monte Carlo method [28].
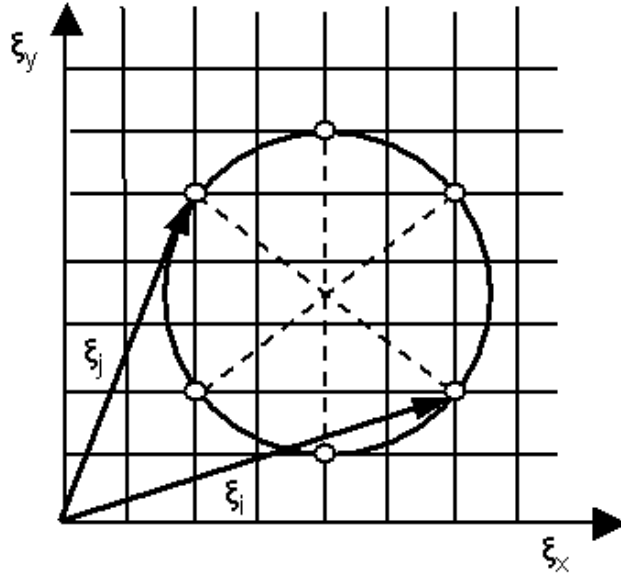
Figure 2 Collision sphere and selection of the collisions for the NtN method

Tcheremissine's method

To generalize the NtN method for more complex cases it is necessary to take into account the inverse collisions that do not fall exactly on the nodes of the velocity grid. Depending on how the post collision velocities are taken into account it is possible to obtain different schemes of integral calculation. In a series of works (see [29] and references therein), Tcheremissine has developed conservative methods of calculating collision integral for arbitrary interaction potential, using interpolation in velocity space. Dividing contributions of post collision points into two parts and accounting them in two of the closest nodes (see Figure 3), it is possible to satisfy conservation laws at each collision. This method is briefly described below.

For arbitrary potential on intermolecular interactions, it is more convenient to perform integration over collision impact parameters (5) instead of integration over a unit sphere (2). The corresponding integral in the symmetric form is

$$I(\xi^*) = \frac{1}{4} \int_0^{2\pi} d\varepsilon \int_0^{b_m} db \int_{R^3} \int_{R^3} [\delta(\xi^* - \xi_1) + \delta(\xi^* - \xi) + \delta(\xi^* - \xi_1') + \delta(\xi^* - \xi')] i(\xi, \xi_1) b g d\xi_1 d\xi \quad (14)$$

where $i(\xi, \xi_1) = f(\xi') f(\xi_1') - f(\xi) f(\xi_1)$. The velocities before collision (ξ, ξ_1) are chosen in integer nodes N, N_1 of the grid and post collision velocities (ξ', ξ_1') may not lie in integer nodes. To obtain the mass, impulse, and energy conservation in each collision and satisfy the condition $(\psi(\xi_N) + \psi(\xi_{N1}) - \psi(\xi') - \psi(\xi_1')) = 0$, the value of $\psi(\xi') + \psi(\xi_1')$ is interpolated to the nearest

10

integer nodes ξ', ξ'_1 using the following interpolation:

$$\psi(\xi') + \psi(\xi'_1) = (1-\lambda)(\psi(\xi_M) + \psi(\xi_{M1})) + \lambda(\psi(\xi_L) + \psi(\xi_{L1})). \qquad (15)$$

On a uniform grid, it is possible to perform this interpolation with one coefficient for five functions, since conservation of mass and impulse in this case is satisfied automatically due to symmetric position of nodes. The coefficient λ is found from the equation

$$(\xi'_1)^2 + (\xi')^2 = (1-\lambda)[(\xi_M)^2 + (\xi_{M1})^2] + \lambda[(\xi_L)^2 + (\xi_{L1})^2]. \qquad (16)$$

The weight coefficients λ and $1-\lambda$ define the contribution
$i(\xi', \xi'_1) = (f(\xi_N)f(\xi_{N1}) - f(\xi')f(\xi'_1))$ to the closest integer nodes $\xi_L, \xi_{L1}, \xi_M, \xi_{M1}$, see Figure 3.
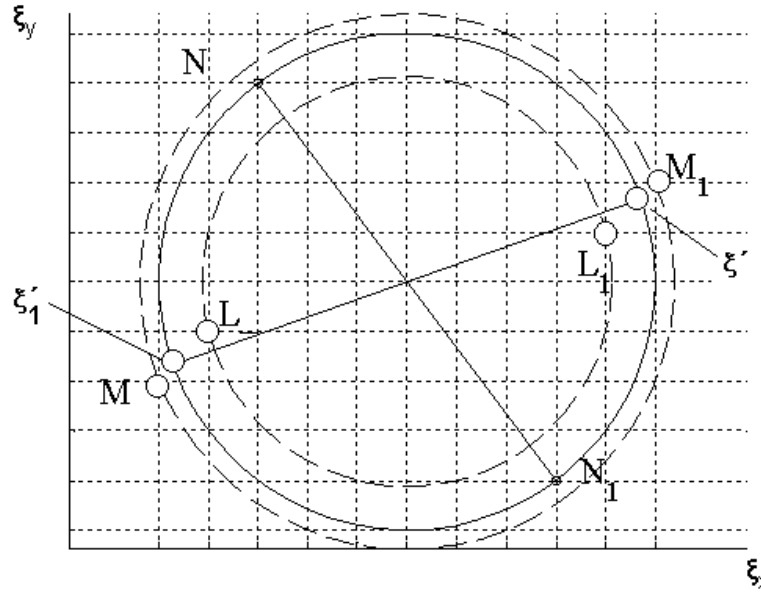
Figure 3 Selection of post-collision nodes for Tcheremissine's method.

The interpolation of $f(\xi')f(\xi'_1)$ can be performed using any interpolation formula and does not influence the conservation laws.

The NtCN method

Finally, we describe a method that can be used for arbitrary interaction potentials and non-uniform grid in velocity space. We start from the same symmetrical form of integral as in Tcheremissine's method.
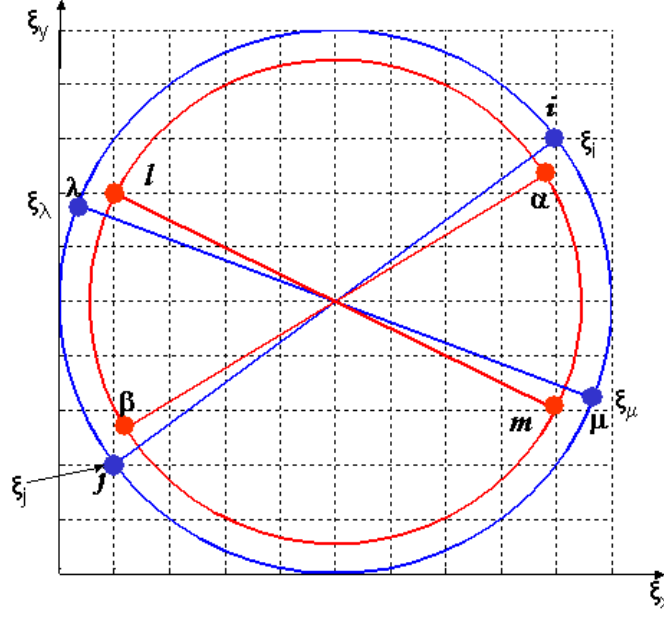
Figure 4 Selection of nodes for NtCN method.

The procedure of calculating collision integral consists of the following steps:

- select values of pre collision velocities ξ_i, ξ_j for some impact parameters b, ε

- determine post collision velocities ξ_μ, ξ_λ,

- find the nodes ξ_m, ξ_l closest to the nodes ξ_μ, ξ_λ,

- make an inverse collision with velocities ξ_m, ξ_l for the same impact parameters b, ε,

- calculate velocities after this inverse collision ξ_{α_k}, ξ_{β_k},

- calculate contributions to the integral from the direct $I_{ij} = (f_\lambda f_\mu - f_i f_j) g_{ij} b$, and inverse $I_{ml} = (f_\alpha f_\beta - f_m f_l) g_{ml} b$ collisions, where the quantities $f_\alpha f_\beta$, $f_\lambda f_\mu$ are found using a logarithmic interpolation to give zero integral for a Maxwellian distribution.

- sum up contributions to the direct and inverse integrals $-\nu(\xi_i) f(\xi_i) + G(\xi_i)$,

This procedure of evaluating collision integral uses closest nodes (NtCN) for accounting inverse collisions and introduces errors of the order of $O(h_\xi) | f - f_M |$ in conservation of mass, momentum and energy. In order to eliminate these errors, we introduce a correction to the collision frequency using the method of least squares

$$\nu^*(\xi) = (1 + a_0 + a_1 \xi_x + a_2 \xi_y + a_3 \xi_z + a_4 (\xi_x^2 + \xi_y^2 + \xi_z^2)) \nu(\xi), \quad (17)$$

where the coefficients a_i are defined from the collision invariants (11). Thus, this method of calculating the Boltzmann collision integral possesses all the properties (1-3).

For evaluation of the eight-dimensional integrals, the Korobov sequences [30] are applied. In the general case, Korobov's points in a s-dimensional hypercube are defined as

$$x_{r\nu} = \left\{ \nu a_r^{p_\nu} / p \right\}, \quad r = 1, 2, ..., s, \quad \nu = 1, 2, ..., p - 1 \quad (18)$$

where p is a prime number, $a_r^{p_v}$ are precalculated integer coefficients, and the brace denotes the reminder on dividing an integer by an integer. The velocity grid points closest to the selected Korobov's points are taken as the velocity grid points. The accuracy of this procedure is estimated as $O((\ln N_c)^{\alpha s} / N_c^{\alpha})$, where the exponent $\alpha \geq 1$ depends on the smoothness of the integrated function. For a piecewise-constant function, $\alpha = 1$. The above error is less than the estimated error of the Monte Carlo method.

The typical number of quasi-random trials N_c in our simulations was equal to 34000. We have only accounted for trials that fall inside a sphere (with center and radius defined by the characteristic parameters of the problem) under the condition that inverse collisions also fall into this sphere. Depending on the value of N_c, and the number of cells in velocity space N, different Korobov's sequences were selected.

Note that all three methods described above make it possible to solve the BTE without splitting into the stages of relaxation and free molecular flow and using any other scheme of calculating a hyperbolic system with a source term.

The search for the best methods of calculating the Boltzmann collision integral continues. Many attempts have been explored [31], among them are polar discretization of the velocity space [32], smoothing of the collision spheres [33], and smoothing the collision integral [34] in order to incorporate more points of the discrete velocity grid.

3.1.2 Validation of the Boltzmann solver

In this Section, we describe selected validation cases for the Boltzmann solver

Shock Wave Structure

The problem of shock wave structure is ideal for testing accuracy of the numerical BTE solution, in particular, the accuracy of the nonlinear collision term. We have performed simulation of the shock wave structure for different Mach numbers and compared our results with with previous DSMC results and with experimental data. The comparison with the benchmark results [18] obtained by the conservation splitting method and by the Ohwada's method demonstrated agreement for gas density and temperature with accuracy of 1% for the HS model at Mach number M=3.

Figure 5 compares our computations with experiments for density and temperature profiles in the shock wave in rare gases for two different Mach numbers. The density profile in Argon for *M*=3.8 is compared with an experiment by Alsmeyer [35]. The temperature profile in Helium for *M*=1.59 is compared to the experiment [36]. The computations were performed for the Lennard-Jones interaction potential. The agreement of experimental and calculated profiles indicates the high accuracy of the Boltzmann solver.
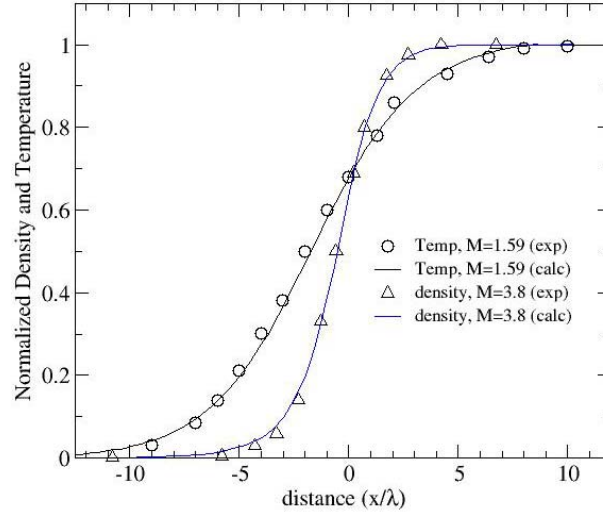
Figure 5. Normalized gas density at M=3.8 and temperature at M=1.59 for a shock wave in argon (solid lines – calculations, symbols – experiment)

Figure 6 shows longitudinal and transversal temperatures *Tx* and *Ty* in comparison with DSMC results [37]. The velocity grid in the Boltzman solver was (24,24,12). One can see that the DNS and the DSMC results are in close agreement. Figure 7 compares results of the Hard Sphere model and the inverse power of 12 model.
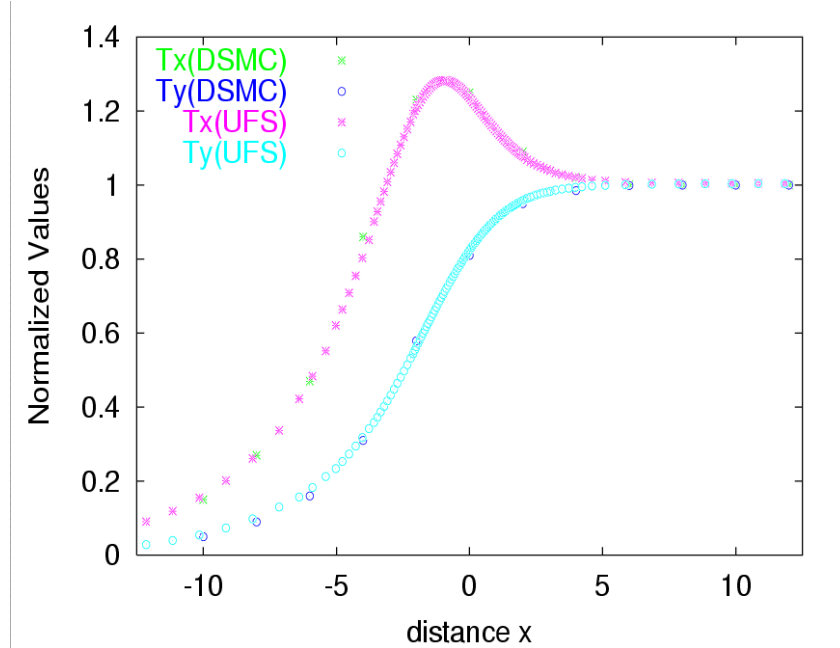
Figure 6 Comparison of the UFS results with DSMC results for the shock wave problem at Mach = 5.

8572/F
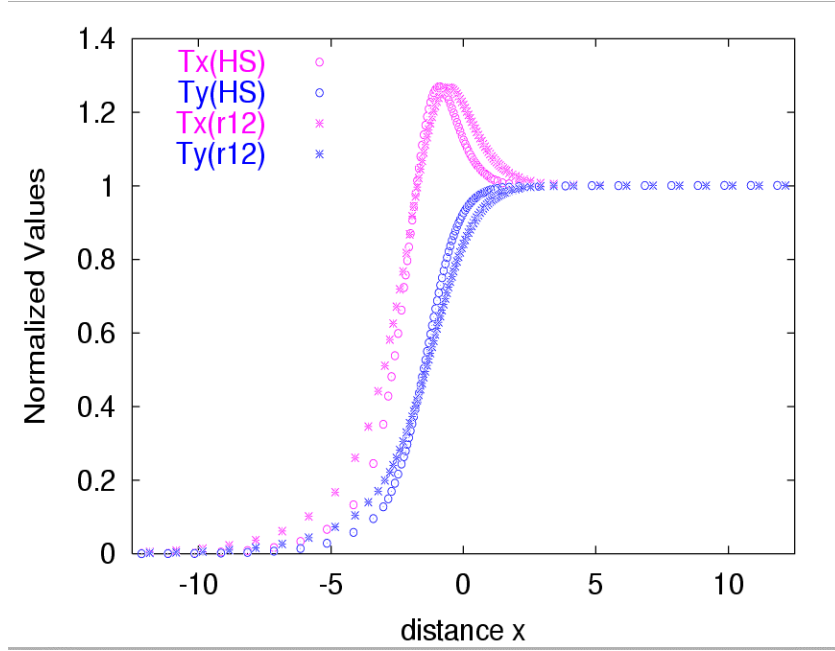
Figure 7 Comparison of Tx and Ty for two different models of the potential:
HS – hard sphere model and r12 – inverse power of 12.

To evaluate efficiency of the Boltzmann solver for hypersonic flows, we have simulated the shock wave structure at *M*=25 using the Boltzmann solver for the hard sphere gas. The profiles of macroscopic parameters are shown in Figure 8 (top left). The slices of the distribution function at *w=h/2* as a function on *v* and *u* velocity components in 3 locations: $X_c + 0.3\lambda$, $X_c - \lambda$, and $X_c + \lambda$ are shown in Figure 8. The grid size in the velocity space is *h*=1.235 of thermal velocity. The second slice corresponds to the normalized density nearly 0.56, hence to the 1D graphics of the Muntz paper. The computations are made at about 45,000 velocity nodes with CPU time of about 75 hrs.
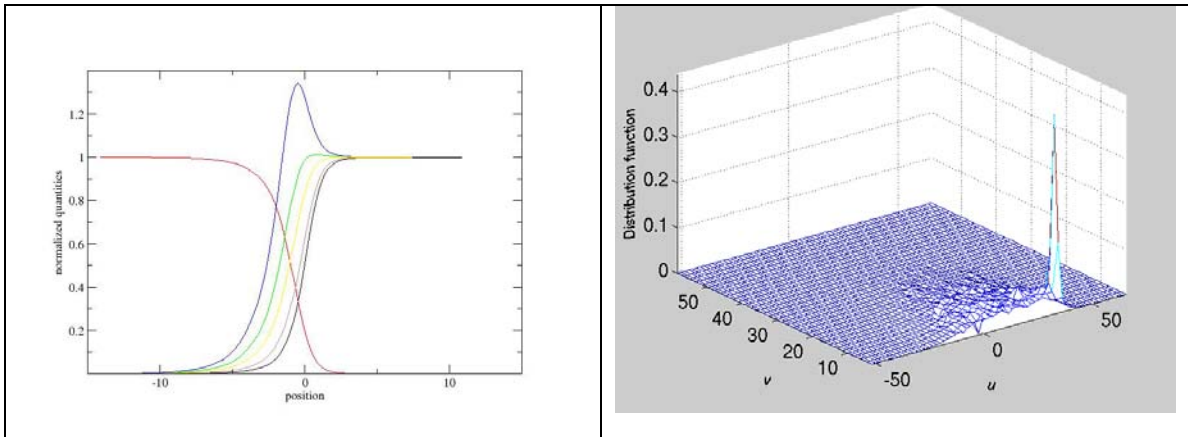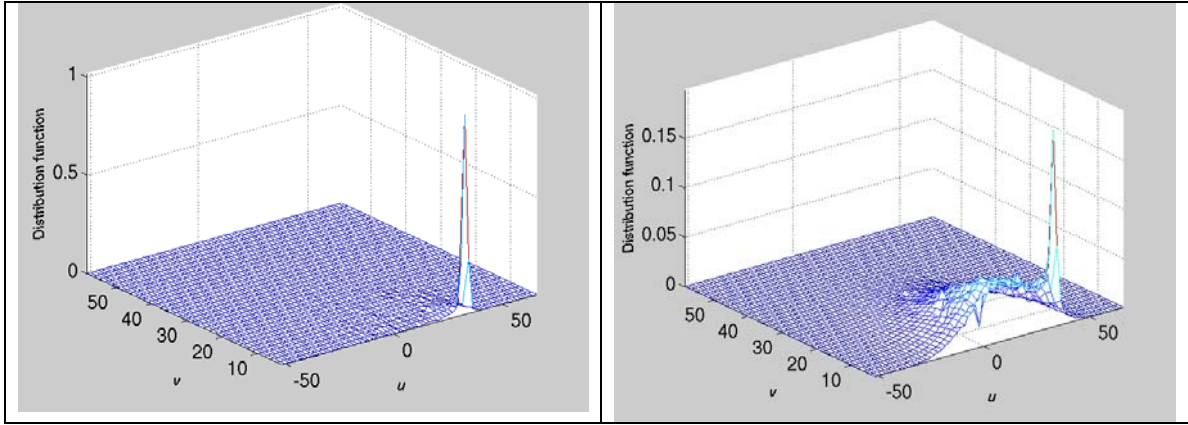
Figure 8 Shock wave at M=25. Macro-parameters and velocity distribution functions f(v,u,w=h/2) at 3 positions inside the shockwave.

Heat Transfer Between Parallel Plates

We have performed testing of the Boltzmann solver for a 2 dimensional problem of heat transfer between two parallel plates with nonuniform temperature along the plate surfaces. For the collisionless gas flow between two parallel plates with temperatures $T_1(x) = 1$ at *y=0.5* and $T_2(x) = 1 - 0.5\sin(2\pi x)$ at *y=-0.5*, we obtained an analytical solution shown in Figure 9. This solution was used to access limitations of the discrete velocity model.
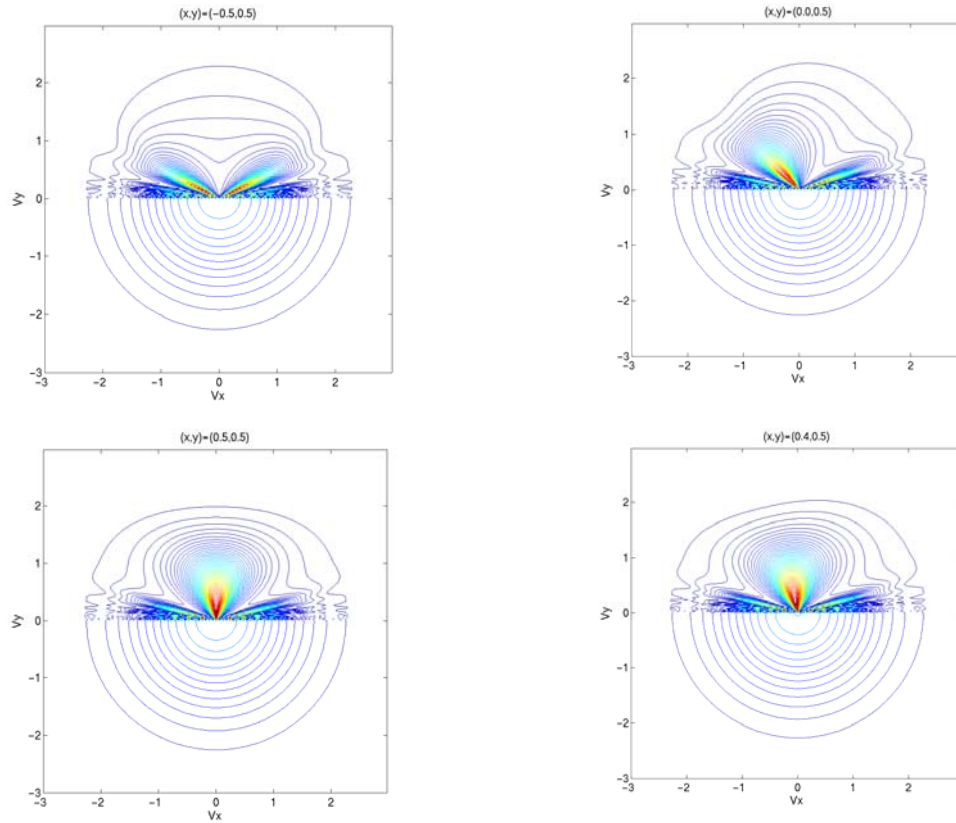
Figure 9 Velocity distribution function at different points.

In order to test the capabilities of the UFS for low speed problems we have solved a series of problems of heat transfer between parallel plates using Boltzmann and kinetic NS solvers. In this problem, two plates are heated to a non-uniform temperature, which is $T = 1 - 0.5\cos(2\pi x)$, along the *x*-axis, which is the axis of periodicity. The results of calculations using the Boltzmann solver with BGK collision model are presented in Figure 10. One can see that there is also well-formed vortex-type distribution of the velocity flow field. Using the Boltzmann solver for *Kn* from 0.03 up to 3, we observe a maximum of the flow velocity of about of 0.007 at *Kn*=0.1.
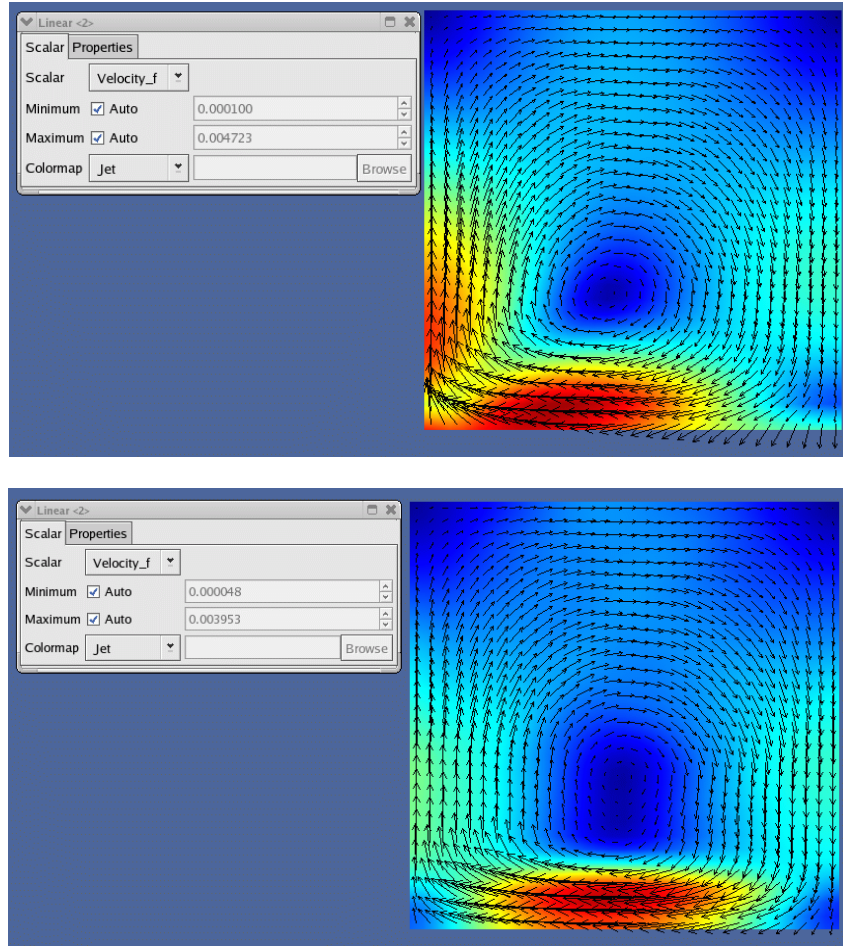
Figure 10 Results of simulations of the heat transfer problem using the Boltzmann solver for two Kn numbers: Kn = 0.03 and Kn = 1. The total velocity profile is plotted, together with velocity vectors.

Collisionless Flow Around Cylinder

Consider rarefied gas flow over a cylinder. At the left-hand side boundary (in front of the cylinder) we assume that the velocity distribution function of the gas is of the form

$$f_\infty(t, x, \xi) = \frac{n_\infty}{(T_\infty \pi)^{3/2}} \exp(-\frac{(\xi_x - U_\infty)^2 + (\xi_y - V_\infty)^2 + \xi_z^2}{T_\infty}), \qquad (19)$$

where $n_\infty, U_\infty, V_\infty, T_\infty$ are the number density, the velocity components, and the gas temperature in the free stream. Introduce dimensionless velocity according to $U_0^2 = 2kT_0/m$. On the surface of the cylinder, we assume diffuse reflection of the gas molecules, i.e. the distribution of the reflected molecules as

$$f_r = (n_r / \pi T_r)^{3/2} \exp(-\frac{(\xi_x^2 + \xi_x^2 + \xi_x^2)}{T_r}).$$

The non-penetration condition at the surface results in the relation

$$\int\limits_{\xi \cdot n \geq 0} f_r(t, x, \xi_r)(\xi_r \cdot n) d\xi_r = -\int\limits_{\xi \cdot n \leq 0} f_i(t, x, \xi_i)(\xi_i \cdot n) d\xi_i,$$

that defines the distribution function of the reflected particles, f_r, through the known distribution function of the incident particles, f_i. Assuming the temperature of the cylinder, T_r is equal to the gas temperature at the stagnation point on the axis, and using the condition of the constant enthalpy along the flow stream line, we obtain

$$T_r = T_\infty (1 + \frac{(\chi - 1)}{2} M^2),$$

where $\chi = 5/3$ and M denotes the Mach number.

Figure 11 compares the calculated heat flux over the cylinder surface for free molecular flow with an analytical solution. It is seen that the numerical and analytical results agree with high accuracy.
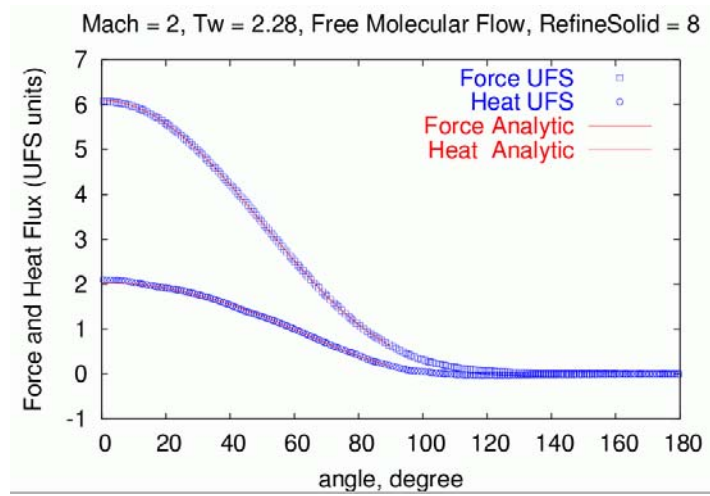
Figure 11 Force and heat flux for free flow around cylinder.

3.2. Continuum Flow Solvers

Traditional numerical schemes of Computational Fluid Dynamics (CFD) are based on discretization of the continuum (Euler or Navier-Stokes) equations. Kinetic schemes differ from the traditional CFD schemes - they use the BTE for building numerical CFD algorithms (see [38]). Kinetic schemes for the Euler equations have been proposed in [39],[40], and independently in [41],[42]. The main idea of this approach was suggested earlier, in [43]. Kinetic schemes using *moments* of the equilibrium distribution function were introduced by Deshpande et al. [44], and later further developed and improved in [45], [17], [46], [47]. Generally, kinetic schemes are preferable for hybrid codes since the BTE is used as a foundation for both algorithms. We have used kinetic schemes for the continuum equations to facilitate coupling to the Boltzmann solver. The implementation of the kinetic schemes for the Euler and NS equations is described below.

3.2.1. Kinetic Euler Solver

Our kinetic Euler scheme follows the EFM Equilibrium Flux Method by Pullin [39]. The main idea of

this method is illustrated below for a 2D case. Consider Euler equations in the form

$$\frac{\partial h}{\partial t} + \frac{\partial F}{\partial x} + \frac{\partial G}{\partial y} = 0, \tag{20}$$

where

$$h = \{\rho, \rho u, \rho v, \rho E\},$$
$$F = \{\rho u, p/2 + \rho u^2, \rho v u, u(\rho E + p)\},$$
$$G = \{\rho v, \rho u v, p/2 + \rho v^2, v(\rho E + p)\}.$$

Here ρ is the gas density, u and v are the mean gas velocities along the x and y axes, correspondingly, $\rho E = 3/2\rho T + \rho(u^2 + v^2)$ is energy, T is temperature, and $p = \rho T$ is gas pressure (dimensionless units are used).

The discretization of Eq. (20) using the finite volume method gives

$$h_{ij}^{n+1} = h_{ij}^{n} - \frac{\Delta t}{\Delta x}(F_{i+1/2,j}^{n} - F_{i-1/2,j}^{n}) - \frac{\Delta t}{\Delta y}(G_{i,j+1/2}^{n} - G_{i,j-1/2}^{n}), \tag{21}$$

where h_{ij}^{n} is the cell averaged value of h at a time t^n, $F_{i+1/2,j}^{n}$ and $G_{i,j+1/2}^{n}$ are fluxes on cell faces along x and y, correspondingly. To obtain these fluxes, we calculate the integrals over the velocity distribution function

$$F_{i+1/2,j}^{n} = \frac{1}{\Delta t}\int_{t^n}^{t^{n+1}}\int_{R^3}\psi\xi_x f(x_{i+1/2}, t, \xi)d\xi dt$$

$$G_{i,j+1/2}^{n} = \frac{1}{\Delta t}\int_{t^n}^{t^{n+1}}\int_{R^3}\psi\xi_y f(y_{j+1/2}, t, \xi)d\xi dt \tag{22}$$

where ψ denotes the collision invariants defined above. The required velocity distribution at the cell faces is taken in the form

$$f = H[\xi]g^l + (1 - H[\xi])g^r, \tag{23}$$

where g^l and g^r are Maxwellian distributions at the neighboring cells

$$g^l = \frac{\rho_{i+1/2}^{n}}{(\pi T_{i+1/2}^{n})^{3/2}}\exp[-\frac{(\xi_x - u_{i+1/2,j}^{n})^2 + (\xi_y - v_{i+1/2,j}^{n})^2}{T_{i+1/2}^{n}}] \tag{24}$$

and $H[\xi]$ is the step function

$$H[\xi] = \begin{Bmatrix} 1, \xi > 0 \\ 0, \xi < 0 \end{Bmatrix},$$

By substituting the distribution function (23) into the expression for the fluxes (22) and performing the integration, one obtains

$$F_{i+1/2,j}^{n} = \int_{\xi_x>0}\xi_x\psi g^l d\xi + \int_{\xi_x<0}\xi_x\psi g^r d\xi$$

$$G_{i,j+1/2}^{n} = \int_{\xi_y>0}\xi_y\psi g^l d\xi + \int_{\xi_y<0}\xi_y\psi g^r d\xi \tag{25}$$

19

For the first order scheme, the values of macro-parameters at faces $\rho_{i+1/2,j}^n, u_{i+1/2,j}^n, v_{i+1/2,j}^n, T_{i+1/2,j}^n$ are calculated for the functions g^l and g^r using the known values of the macro-parameters in cells $x_{ij}(x_{i+1,j})$. For the second order scheme, the calculation of these macro-parameters is performed using standard methods of reconstruction using the values at $x_{i-1,j}, x_{ij}, x_{i+1,j}$ ($x_{i,j}, x_{i+1,j}, x_{i+2,j}$) cells and corresponding limiters.

3.2.2. Validation of the kinetic Euler solver

We illustrate the kinetic Euler scheme for a two-dimensional transient simulation of an internal gas flow in a channel with a forward-facing step at *M=3*. The first and second order numerical schemes have been used with mesh refinement based on density gradient. The second-order scheme employs the minmod limiter or Van Leer Limiter. Figure 12 and Figure 13 show simulation results with a sensitivity parameter for mesh refinement equal to 0.025. The total number of cells is 5060, the computational time is 1 hour, and the memory usage is 80 MB on an AMD 2.4 GHz desktop.
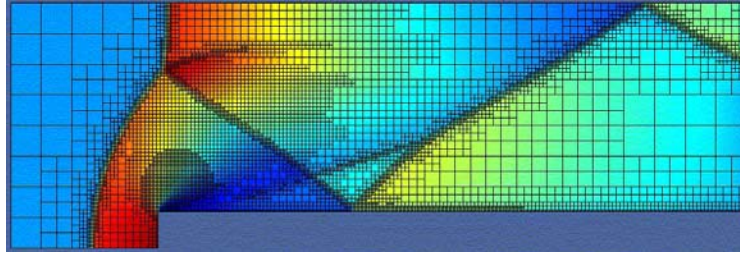
Figure 12 Computational mesh and gas density, t=4
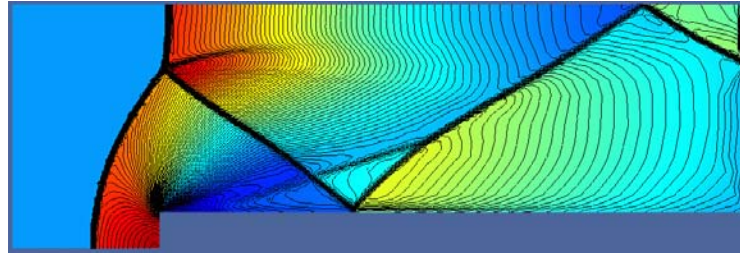
Figure 13 Density contours, t=4

Comparison of the results presented in Figure 13 with published data shows that the kinetic Euler solver gives results close to those of Ref [48].

3.2.3. Kinetic NS solver

Minimizing the size of the kinetic domain where the Boltzmann equation is solved can increase the efficiency of UFS. Using the Navier Stokes (NS) solver instead of the Euler solver can expand the size of the continuum domain. The idea of our kinetic NS solver is a generalization of the scheme used for the kinetic Euler solver and the Kinetic Flux Vector Splitting method by Chou and Baganoff [45] with the distribution function at cell faces taken from Xu [17]. Details are described below.

The development of the kinetic NS solver is based on the solution of the BGK equation

$$\frac{\partial f}{\partial t} + \nabla_r \cdot (\xi f) = \frac{g-f}{\tau},$$

where the inter-collision time $\tau = \mu / p$ is expressed though gas viscosity μ and pressure p. The integration along characteristics gives

$$f(\mathbf{r},\xi,t) = \frac{1}{\tau}\int_0^t g(\mathbf{r}^1,\xi,t^1)e^{-(t-t^1)/\tau}dt^1 + e^{-t/\tau}f_0(\mathbf{r}-\xi t),$$

where $\mathbf{r}^1 = \mathbf{r} - \xi(t-t^1)$. We use directional splitting method to reduce the multi-dimensional problem to a set of one-dimensional problems. For a one-dimensional case, the distribution function $f_0 = f(x,\xi_x,\xi_y,\xi_z,t=0)$ and the Maxwellian distribution $g(x,\xi_x,\xi_y,\xi_z,t)$ on cell faces are expressed as [21]:

$$f_0 = g^l[1+a^l x - \tau(a^l\xi_x + A^l)](1 - H[x]) + g^r[1+a^r x - \tau(a^r\xi_x + A^r)]H[x], \quad (26)$$

$$g(x,t) = g_0\,[1+(1-H[x])\overline{a}^l x + H[x]\overline{a}^r x + At],$$

where functions $a^{l,r}, \overline{a}^{l,r}, A^{l,r}, A$ are polynomial functions in velocity space

$$a = \alpha_1 + \alpha_2\xi_x + \alpha_3\xi_y + \alpha_4\xi_z + \alpha_5(\xi_x^2 + \xi_y^2 + \xi_z^2)$$

with coefficients $a^{l,r}, \overline{a}^{l,r}$ expressed through gradients of the macro parameters in physical space. Coefficients $A^{l,r}$ are calculated to satisfy conservation laws:

$$\int(a^{l,r}\xi_x + A^{l,r})\psi_\alpha d\xi = 0,$$

where ψ_α are the collision invariants. The parameters of the Maxwellian distribution g_0 are calculated from the relation

$$\int g_0\psi_\alpha d\xi = \int_{\xi_x>0} g^l\psi_\alpha d\xi + \int_{\xi_x<0} g^r\psi_\alpha d\xi,$$

For calculation of function A, the condition suggested in [49] is used

$$\frac{\partial}{\partial t}\int[g(0,\xi,t)-f(0,\xi,t)]\psi_\alpha d\xi\,|_{t=0} = 0.$$

Having obtained the velocity distribution function on cell faces, the particle fluxes on faces are calculated by integration of the velocity distribution function with the collision invariants

$$F_{\alpha,x+1/2} = \int\xi_x\psi_\alpha f(x_{i+1/2},\xi,t)d\xi,$$

$$G_{\alpha,y+1/2} = \int\xi_y\psi_\alpha f(y_{i+1/2},\xi,t)d\xi,$$

This scheme incorporates the non-equilibrium character of the distribution function by additional parameter $\tau g^{l,r}(a^{l,r}\xi + A^{l,r})$ and approximates the NS equations if $\tau g^{l,r}(a^{l,r}\xi + A^{l,r}) << 1$

21

3.2.4 Validation of the kinetic NS solver

Figure 14 shows results of simulations for gas flow around a prism for *M*=5, angle of attack of 6 degrees, using kinetic NS solver. The boundary condition at the body surface is diffusive reflection with the temperature of the wall *T*=9. Mesh adaptation performed using parameter $\delta = \log(n) + \log(u) + \log(v)$ where *n* is the gas density, *u* is longitudinal velocity and *v* is transversal velocity. This value of the parameter gives correct concentration of the grid not only in the area of the shock waves but also behind the body that is important for study vortex flows.
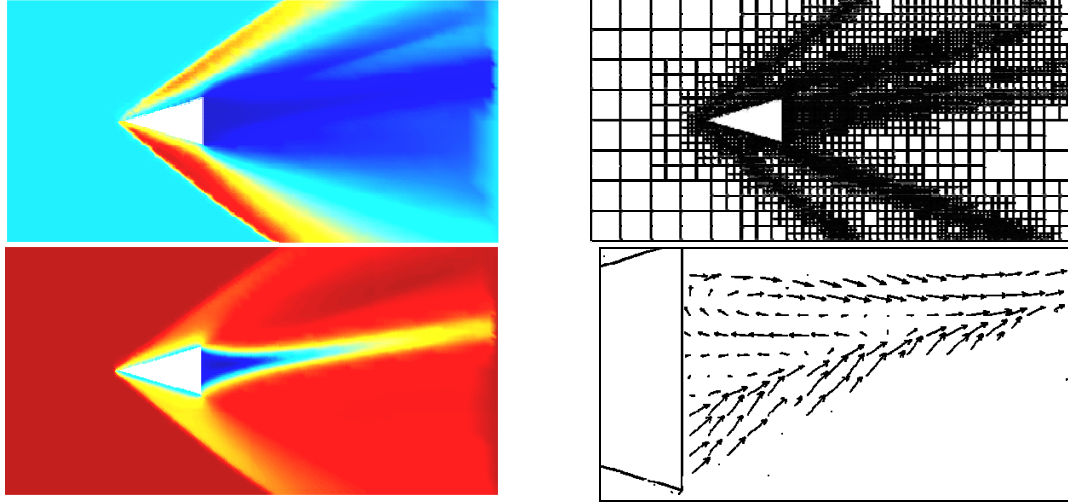
Figure 14 Gas flow around a prism at M=5, Kn=0.0001. The density (upper left) and velocity distribution (lower left), the computational grid (upper right) and velocity vectors behind the body (lower right).

The results of calculations of low speed gas flow between nonuniformly heated plates are presented in Figure 15. One can see that there is a well-formed vortex in the middle of the simulation domain. This vortex is temperature-driven. The flow velocity at larger Kn =0.03 is about twice as large as for Kn=0.001 and its value of 0.0012, which is in very good agreement with the results obtained by Sone [38] using the linearized Boltzmann calculations.
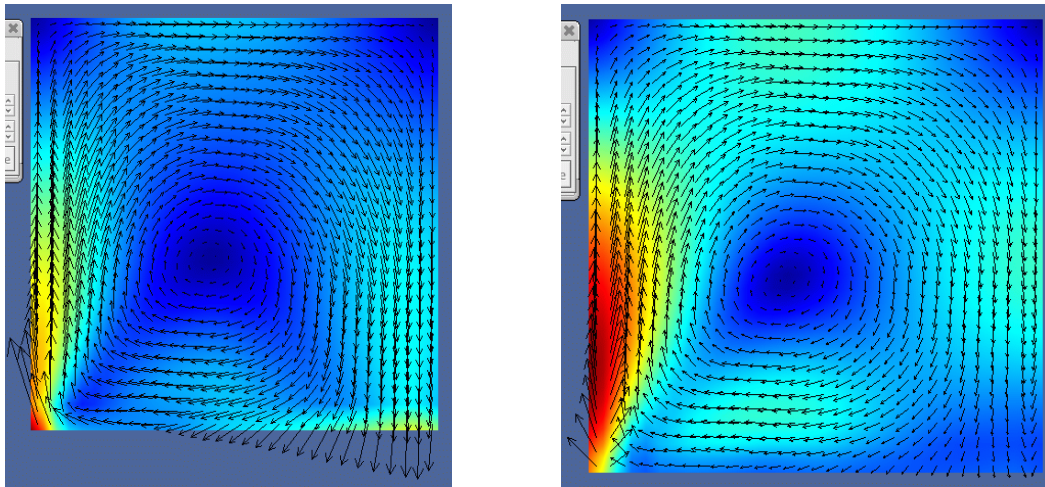
Figure 15 Results of simulations of the heat transfer problem using the kinetic NS solver for two Kn numbers: Kn = 0.001 and Kn = 0.03. The total velocity profile is plotted, together with velocity vectors.

3.2.5 Prandtl Correction

It is well known that the BGK model results in incorrect Prandtl number, *Pr=1*. To introduce *Pr* correction, we calculated the heat flux F_H on the cell faces using polynomial interpolation of the velocity distribution function defined at cell centers. The resulting heat flux has the form

$$F_E = F_E + (\frac{1}{Pr} - 1)F_H.$$

This algorithms of *Pr* correction was tested for the shock wave structure for different M numbers (1.5,3,5,10) and for different temperature dependence of the viscosity coefficient (see Figure 16). The results of calculations were compared with the benchmark calculations by Xu using the classical NS solver.
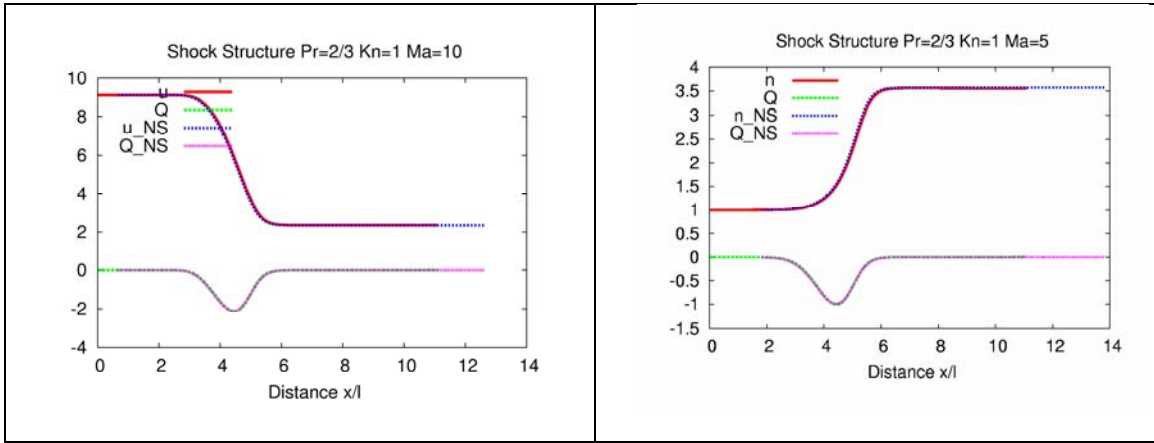
Figure 16 Comparison of the kinetic NS solver with Pr correction with classical NS solver for M=10 (left) and M=5 (right)

The BGK model implemented in the new form allowed us to implement the Shakhov correction in an simple and efficient manner. The new BGK model with Shakhov correction has been benchmarked for the shockwave problem as different Mach numbers. Figure 17 shows results of comparison for the heat flux between 3 models: the BGK model with no Pr correction (Pr = 1), the BGK model with Pr correction (Pr = 2/3) and the full Boltzmann calculation. One can see that the BGK model with Shakhov correction reproduces very well the results of full calculations and that the results without Pr correction differ significantly from the full calculations (see also Figure 18).
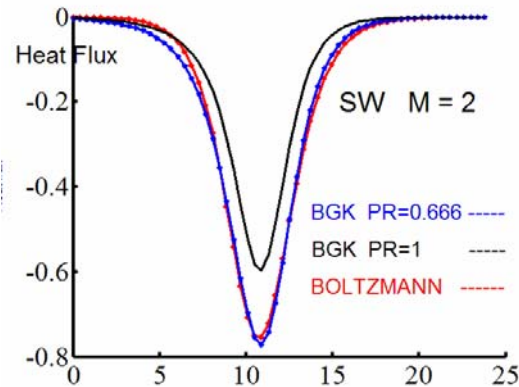
Figure 17. Comparison of the heat flux profiles calculated for 1D SW at Mach = 2 using the full Boltzmann collisional integral (HS model), the Shakhov Model with Pr = 2/3 and the BGK model with Pr = 1.

23
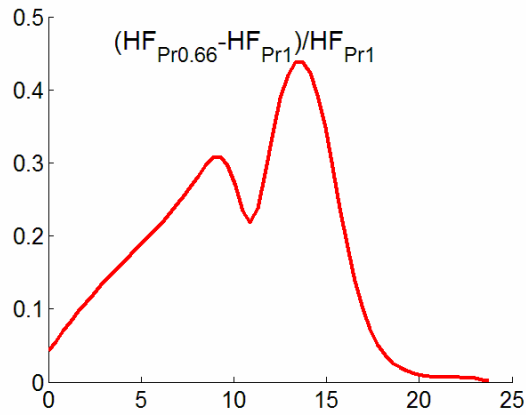
Figure 18. Normalized difference in heat flux calculated with and without Pr correction for the SW problem at Mach = 2.

Figure 19 shows the results of UFS calculations of SW structure at M=2 with the BGK model without Pr correction (Pr = 1) and with Pr correction (Pr = 2/3).
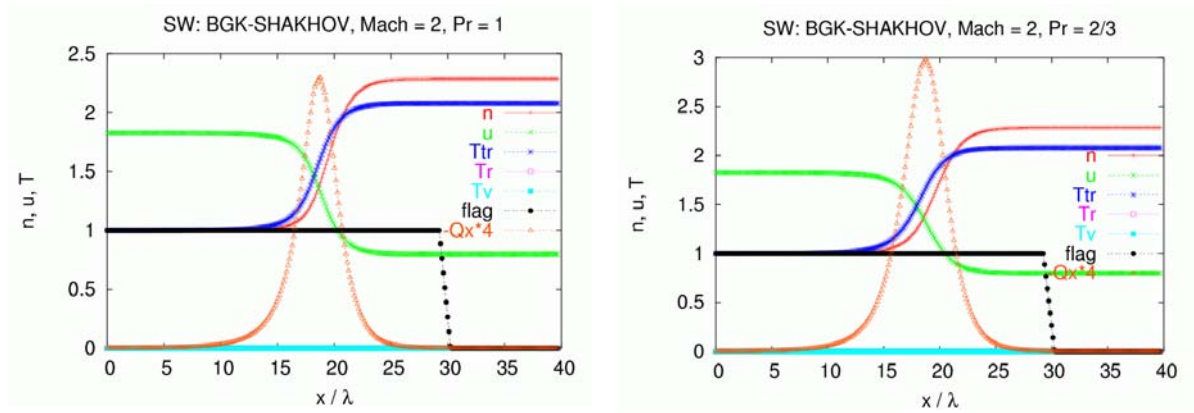
Figure 19. UFS calculation of SW structure for two Pr numbers: Pr = 1 (BGK model) and Pr = 2/3 (Shakhov Model).

The BGK model with Pr correction has been further expanded to the case of 3T-BGK model (described below) describing molecular gases with internal degrees of freedom of the molecules. The results of calculations of SW at Mach = 5, Z_r = 3, Z_v = 100 and Pr = 2/3 are shown in Figure 20.

24
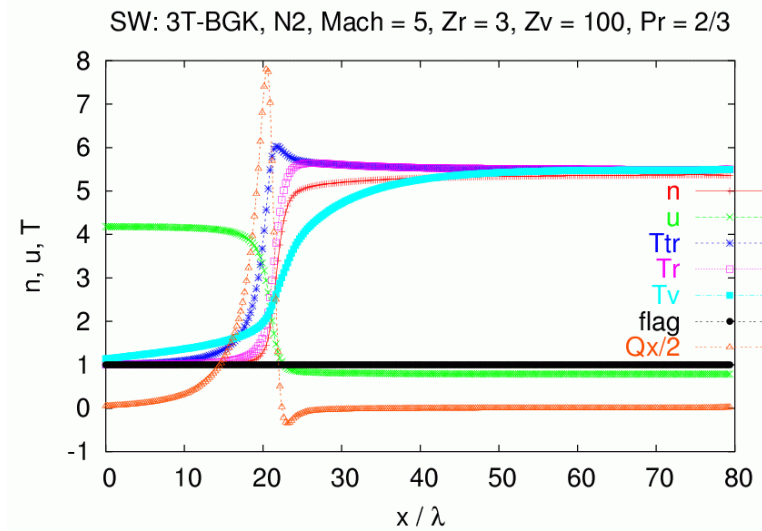
Figure 20. Calculation of 1D SW using 3T-BGK Model with Shakhov correction with Pr = 2/3.

3.3. Domain Decomposition Criteria

The main problem of unified methods is to separate kinetic and continuum regions. In our solver the adequate switching criterion is important because wrong domain decomposition could lead to non-positive distribution function when kinetic NS solution is coupled with the Boltzmann solution. We have used the following switching criteria:

$$S_p = \sqrt{p_{xx}^2 + p_{yy}^2 + p_{zz}^2} \Big/ p, \tag{27}$$

$$S_{Kn\_local} = Kn \frac{1}{\rho} \frac{\partial \rho}{\partial x}, \tag{28}$$

$$S_{gk\rho} = Kn \sqrt{\left(\frac{\nabla \rho}{\rho}\right)^2 + \frac{1}{T}\left[\left(\frac{\partial u}{\partial x}\right)^2 + \left(\frac{\partial v}{\partial y}\right)^2 + \left(\frac{\partial w}{\partial z}\right)^2\right]}, \tag{29}$$

$$S_{NS} = Kn \sqrt{\left(\frac{\nabla p}{p}\right)^2 + \left[\left(\frac{\partial u}{\partial x}\right)^2 + \left(\frac{\partial v}{\partial y}\right)^2 + \left(\frac{\partial w}{\partial z}\right)^2\right] \Big/ \left(u^2 + v^2 + w^2\right)} \tag{30}$$

where p_{xx}, p_{yy}, p_{zz} are appropriate components of the non-equilibrium stress tensor, p is the pressure, ρ is density, T is temperature, *u, v, w* are appropriate component of velocity (all values are given in dimensionless form), Kn is the Knudsen number of the problem under consideration (e.g., for a flow around a cylinder $Kn = \lambda / R$ where λ is the mean free path and R is the radius of a cylinder). If S is greater then a threshold value, then the kinetic solver must be used. The applicability of different criteria and the ways to choose the threshold value is currently being studied. It was found that the criterion S_{Kn_local} gives correctly the non-equilibrium domain near shock wave and behind the body at moderate Knudsen numbers, but at small Knudsen numbers ($Kn<<0.1$) non-equilibrium domain behind the body appears to be too small. We found experimentally that criterion S_{NS} gives correct kinetic regions and allows one to successfully couple the NS and Boltzmann solvers.

25

We have studied the influence of the breakdown parameter on the flow characteristics calculated by the UFS. Figure 21 shows an example of the normal force on the cylinder surface calculated at 5 breakdown parameters s = 0.025, 0.05, 0.1, 0.2, and 0.4 for supersonic gas flow around a cylinder at Mach=3. One can see that all curves converge at small s numbers when the Boltzmann region grows. At the same time, by decreasing the s number, the computation time increases. Therefore, for quick results one can use larger s numbers if precision of the order of 10% is satisfactory.
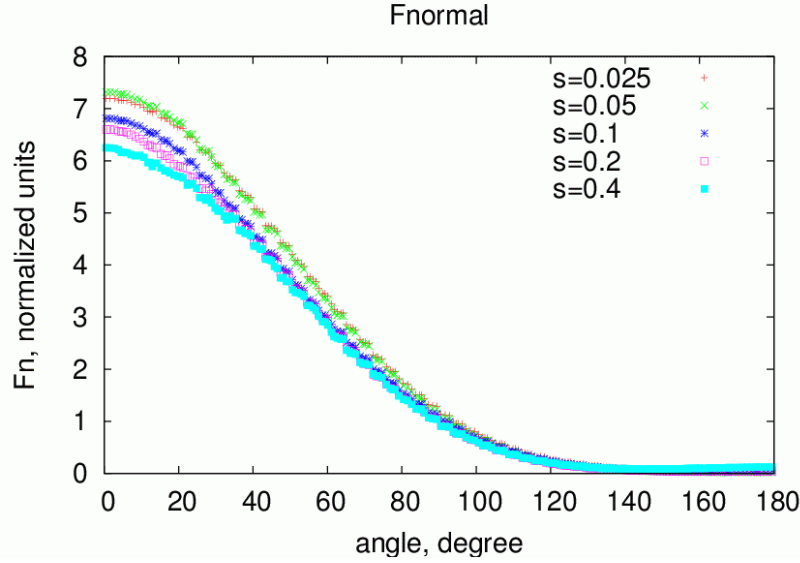
Figure 21 Normal force on the cylinder body as a function of angle for the problem of flow around cylinder for Mach=3.

3.4.   Coupling kinetic and continuum solvers

The coupling of kinetic Boltzmann and continuum Euler solvers consists of the following. The Euler equations are solved in the entire computational domain. The boundary conditions for the Boltzmann equation at the kinetic/continuum interface are obtained assuming Maxwellian velocity distribution function in the continuum cells. In the kinetic domain, the moments are obtained from the Boltzmann solution.

The coupling of the Boltzmann solver and the NS solver consists of the following. On each time step, a continuum cell is considered, which is a neighbor to a kinetic (Boltzmann) cell. In this continuum cell, a velocity grid is introduced which is identical to that in the kinetic cell. On this velocity grid, the following distributions functions are constructed $f_0 = g^l[1 - \tau(a^l \xi_n + A^l)]$ on each face where ξ_n is the normal velocity to a cell face. The parameters of the Maxwellian distribution function g^l are calculated using the macroparameters in the continuum cell and the coefficients of the polynomial a^l are calculated using the gradients of the macroparameters in the continuum and the neighboring kinetic cells. The coefficients of the polynomial A^l are then calculated using the relationship of conservation $\int g^l(a^l \xi_n + A^l)\psi_\alpha d\xi = 0$ of the moments on the discreet velocity grid. Coupling NS and Boltzmann solvers requires knowledge of the face values of the distribution function, whereas only cell values are used for coupling with the kinetic Euler solver. The coupling with the kinetic NS requires that the face values are stored and transferred to the Boltzmann solver.

The results of coupled NS/Boltzmann solution are shown in Figure 22 for the 1D shock wave. The Boltzmann solver was run with the HS model for the collisional integral. One can see that pure Boltzmann results are very close to those obtained using the coupled NS-Boltzmann solution. Only

26

about a third of the simulation domain is simulated by the Boltzmann solver, that gives significant computational speedup.
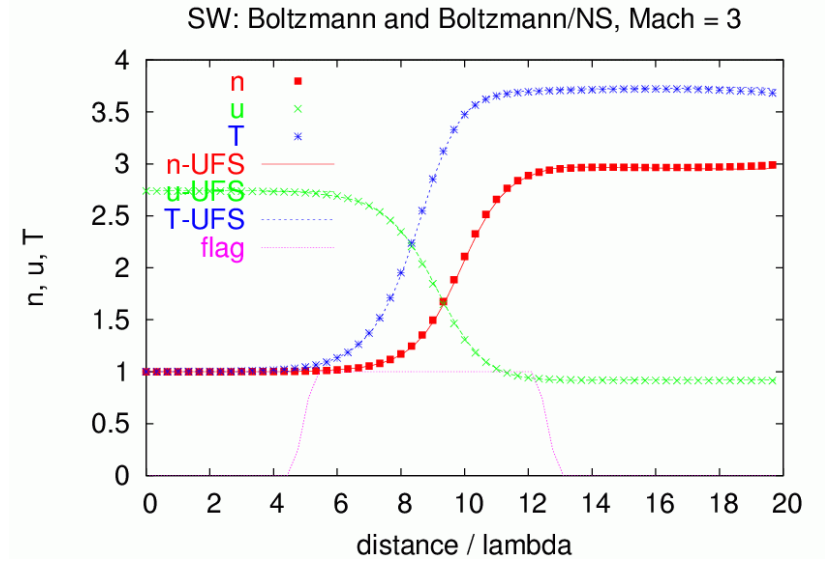
Figure 22 Results of comparison between the pure Boltzmann (symbols) and NS-Boltzmann computations for the shock wave at Mach = 3. Also shown is the kinetic flag indicating the region (flag = 1) where the Boltzmann solver is run.

3.5.   Axi-Symmetric version of UFS

The axi-symmetric version of the Boltzmann solver (with BGK collision term) has been implemented. The solver uses cylindrical coordinates (x, r, φ) in physical space and cylindrical coordinates $(\xi_x, \xi_r, \xi_\varphi)$ in velocity space. The cylindrical velocity components $\xi_x, \xi_r, \xi_\varphi$ are related to the Cartesian velocity components as

$$
\begin{aligned}
\xi_x &= \xi_x, \\
\xi_r &= \xi_y \cos\varphi + \xi_z \sin\varphi, \\
\xi_\varphi &= -\xi_y \sin\varphi + \xi_z \cos\varphi.
\end{aligned}
\tag{31}
$$

In these coordinates, the Boltzmann equation (1) has the form

$$
\partial_t(rf) + \xi_x \partial_x(rf) + \xi_r \partial_r(rf) + \partial_{\xi_r}(\xi_\varphi^2 f) - \partial_{\xi_\varphi}(\xi_\varphi \xi_r f) = rI .
\tag{32}
$$

where it is assumed that $\dfrac{\partial}{\partial\varphi} f = 0$. As pointed out in [50], for the numerical solution of Eq. (50) it is more convenient to use cyclic coordinates (R, ω) defined as: $\xi_r = R\cos\omega, \xi_\varphi = R\sin\omega$, $R = \sqrt{\xi_r^2 + \xi_\varphi^2}$. In these coordinates, Eq. (32) has the form:

$$
\partial_t(rf) + \xi_x \partial_x(rf) + R\cos\omega \partial_r(rf) - \partial_\omega(\sin\omega f) = rI .
\tag{33}
$$

We used collision integral in the BGK form, $I = (f_m - f)/\tau$, where

$f_m = n(1/\pi T)^{3/2} \exp\left\{-[(\xi_x - u_x)^2 + (R\cos\omega - u_r)^2 + (R\sin\omega)^2]/T\right\}$ is the Maxwellian distribution. The local parameters of the Maxwellian distribution f_m are determined at each time step according to relations:

$$(n, nu_x, nu_r, E)^t = \int (1, \xi_x, R\cos\omega, (\xi_x^2 + R^2))^t \, fR d\xi_x dR d\omega,$$

$$E = n(\frac{3}{2}T + (u_x^2 + u_r^2)).$$

For the numerical solution, we introduce uniform mesh in velocity space $\{\xi_i, R_j, \omega_k\}$ with steps $\{\Delta\xi, \Delta R, \Delta\omega\}$. The approximation of the convective terms $\partial_x(rf), R\cos\omega\partial_r(rf)$ is done by the standard procedures [50]. The differential approximation of the term $\partial_\omega(\sin\omega f)$ must satisfy additional conditions to give correct values to the discrete analogues of integrals from trigonometric functions, which is necessary to satisfy conservation laws and ensure positive value of the velocity distribution function [50]. We used the following approximation:

$$\partial_\omega(\sin\omega f) = \frac{1}{2\sin(\Delta\omega/2)}[(\sin\omega_{k+1/2})^+ f_{k+1} + (\sin\omega_{k+1/2})^- f_k - (\sin\omega_{k-1/2})^+ f_k - (\sin\omega_{k-1/2})^- f_{k-1}]$$

where $a^\pm = \frac{1}{2}(a \pm |a|)$ and $\omega_{k\pm1/2} = \omega_k \pm 1/2\Delta\omega$. As shown in [50], such an approximation ensures that:
1. The positivity of f is preserved.
2. The conservation laws of density n, impulse nu_x and energy E are satisfied.
3. The entropy is locally dissipated.
4. The uniform flows are preserved.

To derive kinetic scheme for the gas dynamic equations in the cylindrical system, the kinetic equation (50) is integrated over velocity space with invariants $\psi^t = (1, \xi_x, \xi_r, (\xi_x^2 + \xi_r^2 + \xi_\varphi^2))$ to obtain

$$\partial_t(rX) + \xi_x\partial_x(rY) + \xi_r\partial_r(rZ) + F = 0 \tag{34}$$

where

$$X = \int f\psi d\xi_x d\xi_r d\xi_\varphi,$$

$$Y = \int \xi_x f\psi d\xi_x d\xi_r d\xi_\varphi,$$

$$Z = \int \xi_r f\psi d\xi_x d\xi_r d\xi_\varphi,$$

$$F = \int (\partial_{\xi_r}(\xi_\varphi^2 f) - \partial_{\xi_\varphi}(\xi_\varphi \xi_r f)) \, \psi d\xi_x d\xi_r d\xi_\varphi.$$

For a Maxwellian distribution f,

28

$$X = \{n, nu_x, nu_r, nE\},$$

$$Y = \{nu_x, p/2 + nu_x^2, nu_x u_r, u_x(nE + p)\},$$

$$Z = \{nu_r, nu_x u_r, p/2 + nu_r^2, u_r(nE + p)\}$$

$$F = \{0, 0, p/2, 0\}.$$

The numerical scheme for solving Eq. (34) has the form

$$r_{ij} \frac{X_{ij}^{n+1} - X_{ij}^{n}}{\Delta t} = -\left(r_{ij} \frac{Y_{i+1/2,j}^{n} - Y_{i-1/2,j}^{n}}{\Delta x} + \frac{r_{j+1/2} Z_{i,j+1/2}^{n} - r_{j-1/2} Z_{i,j-1/2}^{n}}{\Delta r} + F_{i,j} \right). \qquad (35)$$

To calculate fluxes on cell faces, we used $f = \begin{cases} f_M^l, (\xi_n > 0) \\ f_M^r, (\xi_n < 0) \end{cases}$, where

$f_M^{l,r} = \dfrac{n^{l,r}}{(\pi T^{l,r})^{3/2}} \exp[-\dfrac{(\xi_x - u_x^{l,r})^2 + (\xi_r - u_r^{l,r})^2 + \xi_\varphi^2}{T^{l,r}}]$, and the upper indexes (l,r) correspond to

the left and right cell center values, and ξ_n is the normal component of the velocity at the face. This way we obtained kinetic scheme for the Euler equations in the cylindrical coordinate system.

Together with Eq. (34) we used the equations obtained from the non-conservative form of the kinetic equation (33):

$$\frac{\partial X}{\partial t} + \frac{\partial Y}{\partial x} + \frac{\partial Z}{\partial r} + \frac{F}{r} = 0, \qquad (36)$$

where $F = \{nu_r, nu_x u_r, nu_r^2, (E + p)u_r\}$. As pointed out by many researchers, these equations are preferable for the description of the solution near the axis of symmetry.

The axisymmetric version of the UFS code has been tested against full 3D calculations for a quarter of a supersonic nozzle. The results of the tests are shown in Figure 23.
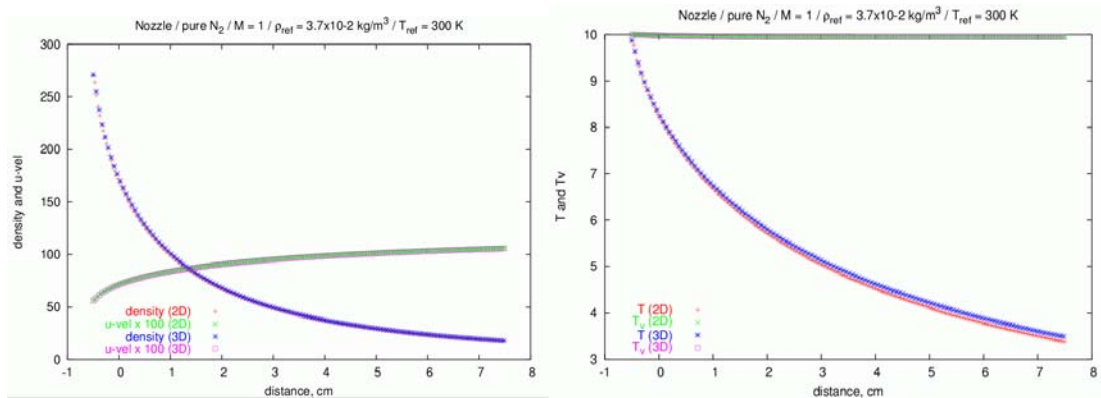

Figure 23. Comparison between 2D axi-symmetric and full 3D calculations. Shown are the density and translational and vibrational temperature profiles along the central line.

29

3.6. Parallelization

The initial version of the GFS code had possibility of parallel domain decomposition using cubical boxes or squares (in 2D). For parallel execution, the computational domain could be subdivided into several cubical (square) sub-domains, and a selected set of these sub-domains assigned to different processors. Such decomposition is static (since it does not change during the computation) and rather inefficient. First, for the domain decomposition into the cubic sub-domains is not always possible to achieve good load balance between the processors, even for the cases when the load is known for each computational cell, and the computational grid is also known. When adaptive grid is used, static domain decomposition can result in large load disbalance. Moreover, for the UFS, the computational load in each cell could wary by orders of magnitude depending on weather the cell is kinetic or continuum.

For these reasons, it was decided to abandon the parallel option built into original GFS and develop new parallel capabilities using subdomains of arbitrary shape with dynamic load balancing between the processors depending on local grid refinement and different weight of kinetic and continuum cells. This problem was subdivided into several stages.

First, the capability of performing computations in a selected part of the computational domain of arbitrary shape was implemented in UFS. To illustrate details of the implementation, consider the procedure of accessing different cells in the GFS code illustrated in Figure 24. The computational grid in the GFS is generated by subsequent division of square boxes into smaller boxes with linear dimensions equal to half of the initial dimension (left part of Figure 24). The procedure of creating the computational mesh can be represented by a tree (the right part of Figure 24). The root of the tree (0th level) corresponds to initial cube; the first level corresponds to 4 (in 2D) or 16 (in 3D) cubes obtained by division of the initial cube, etc. The computational cells correspond to leaves of the tree. The order of cell traversing is shown in Figure 24 by dashed lines with arrows. All computation procedures are called only for the leaves of the tree.
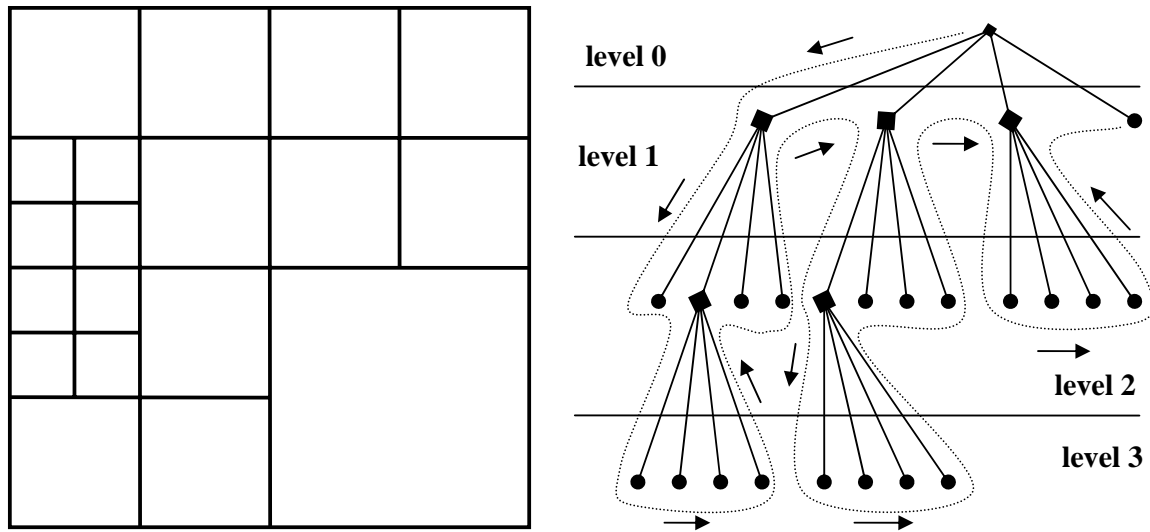
Figure 24 The cell traversing procedure

To perform computations only for a part of the domain (for instance, the sub-domain shown by blue color in Figure 25), one introduces a flag for each leaf to identify whether or not the cell belongs to the selected sub-domain. If a cell is a parent cell for a set of cells, it is flagged only if at least one child cell belongs to the selected sub-domain. After introducing flags, the procedure of cell traversing is modified in such a way as to visit only the cells belonging to the selected sub-domain. As shown on the right part of Figure 25, only the branches connected by solid lines are traversed. Moreover, it is

8572/F

necessary to specify boundary conditions at the boundary of the selected sub-domain. For this purpose, additional cells marked by dashed lines in Figure 25 are used. The branches corresponding to the boundary cells are shown by dashed lines on the graph. The boundary cells are marked using a different flag, and can be traversed separately by the code.
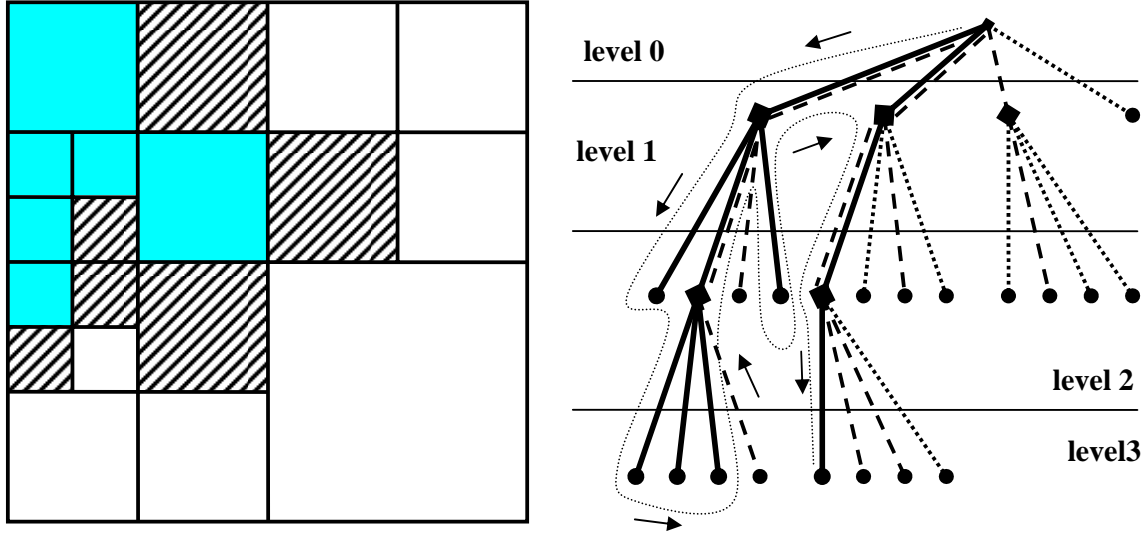
Figure 25 Simulations of a part of the domain

The implementation of the approach described above enabled us to perform simulations only in selected parts of the computational domain. An additional outcome from this part of the work is the possibility to simulate one-dimensional problems (in the original GFS, these problems had to be solved as two-dimensional problems).

The decision on the necessity to perform load balancing is made taking into account the following algorithm. We consider the maximum and average (over processors) computational time for each time step T_{max} and T_a. We introduced 2 coefficients A_{fast} and A_{slow}. The load must be balanced if $T_{max} > T_a \cdot (1 + A_{slow} + A_{fast}/T_{max})$. The value $A_{slow} + A_{fast}/T_{max}$ corresponds to deviation of the parallel efficiency of the computational part of the program from unity. The first term in this sum is the main term by which we specify the limit for the above deviation. The second term is necessary for the fast computations, where the repartitioning time is comparable with the computational time and where too frequent repartitioning can give rise to significant deceleration of the algorithm. The coefficients A_{fast} and A_{slow} can be specified by user in sim-file, and should be chosen different for different computers, depending on the computational performance and data exchange speed. This criterion for load balancing proved effective for Euler and Navier-Stokes solvers, for Boltzmann solver, and for unified computations engaging both kinetic and gas-dynamics solvers.

The next stage of the UFS parallelization consisted in static parallelization when different sub-domains were assigned to different processors and remained unchanged during the computations. After completion of this stage, the possibility of dynamic domain decomposition was implemented. The dynamic load balance between different processors was achieved separately for kinetic and continuum equations. The procedure of domain decomposition was performed using space-filling curves (SFC) as illustrated in Figure 26. During sequential traversing of the cells by natural order, the physical space is filled with curves in N-order (Morton ordering). After this ordering of cells, all cells can be considered as a one-dimensional array. A weight is assigned to each cell, which is proportional to the CPU time required to perform computations in this cell. Furthermore, the array modified with corresponding weights, is subdivided into sub-arrays equal to the number of processors, in such a way that the weight of the sub-arrays are approximately the same. This method allows rather efficient domain decomposition between different processors. Figure 27 shows an example of domain

8572/F

decomposition between several processors for supersonic gas flow around a cylinder. Figure 28 shows an example of dynamic load balancing for a 3D problem of gas flow around a Space Shuttle Orbiter.
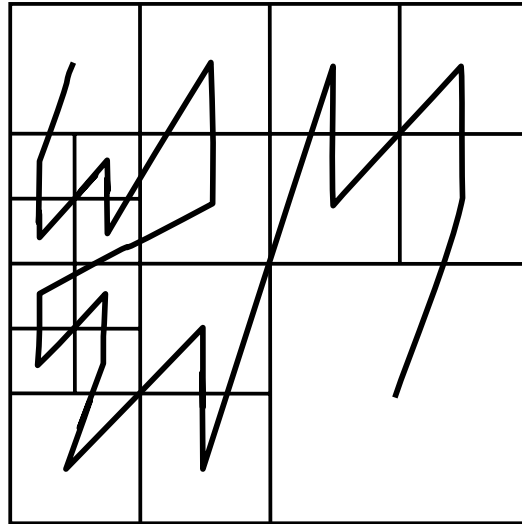

*Figure 26 Space Filling Curves*
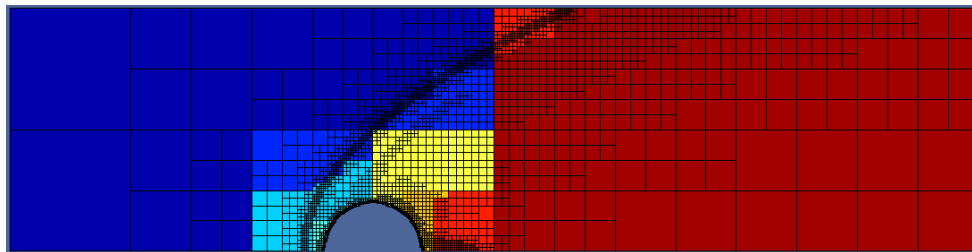
Figure 27 An example of DLB between 8 processors for the problem of flow around cylinder. Each processor ID is shown by a different color.
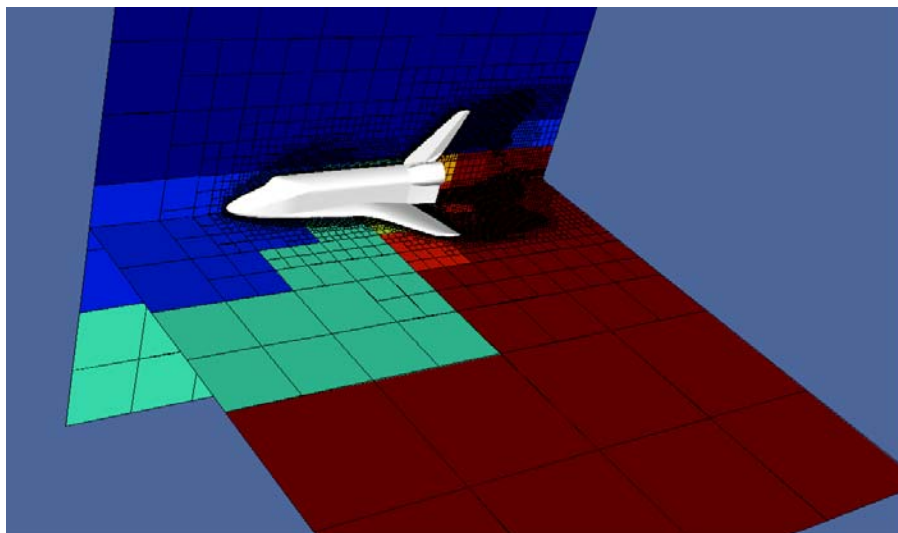

Figure 28 An example of DLB between 8 processors for the problem of flow around the Space Shuttle Orbiter. Each processor ID is shown by a different color.

8572/F

4. UFS VALIDATION AND DEMONSTRATION FOR MONATOMIC GAS FLOWS

4.1. High Speed Flows Around Blunt Bodies

4.1.1. Flow around a cylinder

The flow around a cylinder at *M*=3 was studied in a wide range of *Kn* numbers (0.001-10) using different criteria of domain decomposition and the temperature of the cylinder surface. Figure 29 shows the results of computations with Boltzmann solver and Euler solver using diffuse reflection with the wall temperature of *T*=4. The switching criterion is S_{NS}, the breakdown parameter is $\delta_s = 0.3$. The parameter of the mesh refinement is $\delta = \log(\rho) + \log(u)$.
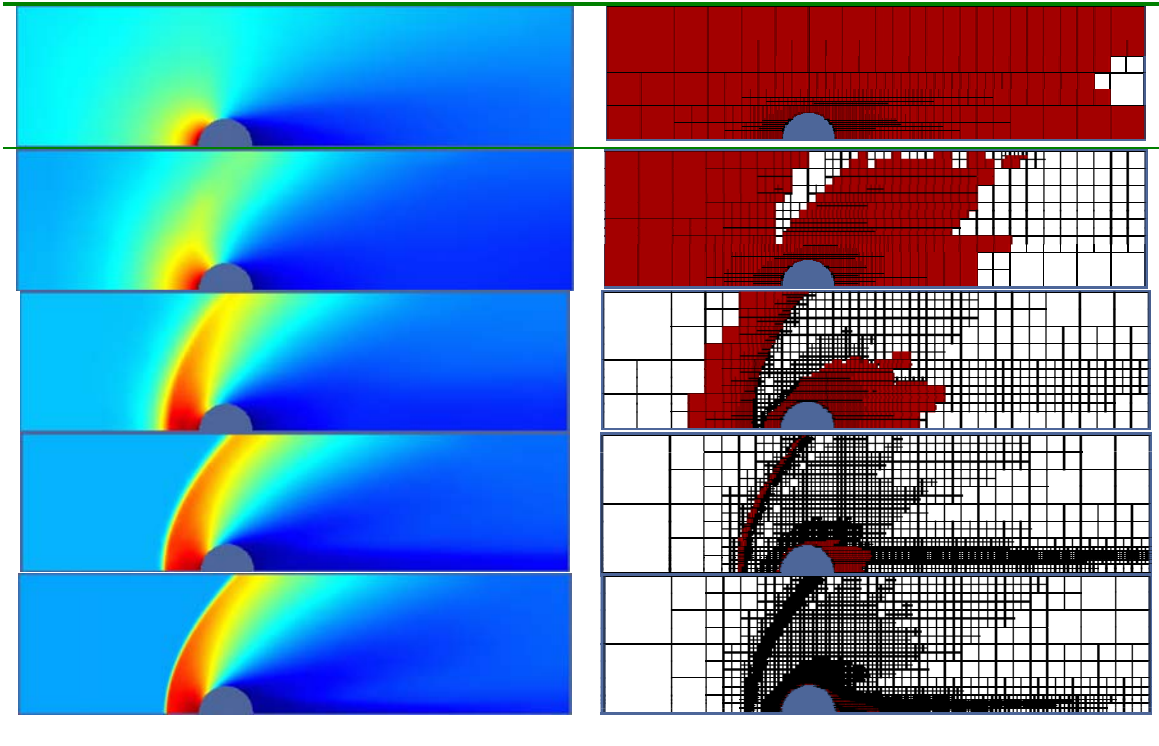
Figure 29 Gas flow around a cylinder for M=3 for different Kn numbers (Kn = λ / R = 5, 1.5, 0.5, 0.05, 0.005). On the left side are the density profiles, on the right side are the computational grid with kinetic (red) and continuum (white) domains.

Important quantities of the gas flow interaction with solid bodies are the vector of forces (F_x, F_y, F_z), the normal force F_n (pressure) and the shear force or shear stress F_t and the heat flux H. Both integral and local quantities can be calculated by the UFS code. We have tested this implementation for the problem of gas flow around a cylinder at *M*=3. The results are shown in Figure 30, Figure 31, and Figure 32 for different levels of mesh refinement near the cylinder surface. One can see that the shear force is a relatively smooth function around the cylinder. Although not directly compared here, the shear force appears to be smoother than what is expected from a cut-cell, conventional Navier-Stokes formulation [51, 52]. As noted in [51, 52, 53], the non-smoothness and non-orthogonality at mesh refinement and cut-cell boundaries of hierarchically-based, adaptively refined grids can introduce non-positive discrete representations when applied to solving the Navier-Stokes equations. This is due to representation of the viscous fluxes by higher order derivatives of the cell-centered data in a non-positive fashion, which for low cell Reynolds and Peclet numbers, can cause at best, non-smooth

8572/F

solutions, and at worst, instabilities that may not be damped by the temporal scheme [51]. It seems the approach implemented in UFS might overcome these deficiencies, although more investigations are in order.
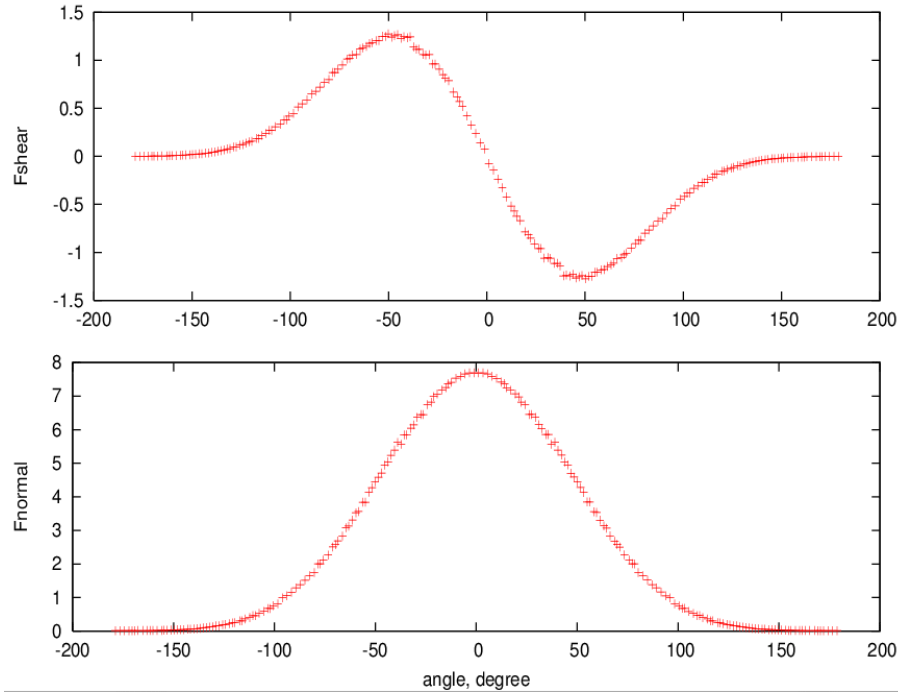
Figure 30 Shear and normal force for the problem of gas flow around a cylinder.
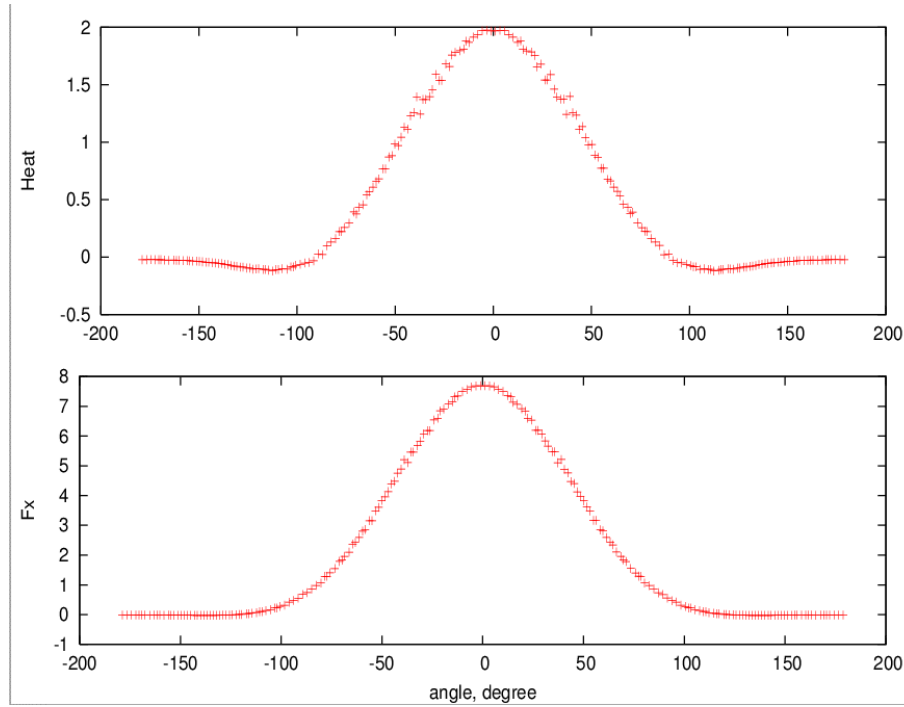
Figure 31 Heat flux and Fx for the problem of gas flow around a cylinder

We have further verified that increasing the mesh resolution around solid bodies does not lead to an increase in the noise. This result is also encouraging since, typically, NS results become noisier when increasing the spatial grid resolution near the surface.

34
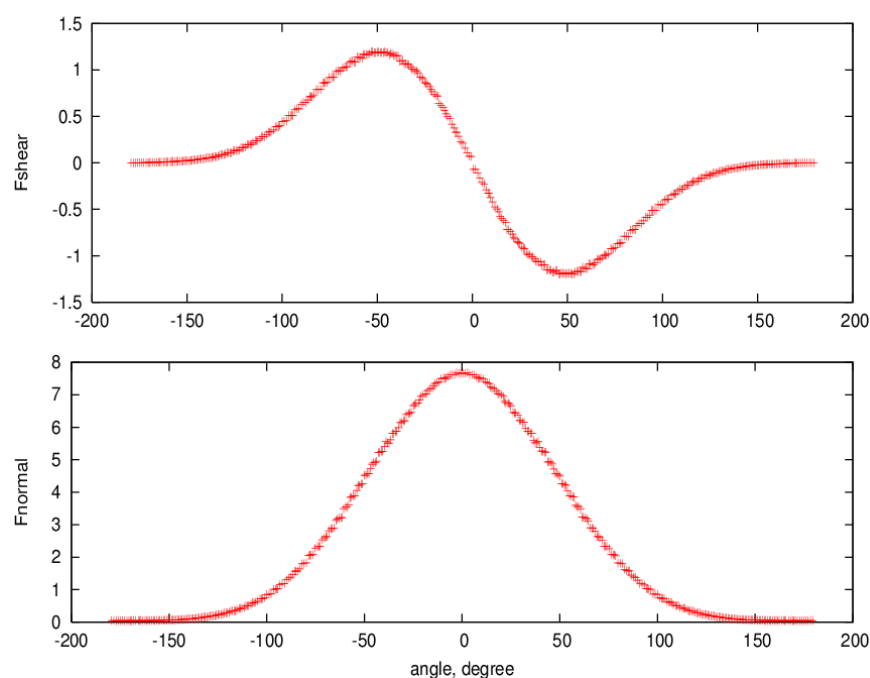
Figure 32 Shear and normal force for the problem of gas flow around a cylinder for the mesh refinement level of 9 near the surface.

Figure 33 compares the calculated drag coefficient with experimental data [54]. Also, results of DSMC simulations are shown in Figure 33 for *M=2* and UFS simulations for *M=3*. It is seen that UFS results agree well with the experimental data and DSMC simulations.
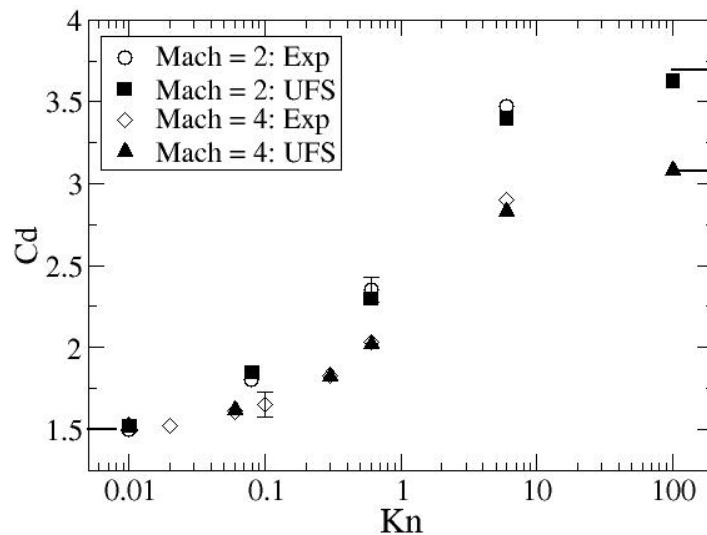
Figure 33 Drag coefficient versus Kn number. Comparison of UFS simulations with DSMC simulation and experiment. Solid lines indicate the free molecular flow and continuum limits.

The problem of supersonic flow past cold bodies (temperature less than the stagnation temperatures) is difficult since it requires careful resolution of the Knudsen layer around the surface. In this layer the density rises sharply and the mean free path decreases strongly. The farther the temperature of the

body is from the stagnation temperature $T_{stag} = 1 + \dfrac{\gamma - 1}{2} M^2 T_\infty$, the more non-equilibrium the distribution function is around the solid body surface. For $\gamma = 5/3$, one obtains $T_{stag} = 4$ at $M=3$ and $T_{stag} = 34$ at $M = 10$.

We first studied this problem for $M=3$ with a surface temperature $T_w = 1$. This case is less demanding numerically than the $M=10$ case and has been run on a 8-node cluster. Figure 34 shows the profiles of macroparameters along the centerline. One can see that the temperature starts to drop (from a high value of 35 to about 5) at a distance of about 30 mean free paths (λ) from the cylinder surface (see plot of (x-R)/λ in Figure 34). This region requires kinetic description with the Boltzmann solver. Choosing smaller kinetic regions results in non-monotone profiles of macroparameters and pressure and heat transfer coefficients (see Figure 35). Figure 36 shows the computational grid and kinetic region (in red) for the base case for $M=3$.
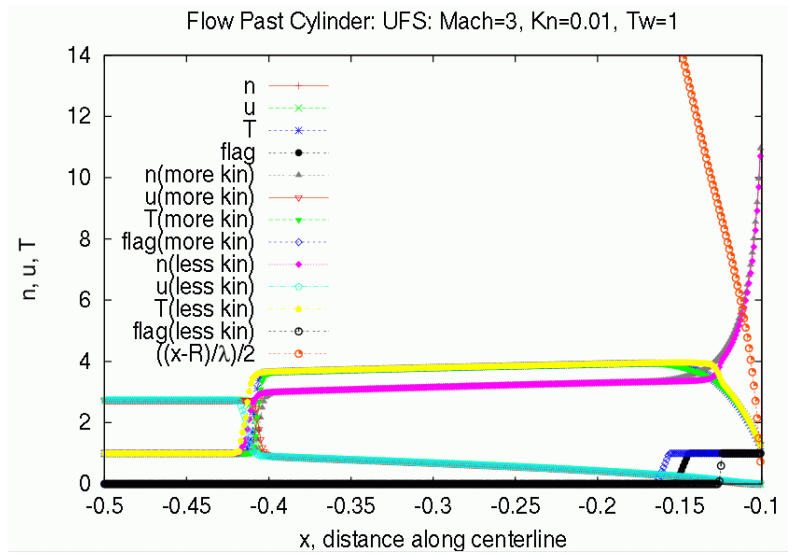
Figure 34. Profiles of density, velocity and temperature for 3 cases with different numbers of kinetic cells for M = 3 . Shown also is the profile of normalized distance (x-R)/λ from the cylinder surface.
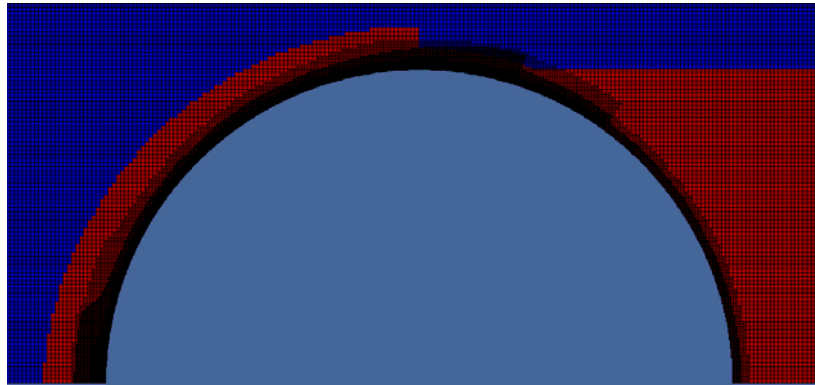
Figure 36. Computational grid and kinetic region for the M=3 base case.

The *M*=10 case is more difficult numerically since it requires larger spatial and velocity grids. This case has been run on an HP cluster with larger number of nodes. For 128 processors, the typical wall clock time is 14 hrs and the memory usage is 710 MB per processor. Figure 37 shows the profiles of macroparameters along the centerline for the *M*=10 case. One can see that the temperature starts to drop (from a high value of 35 to about 5) at a distance of about 35 mean free paths (λ) from the cylinder surface (see plot of $(x\text{-}R)/\lambda$ in Figure 37). This region requires kinetic description with the Boltzmann solver. The pressure and heat transfer coefficients are shown in Figure 38. The heat transfer coefficient is slightly noisy and can be improved by further refining the spatial grid at the cylinder surface. The current results are obtained on a spatial grid in which the cell size is about 2 mean free paths (λ) near the cylinder body. The *M*=3 case shows that to obtain smooth heat fluxes, the cell size of the order of λ is required. It is worth noting that DSMC codes typically require the cell size to be smaller than local λ.
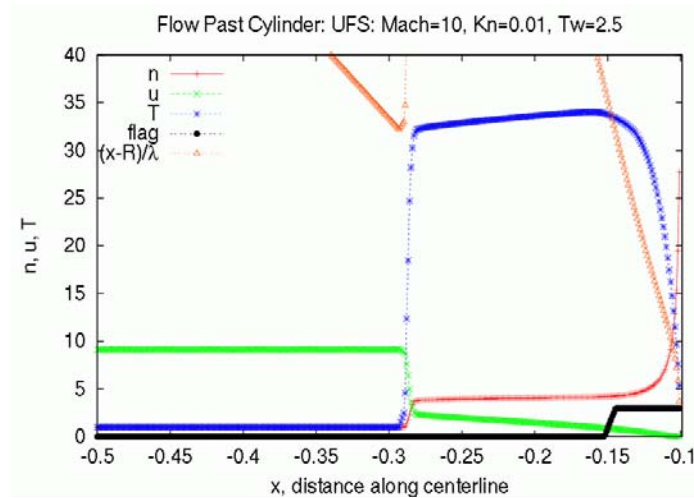
Figure 37. Profiles of density, velocity and temperature for M = 10 case. Shown also is the profile of normalized distance (x-R)/λ from cylinder surface.
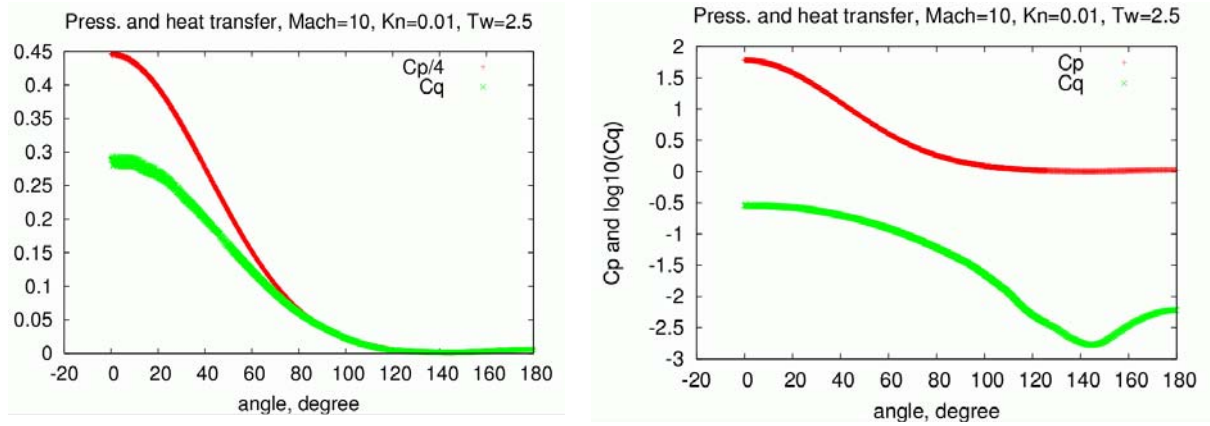
Figure 38. Pressure and heat transfer coefficients for the M=10 case (linear scale on the left and log scale on the right).

We have compared the UFS results with DSMC results (SMILE code) for the case Mach=10, Kn=0.01 case described in [55]. The Euler/BGK option was used in UFS simulations. The BGK solver was used only near the cylinder surface (not in the shock wave area). As seen in Figure 39, the UFS results agree well with the SMILE results. As expected, the shock structure is not resolved well with the Euler solver, but the jumps of macro parameters are predicted well. The flow is not fully converged behind the cylinder in these simulations.
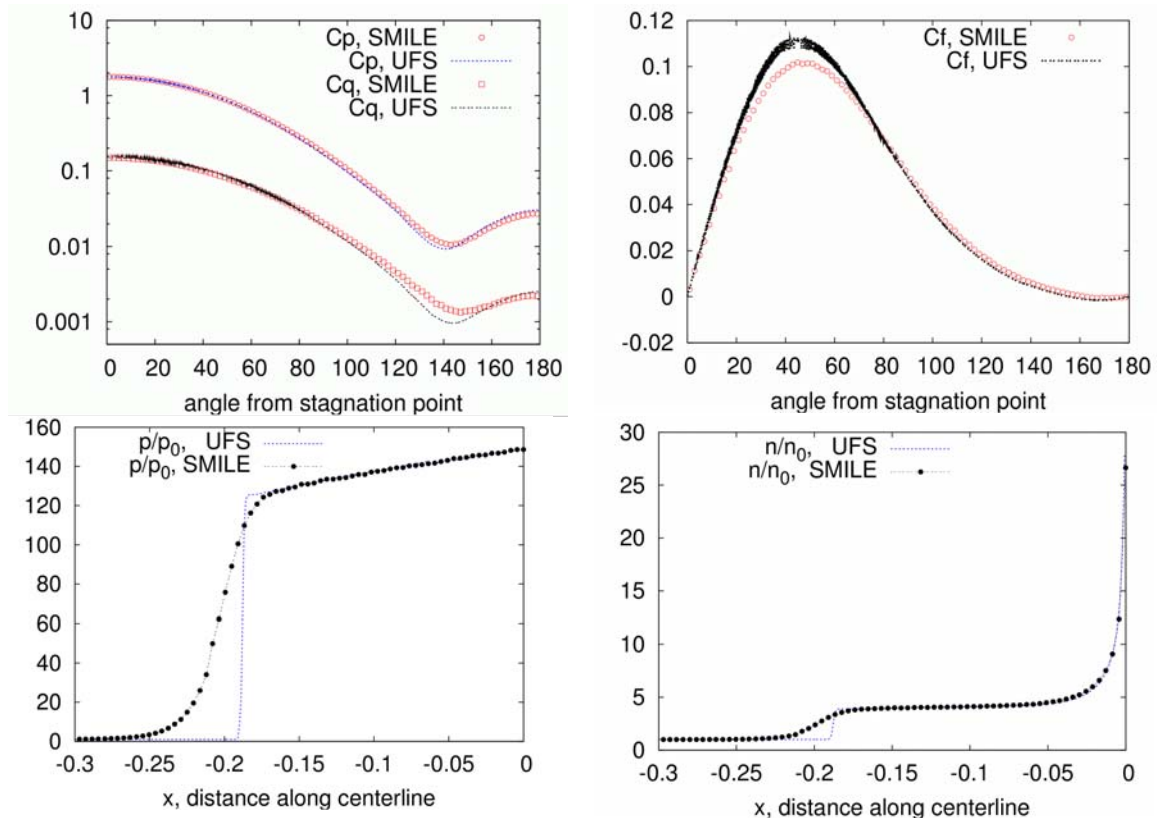
Figure 39 . Profiles along cylinder surface (top) and along centerline (bottom).

4.1.2. Hollow cylinder flare and biconic configurations

The hollow cylinder flare configuration has been set up according to Ref. [56]. The UFS calculations of the simplified (upper half) configuration are shown in Figure 40. The results are close quantitatively with those presented in Ref. [56] (see temperature and pressure distributions in Figure 40). Further detailed study of these cases is envisaged.
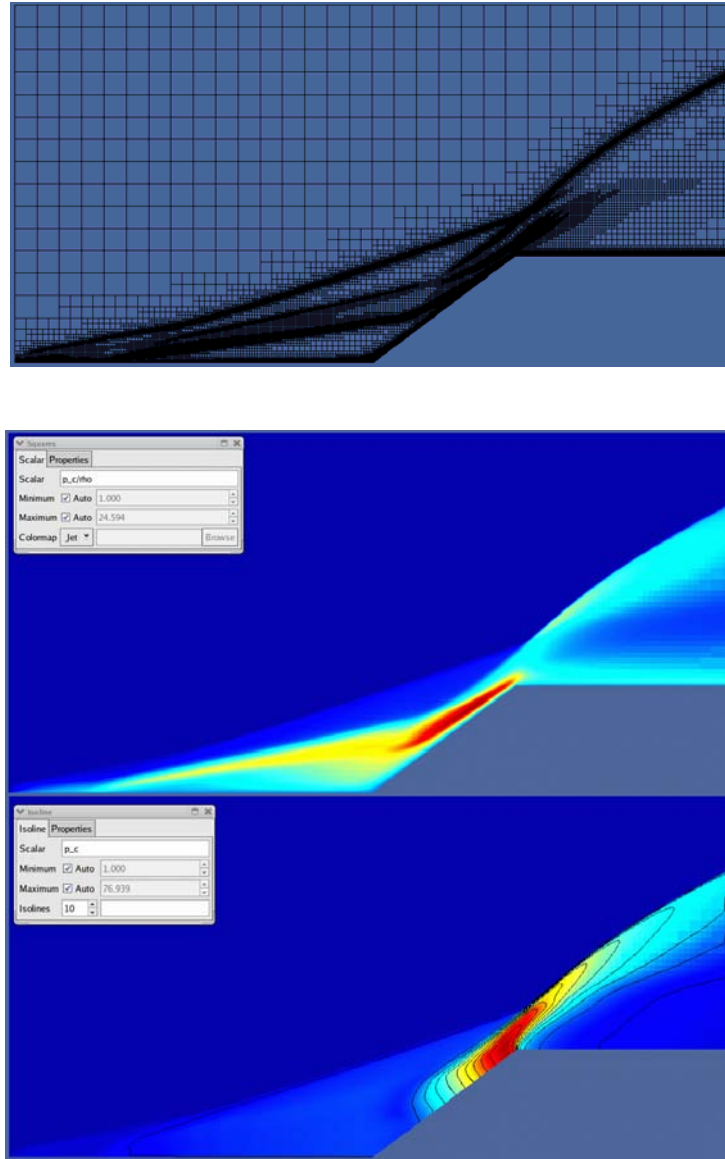
Figure 40. Computational grid and profiles of temperature and pressure for the hollow flare case.
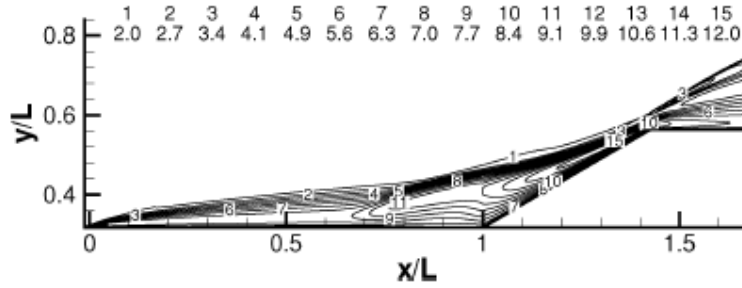
Fig. 2 Temperature contours T/T_∞.
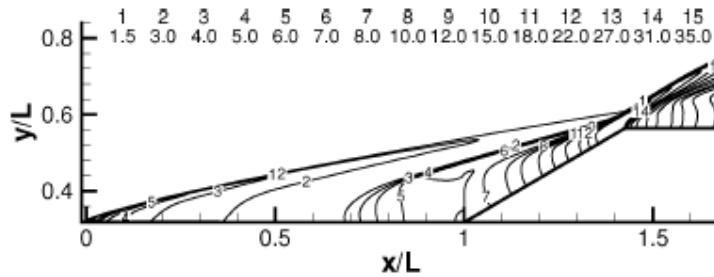
Fig. 3 Pressure contours p/p_∞.

Figure 41. Pressure and temperature distributions from Ref. [56].

Figure 42 shows results of preliminary simulations of a complete hollow cylinder flare configuration. The computational grid inside the cylinder body is intentionally made coarse. Detailed comparison with the DSMC results of [57] is planned.
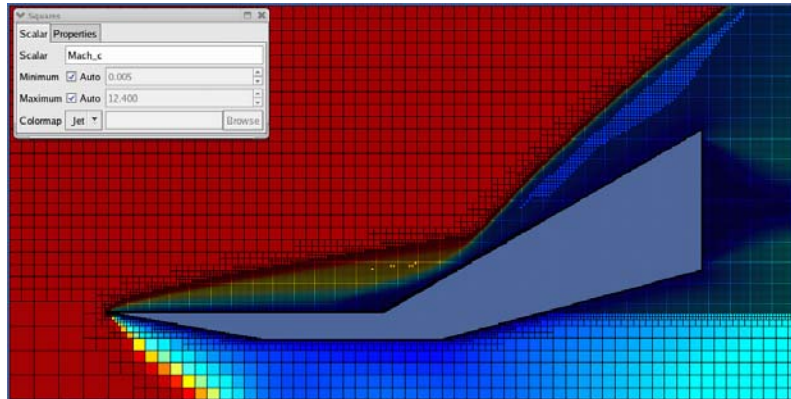
Figure 42. Computational grid and Mach number for the hollow flare case for complete geometry.

4.2.   Micro Channels

The UFS has been tested for simulations of internal flows in channels and nozzles. Figure 43 shows an example of 2D simulations of a short channel for two different *Kn* numbers. The geometry and flow conditions correspond to Ref. [58] The BTE-NS option of the UFS solver with 2nd order was used for these simulations. The boundary conditions on the left boundary are $\rho_{in} = p_{in} = 1.5$, the boundary condition on the right boundary is $p_{out} = 0.5$.
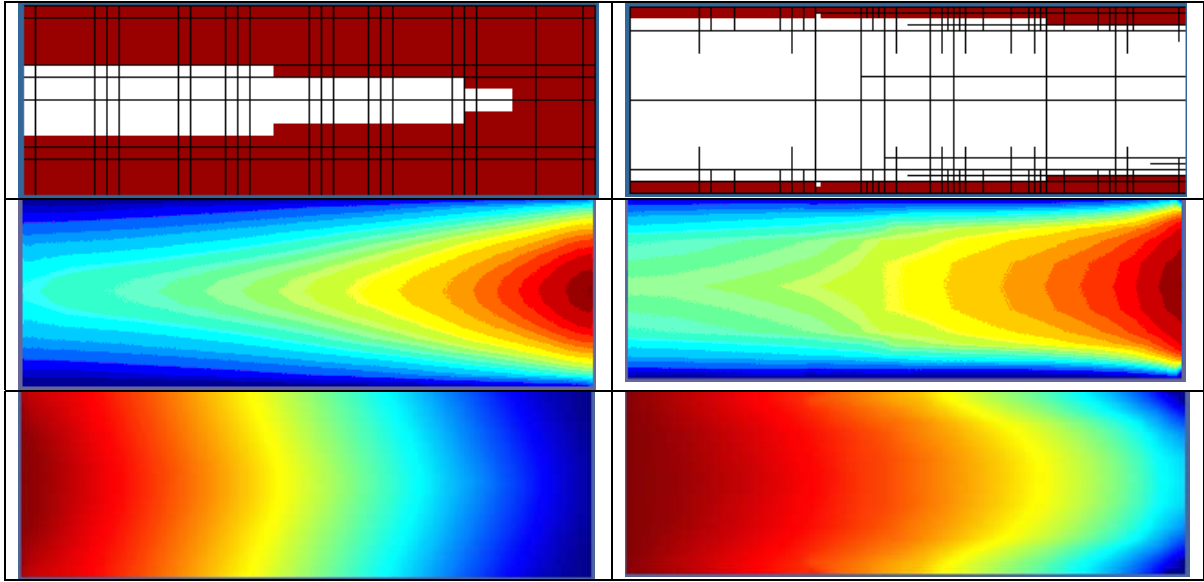
Figure 43 UFS simulations of 2D micro channel. Kinetic and continuum domains (top), axial velocity (middle), density (bottom). Left: Kn=01, density 0.62<r<1.51, velocity 0.08<v<0.60; Right: Kn=0.01, density 0.59< r <1.5, velocity 0.11<v<0.92

We have performed a series of calculations of gas flow in a long channel for a wide range of Knudsen numbers. The Knudsen paradox (the minimum of the mass flow rate) was observed at Kn~1, see Figure 44.
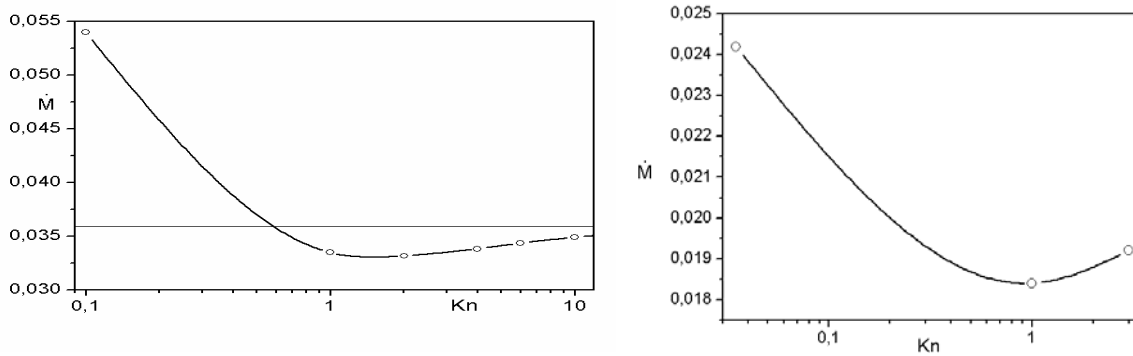
Figure 44 The Knudsen effect in a relatively long channel (L/d=21) for P0/P1=2 (left) and P0/P1=1.5 (right).

Different molecular models have been compared. For example, the calculations by two potentials (Hard Spheres and Lennard-Jones) demonstrated similar behavior of the main quantities. The flow field structures are quite similar, and the difference in a mass flow rate is about 5% (the flow rate is smaller for the hard sphere molecules).

4.3.   Nozzle and Plume Flows

UFS has been sucessfully used for simulations of nozzle and plume flows. Figure 45 shows results of a micro nozzle simulations for two *Kn* numbers. The geometry and flow conditions are described in [59]. The BTE-Euler option of the UFS with the first order numerical scheme was used, the grid adaptation is based on $\delta = \log(\rho) + \log(u)$.
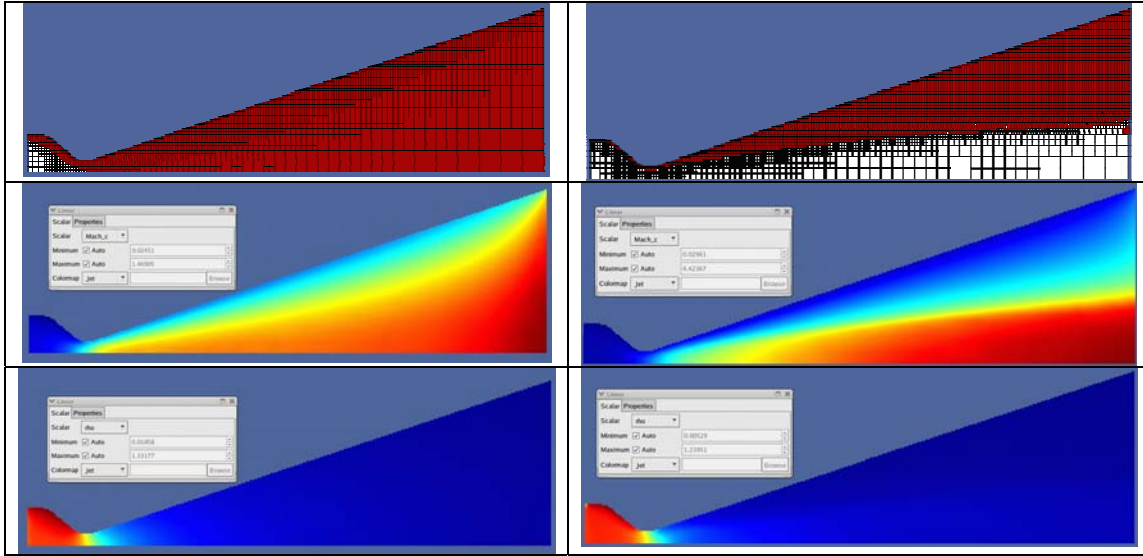
Figure 45 UFS simulations of 2D micro nozzle for Kn=0.01 (left) and Kn=0.001 (right).Kinetic and continuum domains (top), local Mach number distribution (middle), density (bottom).

UFS has been demonstrated for coupled simulations of nozzle and plume [60]. Figure 46 shows the asi-symmetric nozzle geometry of the NASA Ames EAST facility and the computational domain for the plume simulations. The UFS simulations were carried out in the entire domain including nozzle and plume. Figure 47 shows the contours of Mach number and spatial distributions of the translational and vibrational temperatures. The continuum solver was used inside the nozzle and in the dense part of the plume. The low-density part of the plume was calculated with the Boltzmann solver. DSMC simulations were performed for the comparison in the plume region. The results of the UFS and DSMC simulations are compared in Fig. 49
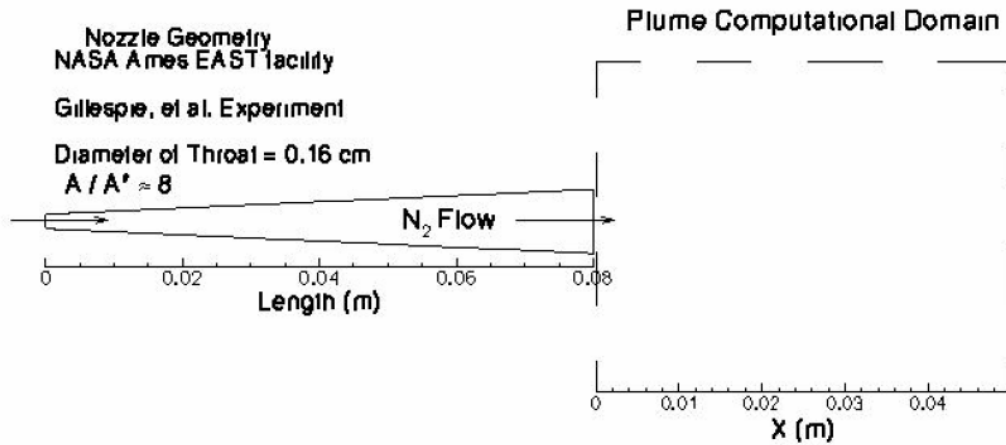
Figure 46 Nozzle geometry and computational domain for combined nozzle/plume simulations

8572/F
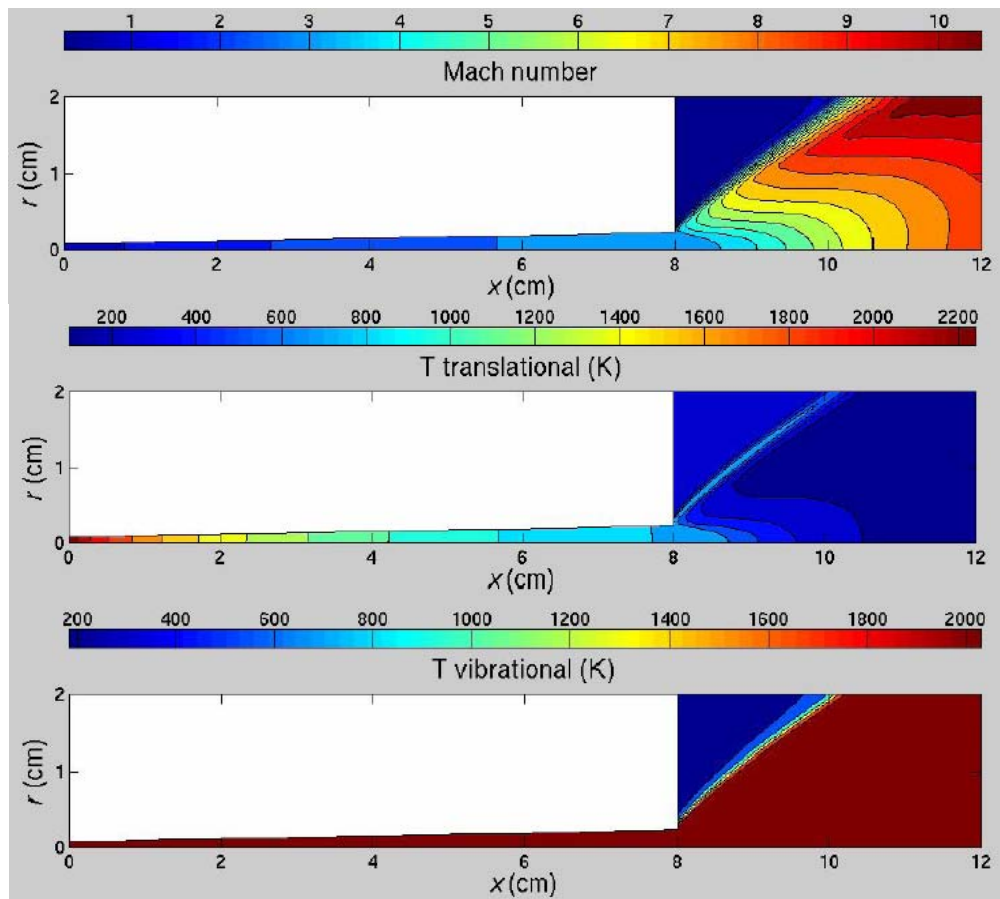
Figure 47 Mach number, translational and vibrational temperature contours for nozzle and plume
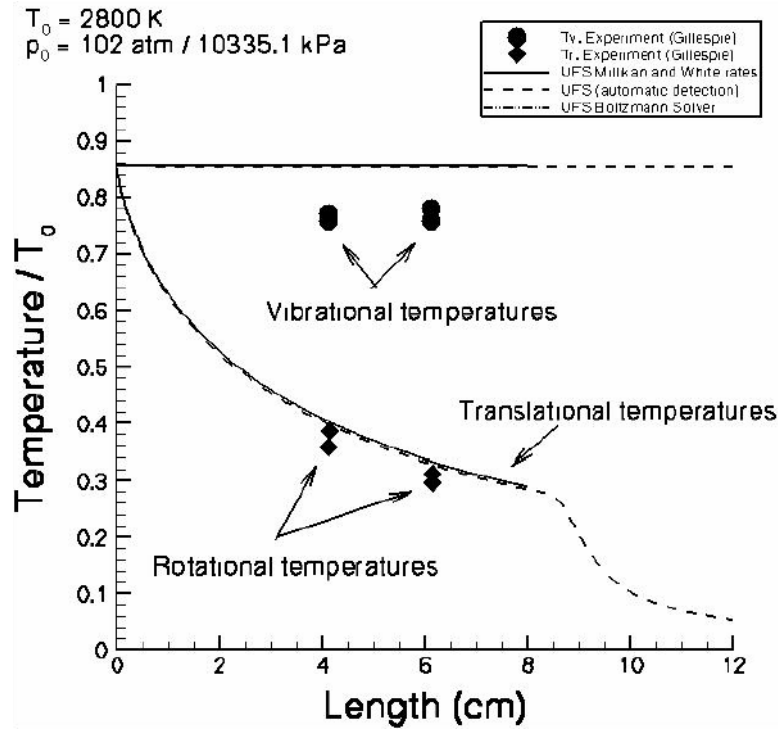
Figure 48 Calculated and experimental temperatures along the nozzle axis
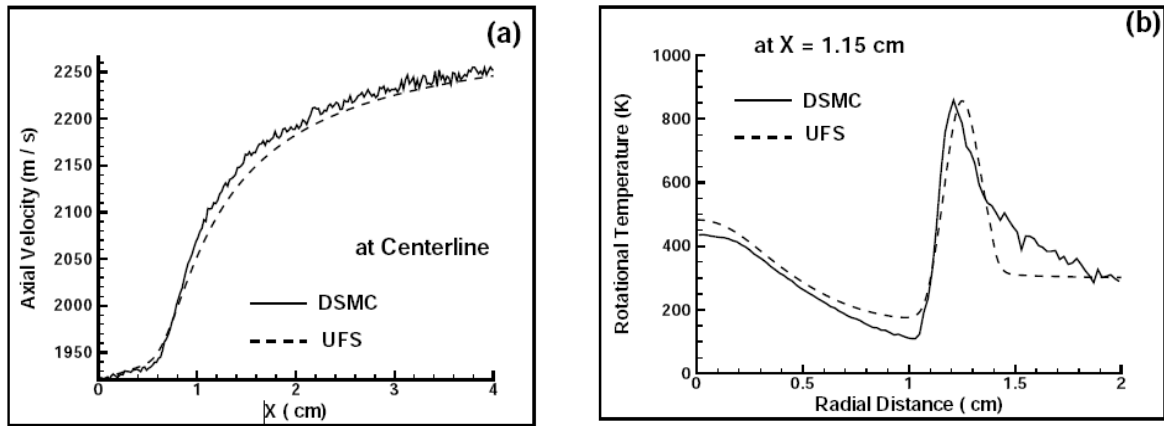
Figure 49 Comparison of UFS and DSMC results: Axial flow velocity along the centerline (left) and radial distribution of the rotational temperature at x=1.15 cm (on the right)

4.4.   Low Speed Flows

Deterministic Boltzmann solver has advantages over statistical methods for low speed flows. Figure 50 from [61] illustrates this statement: "Even after a million time steps of sampling, the statistical scatter is still so large compared to the small changes of flow quantities that meaningful results can not be obtained… In contrast to the DSMC method, the CFD method based on Boltzmann equation is free from the statistical scatter"

8572/F
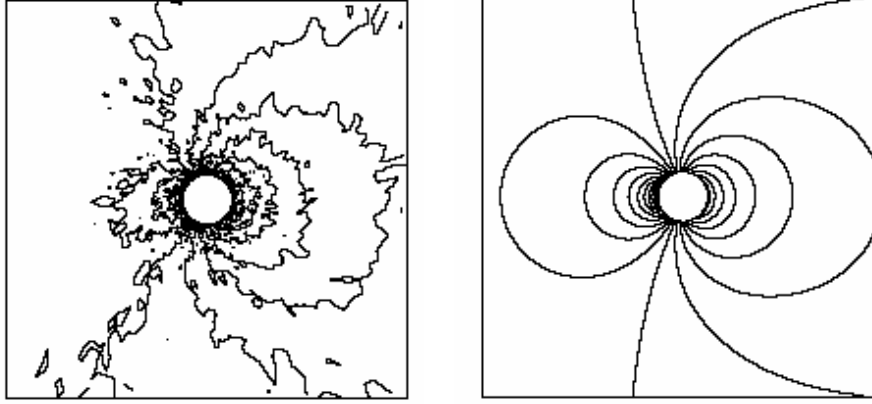
Figure 50 Density contours for flow around cylinder, M=0.1, Kn=0.1. DSMC results on the left, Boltzmann results on the right (after Morinishi [61])

Figure 51 shows results of UFS simulations of low speed flow around a sphere. Kinetic and continuum domains are shown in the vertical plane, the velocity contours are in the horizontal plane.
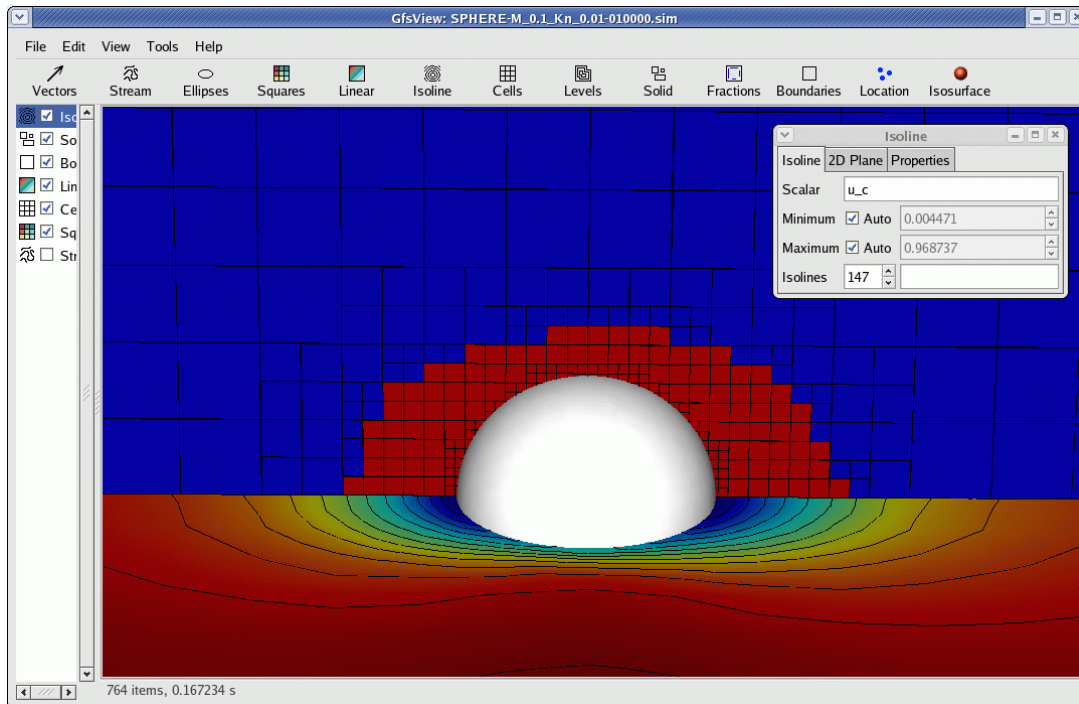
Figure 51 UFS simulation flow around sphere at M=0.1, Kn=0.1

Figure 52 illustrates a low-speed flow induced by temperature gradients. The nonuniform boundary temperature distribution can induce flows in reactor: a significant flow (~2-3 m/s) of simulated by simple gas radicals flow over semiconductor wafer expected. Flow speed of order of 0.01 thermal speed is observed. This flow is absent according to the traditional NS equations with slip boundary conditions. Both the direct Boltzmann solver and the kinetic NS solver produce correct physical picture of the flow shown in Figure 52. The temperature T of surfaces goes from 1.7 to 1 (hot bottom and cold top), bottom is symmetry, top and left boundaries have T=1. Note that flow speed smaller at free molecular flow ($Kn = \infty$) and continuum conditions (Kn=0). Flow speed maximum at some Kn ~ 0.1.

45
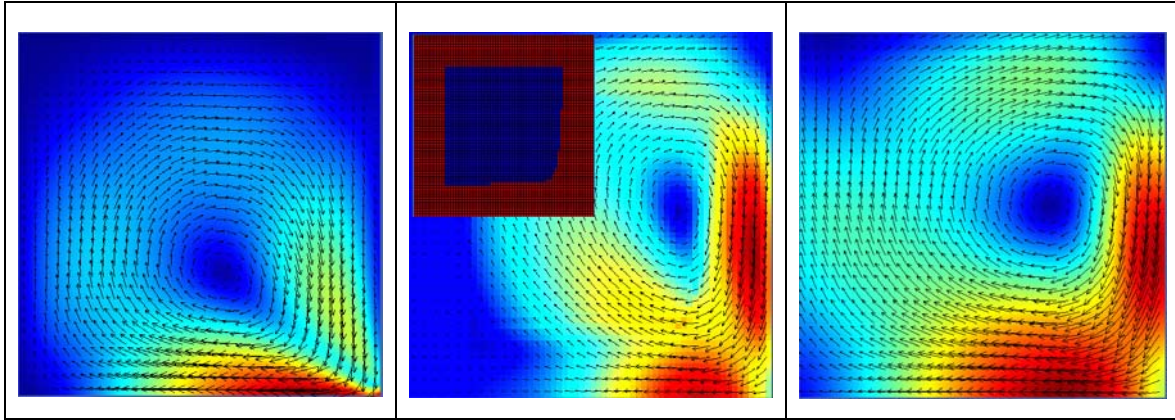
Figure 52. Temperature driven vortex: temperature and velocity fields for three values of Knudsen numbers (Kn=0.01 (|v|max~5E-4), 0.07 (|v|max~0.007), 0.3 (|v|max~0.005) from left to right). Kinetic and continuum zones are shown in the middle Figure corner: blue – continuum, brown – kinetic zones.

4.5.   Space Vehicles – Reentry Problems

We have tested and demonstrated UFS for reentry problems. Figure 53, Figure 54 and Figure 55 show results of simulations for the Orbital Reentry Experiment (OREX). Three types of simulations have been performed: 1) simulations using the gasdynamic solver (2nd order Euler solver) of the flow at low Knudsen numbers (continuum regime), see Figure 53; 2) simulations using the Boltzmann solver at high Knudsen numbers (kinetic regime), see Figure 54; and 3) simulations using UFS (coupled Boltzmann and continuum solvers) for moderate Knudsen number (intermediate regime), see Figure 55.
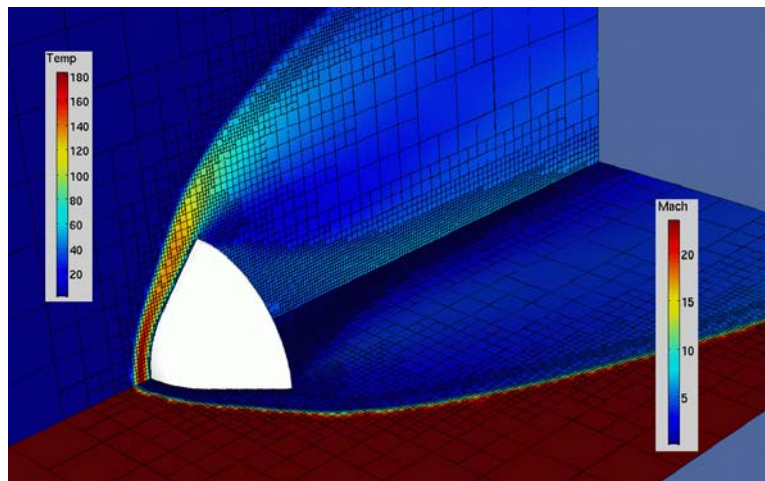
Figure 53 Results of simulations of the OREX at M = 25 using the 2nd order Euler solver in UFS.

46
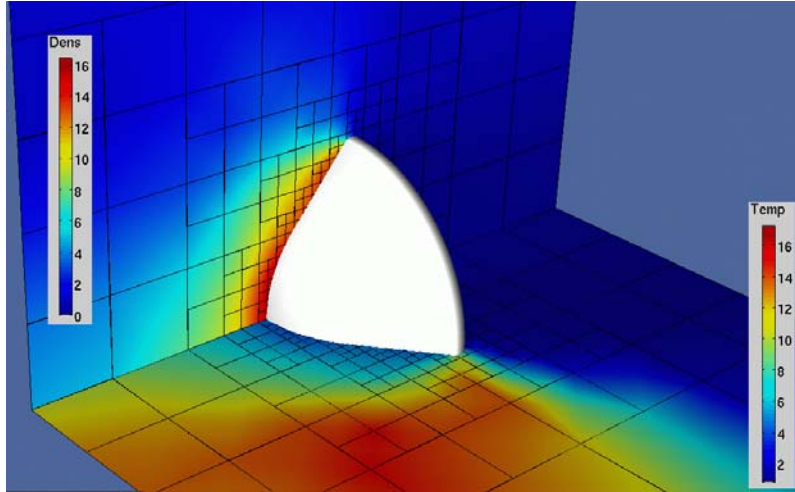
Figure 54 Results of simulations of the OREX at M = 10 and Kn = 10 using the Boltzmann solver in UFS.
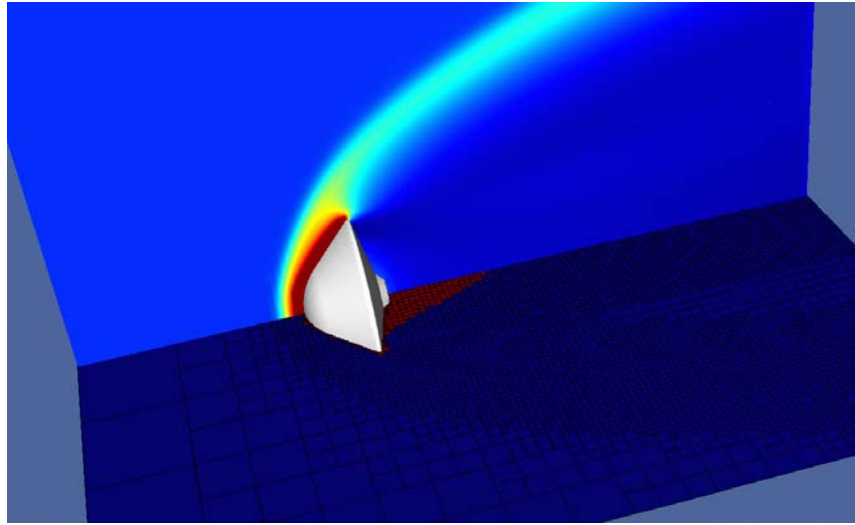
Figure 55 Results of simulations of the OREX at M = 10 and Kn = 0.1 using a coupled kinetic Euler and Boltzmann solvers. Shown are the density profile (vertical plane) and computational grid and kinetic domain (in red) on horizontal plane.

As part of validation and demonstration of the UFS, we have performed simulations of the Inflatable Reentry Vehicle Experiment (IRVE) using Euler+Boltzmann solvers on 7-processor Linux cluster. The flow conditions are for 91 km altitude: Kn = 0.01 and Mach = 3.94 [62]. The flow is at zero angle of attack. Figure 56 shows streamlines, Mach number, and computational mesh (on the left) and the gas temperature T (in units of free flow gas temp) in the vertical plane, as well as kinetic (red) and continuum (blue) domains in the horizontal plane.

47
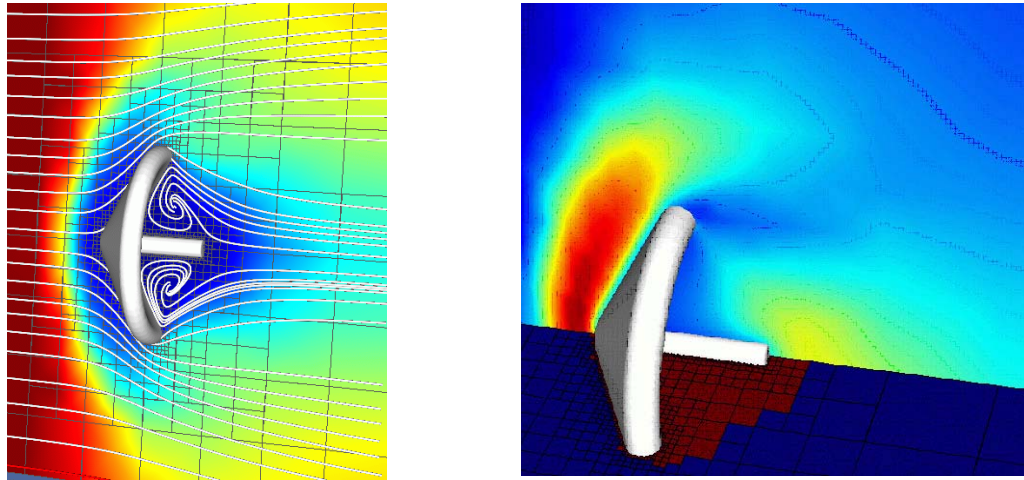
Figure 56 Streamlines, Mach number, and computational mesh (on the left). Gas temperature in the vertical plane, kinetic (red) and continuum (blue) domains in the horizontal plane (on the right).

4.6.   Unstable flows

The UFS can be a useful tool for studies of unstable flows, in particular, for

- analysis of large scale structures by means of kinetic Euler or Navier-Stokes solvers
- kinetic analysis of instabilities on the basis of the Boltzmann (or BGK) solver
- multi-scale description of unstable (turbulent) flows

First results of this direction have already been obtained. Figure 57 shows the gas density distribution for a subsonic flow (M=0.6) around a prism obtained with the kinetic Euler scheme. A vortex structure is formed in the wake behind the prizm, as discussed in [63]
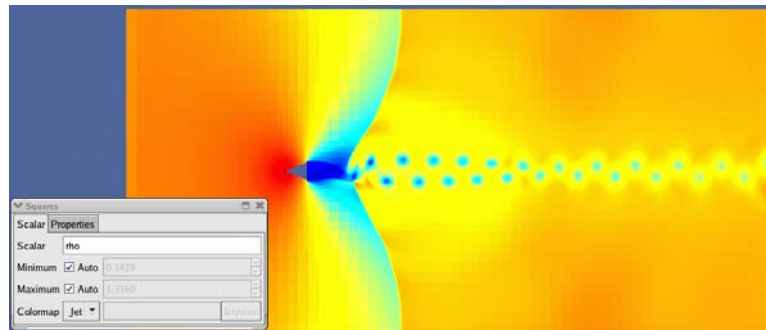
Figure 57. Large scales structures for gas flow around a prism by the kinetic Euler scheme, 2nd order.

Figure 58 shows supersonic flow around a prism at an angle of attack = 3 deg according to the kinetic Navier-Stokes scheme. Unstable structures appear in a wake behind the prism at M=3, Kn=0.00001.
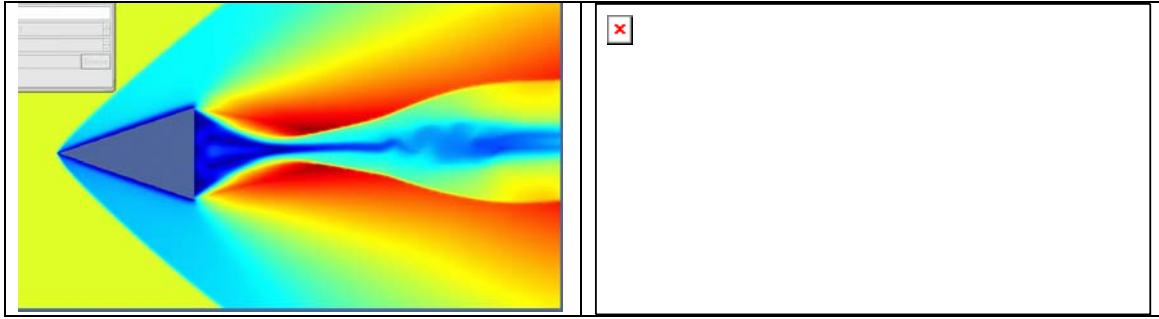
Figure 58. Mach number (0.009<M<5) on the left, gas temperature (0.4<T<4.14) on the right.

A subsonic flow around a cylinder has been studied for different regimes using the Boltzmann (BGK) solver. It is known from experiments and theoretical investigations that for 0<Re<4 the flow is symmetrical. In Figure 59 the velocity field for a steady regime at M=0.55, Kn=0.2 (Re=2.75) is depicted.
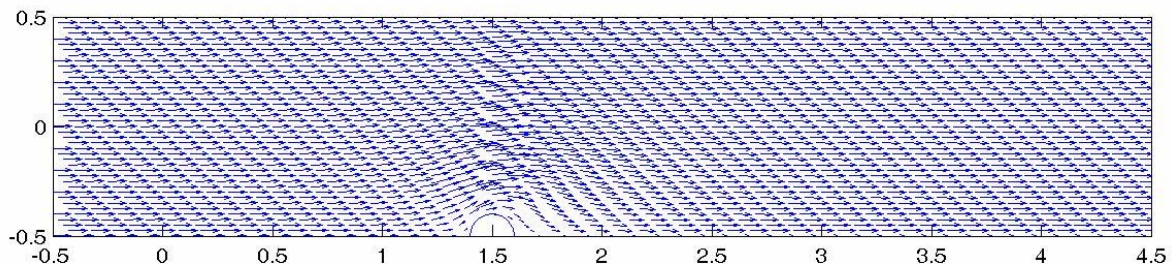
Figure 59. Velocity field for a subsonic flow at the Reynolds number Re=2.75

For Reynolds numbers in the range 0<Re<40 one can expect attached vortices behind a cylinder. In Figure 60 this flow structure is shown for M=0.55, Kn=0.015 (Re=37).
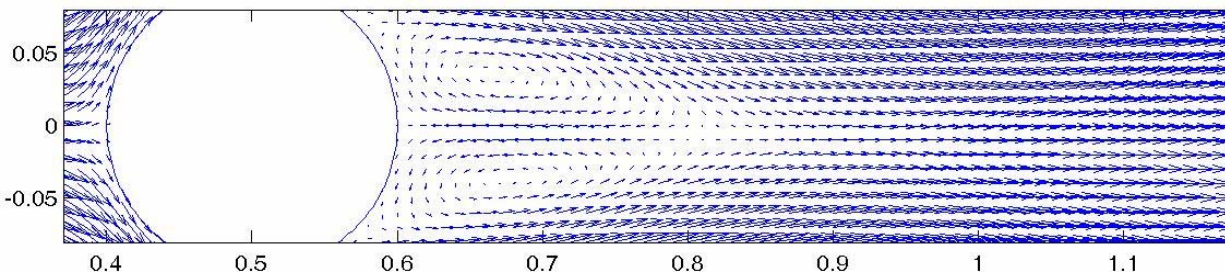
Figure 60. A steady regime with a pair of attached vortices obtained with the Boltzmann (BGK) solver.

For Reynolds numbers in the range 40<Re<60-100 one can expect the appearance of the von Karman vortex street. Figure 61 shows the results of the simulation for M=0.6 and Kn=0.015 (Re=40). The von Karman vortex street is formed during the simulations without external flow perturbations, in distinction with the results of [64]. Figure 62 shows the axial U-velocity vs time at different monitor points.

8572/F
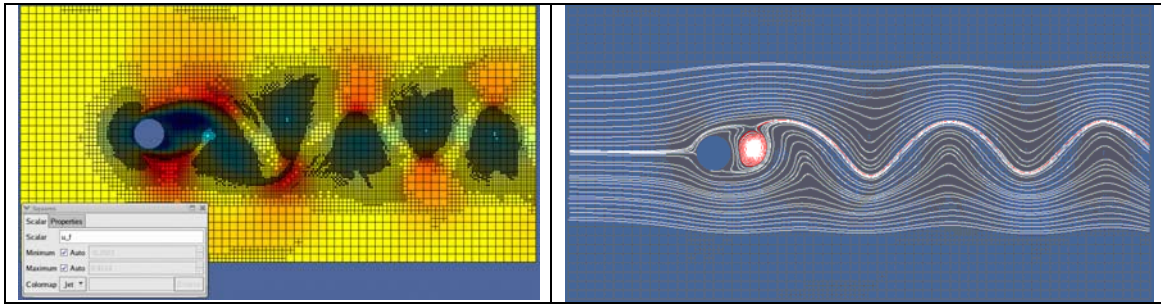
Figure 61. The longitudinal velocity U and computational grid (on the left), and stream lines (on the right).
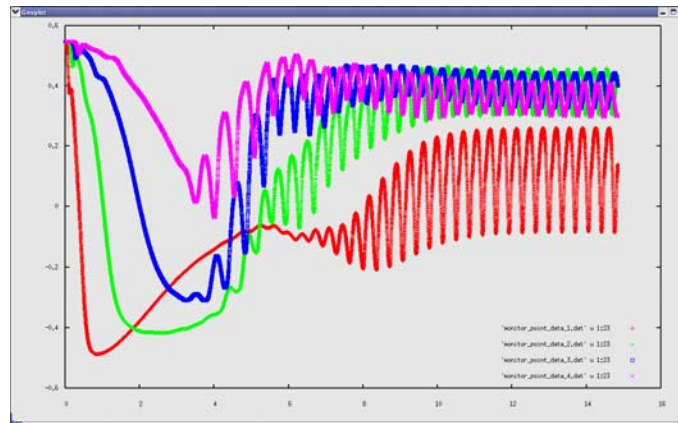
Figure 62. The longitudinal flow velocity vs time at different spatial points. Cylinder of radius R=0.1 is located at x=0, y=0, the monitor points are at y=0 and x=0.2, 0.4, 0.6, 0.8 and 1.0

5. EXTENSION TO MOLECULAR GASES AND REACTIVE GAS MIXTURES

In this section we describe UFS extensions for mixtures of atomic ans molecular gases

5.1. Mixtures of atomic gases

We first implemented the BGK-type collision integral described in [65]. This model is based on the following set of equations

$$\frac{\partial f_i}{\partial t} + \xi \cdot \nabla_x f_i = \nu_i (F_m^i - f_i) \tag{37}$$

where

$$F_m^i = n^{(i)} \left(\frac{m_i}{2\pi k_B T_i} \right)^{3/2} \exp\left(-\frac{m_i |\xi - v_i|^2}{2 k_B T_i} \right)$$

is a Maxwellian distribution. The parameters of this distribution are defined by conservation of total momentum and energy of the mixture (see Ref. 65 for notations):

$$m_i \nu_i v_i = m_i \nu_i v^{(i)} + \sum_{k=1}^{n} 2 \mu_{ik} \chi_{ik} n^{(k)} \left[v^{(k)} - v^{(i)} \right] \tag{38}$$

$$\nu_i \varepsilon_i = \nu_i \varepsilon^{(i)} - \frac{m_i \nu_i}{2} \left| v_i - v^{(i)} \right|^2 + \sum_{k=1}^{n} 2 \mu_{ik} \chi_{ik} n^{(k)} \frac{2}{m_i + m_k}$$

$$\times \left(\varepsilon^{(k)} - \varepsilon^{(i)} + m_k \frac{|v^{(k)} - v^{(i)}|^2}{2} \right) \tag{39}$$

The frequencies are defined as $\nu_\alpha = \sum n_\beta \chi_{\alpha\beta}$, and the quantities $\chi_{\alpha\beta} = 8/6\sqrt{2\pi}\sigma_{\alpha\beta}^2 (kT_\alpha/m_\alpha + kT_\beta/m_\beta)^{1/2}$ are derived in [66].

5.1.1. Temporal relaxation in a binary mixture of rare gases with disparate mass

Initial conditions correspond to two Maxwellian distributions with equal number densities $n_\alpha = n_\beta = 0.5$, temperatures $T_\alpha = T_\beta = 1$, and mean velocities $v_\alpha = -v_\beta = 0.1$. The conservation of momentum implies that the final equilibrium velocity is given by:

$$v = v_\alpha \frac{n_\alpha m_\alpha - n_\beta m_\beta}{n_\alpha m_\alpha + n_\beta m_\beta} \tag{40}$$

It is expected that the approach to equilibrium occur in two stages. During the first stage (Maxwellization), the velocity and heat conduction relax with a characteristic scale

$$\nu \approx \frac{\nu_\alpha \nu_\beta n}{n_\alpha \nu_\beta + n_\beta \nu_\alpha} \tag{41}$$

During the second stage, the temperatures of the species equilibrate with a characteristic scale $v_T = v m_\beta / m_\alpha > v$. This stage can be described by a two-temperature hydrodynamics.

Dimensionless units are used in simulations. The particle velocity is measured in units of thermal velocity of the first (light) species, $v_{th} = \left(2kT / M_1\right)^{1/2}$. The Knudsen number for a gas mixture is defined as

$$Kn = Kn_0 \left\{ n_1 d_1^2 + n_2 d_{12}^2 \sqrt{1 + m_1 / m}_2 / 2 + ... \right\} \tag{42}$$

where $d_{ij} = (d_i + d_j)^2 / 4$ and $Kn_0 = \lambda_1 / L$. We use common momentum space so that components with different mass have different velocity range.

Figure 63, Figure 64 and Figure 65 compare the mean particle velocity, heat flux and temperature of species for HS and BGK models in HeNe and HeXe mixtures.
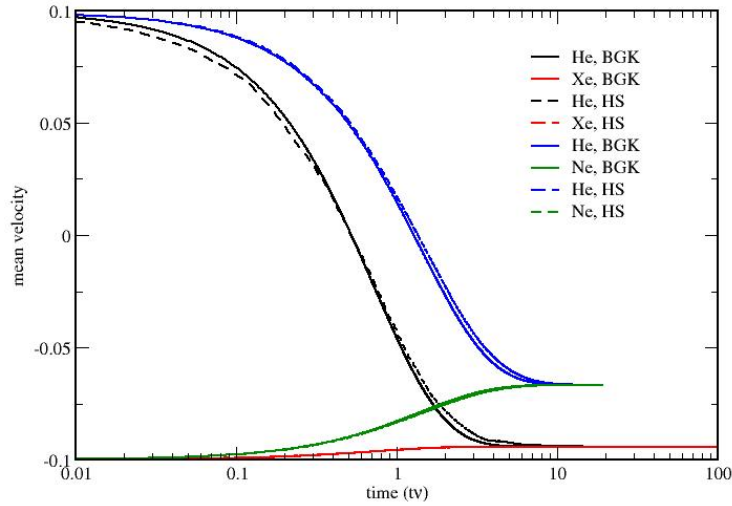
Figure 63. Time dependence of the mean velocity for HeNe and HeXe mixtures.
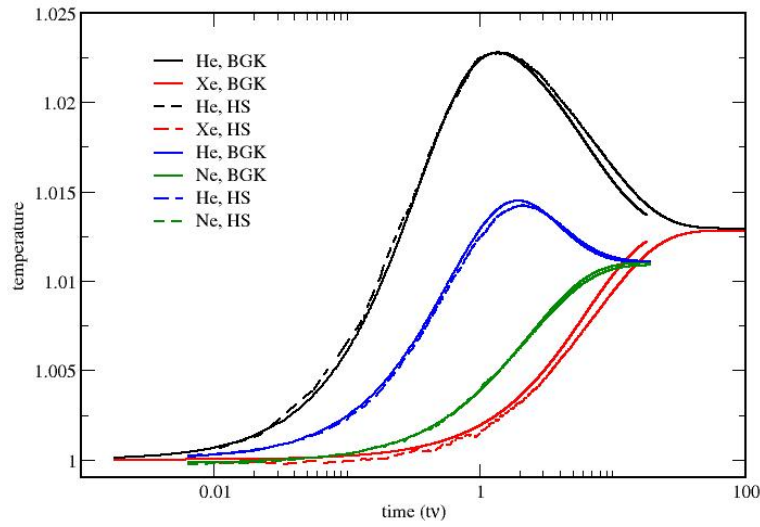
Figure 64. Time dependence of species temperature for HeNe and HeXe mixtures.
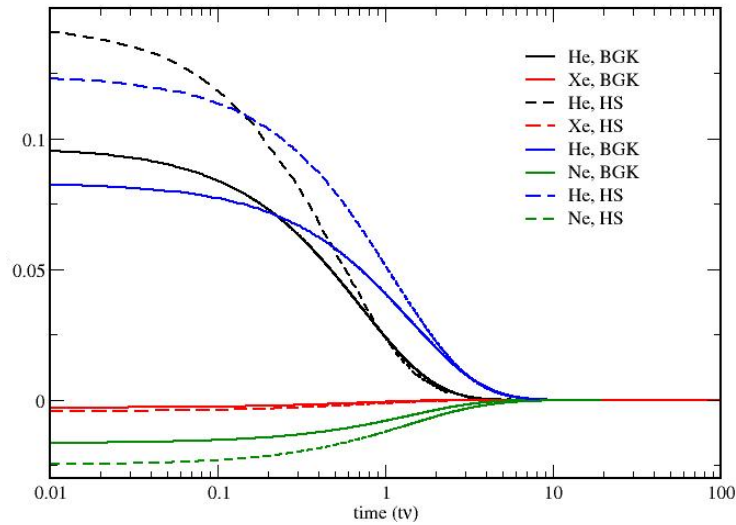
Figure 65. Time dependence of heat fluxes for HeNe and HeXe mixtures.

It is seen from Figure 63, Figure 64 and Figure 65 that relaxation processes in gas mixtures with disparate mass occur in two stages with vastly different time scales. The first (short) stage corresponds to Maxwellization of the distribution function. The heat flux vanishes at the end of this stage. The second (long) stage corresponds to relaxation of temperatures to a common equilibrium value. This stage can be described by a two-temperature hydrodynamic model.

53

5.1.2. Spatial Relaxation for a Gas Mixture

The nonuniform spatial relaxation problem [67] is an analog of the temporal relaxation problem and describes the relaxation processes in space. At the boundary of a half-infinite region (x=0) the nonequilibrium distribution function is specified. The nonequilibrium distribution is relaxed to equilibrium downstream at x>0. The Mach number is assumed to be sufficiently large thus the negative flux of the back-scattered molecules can be neglected. The interesting properties of the spatial behaviour of macroparameters have been observed such as anomalous heat transfer. For mixtures of gases the nonequilibrium structure can be rather complicated. This problem can serve a basic model for the description of kinetic processes in open systems.

We first considered a binary mixture of simple gases. The anomalous heat transfer noted above for a monatomic gas is also observed in a binary gas mixture. Namely, the gradient of the total temperature can have the same sign as the total heat flux. This peculiarity of the nonequilibrium heat convection denotes that the nonequilibrium boundary distribution can heat up (or cool down) the region downstream, so the temperature can increase (decrease) if the heat flux is positive (negative) respectively. Figure 66 shows the spatial distribution of the total temperature and the heat flux. The spatial distance is given in units of the mean free path. The BGK-type model is used. Solutions of the Boltzmann equation for hard sphere molecular model (HS) demonstrate a similar behaviour (the relaxation region is larger than that for the BGK model). In our simulations, the boundary densities, masses and diameters of the gas components are equal to the ratios for oxygen and nitrogen in air. The densities are 1 and 3.71, the masses are 1.14 and 1 and the diameters 1 and 1.07, respectively (here molecules of oxygen and nitrogen is considered as simple and unstructured). The boundary conditions for each component correspond to different Maxwellian distributions. It is interesting that for the 1-st component the temperature decreases monotonically downstream and the heat flux in negative (an absolute value of the heat flux tends to zero downstream), for the 2nd component the temperature increases downstream and the heat flux is positive. It is important that the total temperature gradient and the heat flux have the same signs, namely, this gradient and the flux are both negative.
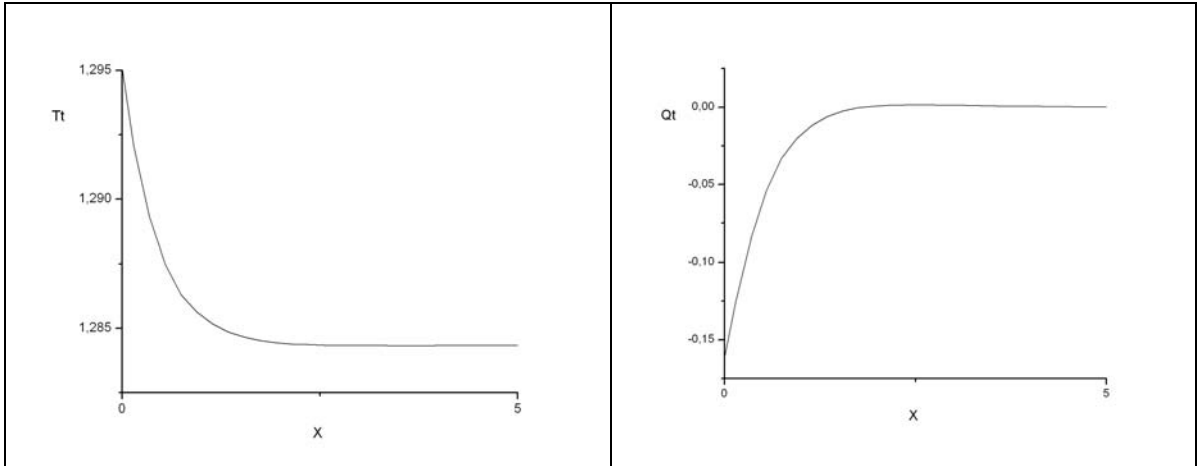
Figure 66. Spatial distribution of the total temperature (on the left) and the total heat flux (on the right) for the nonuniform relaxation problem in a binary gas mixture

The structure of the ralaxation zone for a multiple gas mixture can be more complex; in particular, one can change the spatial distributions of density by changing the boundary conditions for the gas components. Figure 67 shows the spatial distributions of the species density and the total density for a mixture of 3 gases. For a one-component gas, the density can only decrease, but for a mixture, the total density increases with distance (see Figure 67).

This spatial relaxation problem in gas mixtures has also been studied for an unsteady case and for a 2D steady setting.
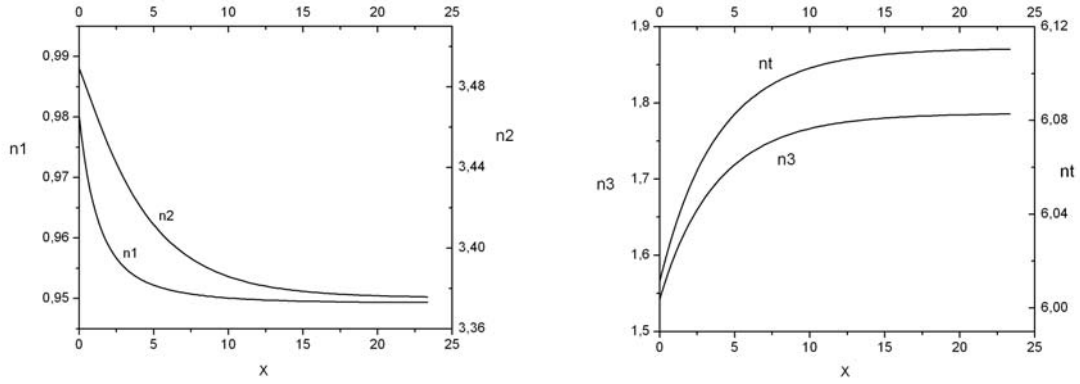
Figure 67. Spatial distribution of specie densities for a nonuniform relaxation problem in a 3-component mixture

5.1.3. Gas acceleration by optical forces

Laser induced optical lattices have recently attracted considerable interest for several applications including contact-free diagnostics [68]. The direct Boltzmann solver has advantages over statistical methods for the analysis of low amplitude density perturbations induced by laser fields We have solved a set of kinetic equations in the form

$$\left(v - \frac{\omega}{k}\right)\frac{\partial f_\alpha}{\partial x} + F_\alpha(x)\frac{\partial f_\alpha}{\partial v} = J_\alpha \tag{43}$$

where $F(x) = F_0 \sin(2\pi x / L)$. Computational domain is from 0 to L, and cyclic boundary conditions are set up at $x=0$ and $x=L$. We have studied the BGK and HS models of inter-molecular interactions.

Figure 68 and Figure 69 show the density modulation of different species in HeNe mixture induced by optical lattices. The observed resonance corresponds to sound wave propagation in the binary mixture with the sound speed determined by gas composition. The heavy and light components respond differently to laser forces. Figure 68 (right part) illustrates the effect of gas composition on density perturbations, reflecting the change in sound speed in gas mixtures of different composition.. Figure 69 shows the effect of Kn number on the density perturbations

HeNe: 0.5:0.5, Kn=0.01 | HeNe: BGK, Kn=0.01
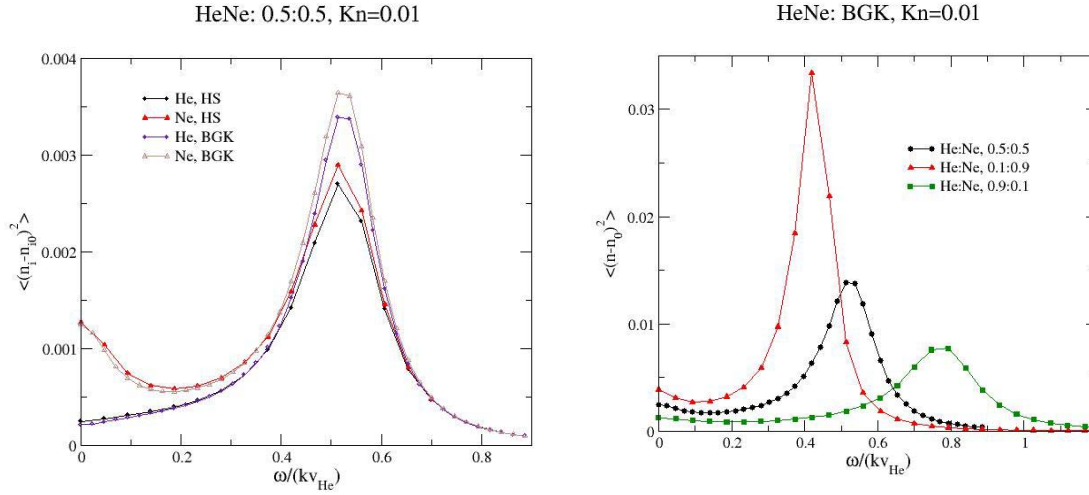
Figure 68. Density modulation of different species: comparison of BGK and HS models (left). Total density according to BGK model for different fraction of species (right).

HeNe, 0.5:0.5, BGK
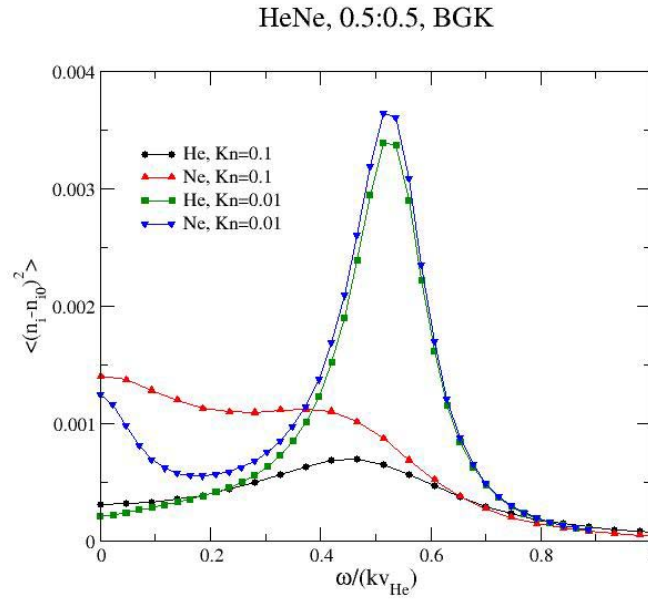
Figure 69. Density modulation of different species for two Kn numbers via BGK model

These results illustrate the potential of UFS for simulations of kinetic effects induced by optical forces in gas mixtures.

5.1.4. Shock wave structure in binary gas mixture

Figure 70 shows results of simulations of the shock wave structure for $M = 3$, the mass ratio $m2/m1 = 3$, and density ratio $n2/n1=0.1$. The boundary conditions are taken from Ref. [69]. The velocity mesh used in these simulations had 32*32*16 nodes.

8572/F

Shock Tube: MultiSpecies BGK, m2/m1=3, Species 1

Shock Tube: MultiSpecies BGK, m2/m1=3, Species 2
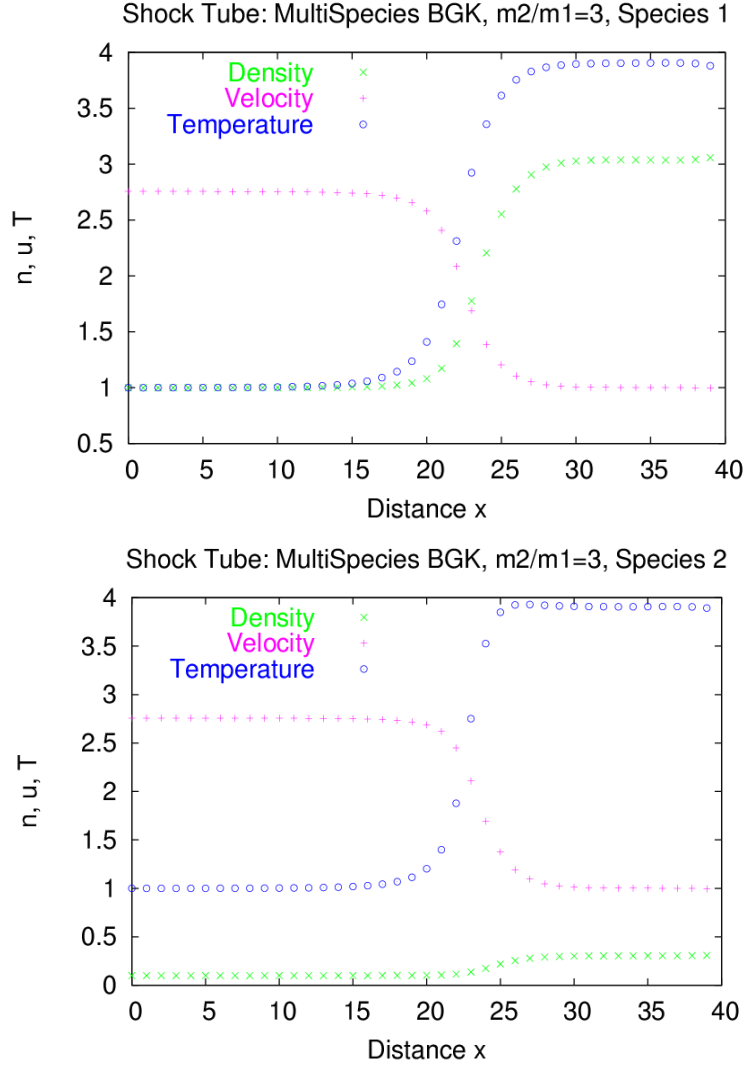
Figure 70 Shock structure for a two-component gas mixture with a mass ratio of 3.

Two types of velocity meshes have been tested, the one with same velocity mesh for different components, and the other with different velocity mesh (cell numbers and velocity range) for components with different mass. The second type of mesh turned out to be preferable since it allowed us to capture the key behavior of the distribution function with smaller number of mesh points. Criteria for selection of optimal mesh in velocity space were analyzed.

Furthermore, the collision integral based on HS model for multi-component mixtures [70] was implemented using momentum space rather than velocity space. We have carried out calculations for the shock wave structure in a mixture of two gases with mass ratio ¼, the upstream density of heavy component 0.9 and M=2. The HS model is used with equal molecular diameters. Figure 71 shows the velocity distribution functions (averaged over *y*- and *z*-directions) of both species on the common momentum space and at different locations in the shock wave. Figure 72 shows the distribution of normalized densities $[(n_i(x) - n_{i-})/(n_{i+} - n_{i-})]$ and parallel and perpendicular temperatures of both gas species. The results are in close agreement with [70] One can see that the parameters of the heavy component react to shock wave with a delay compared to those of the light component. The temperature of the heavy component "overshoots," which is also a well known phenomenon [70]. We also note that with increasing the mass ratio, the computational time increases greatly. Using different

57

velocity mesh for different components and simplifying collision integral for the mixtures with disparate mass [71] should increase the efficiency of simulations.
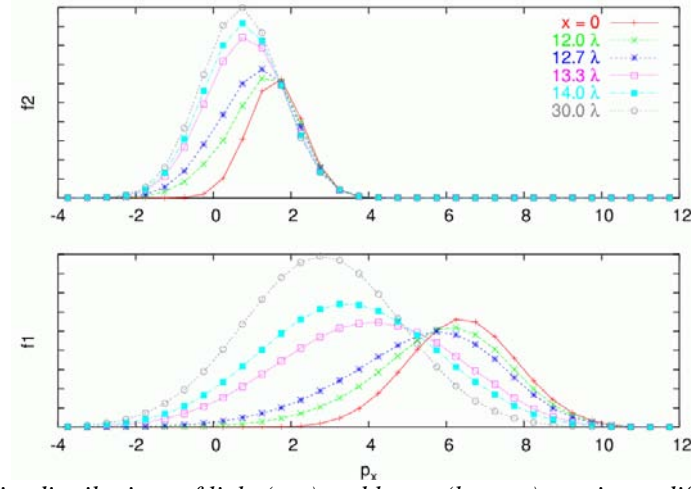
Figure 71 Velocity distributions of light (top) and heavy (bottom) species at different points of the shock wave for M=2 and mass ratio ¼. The species momentum space p_x is used as x-axis.
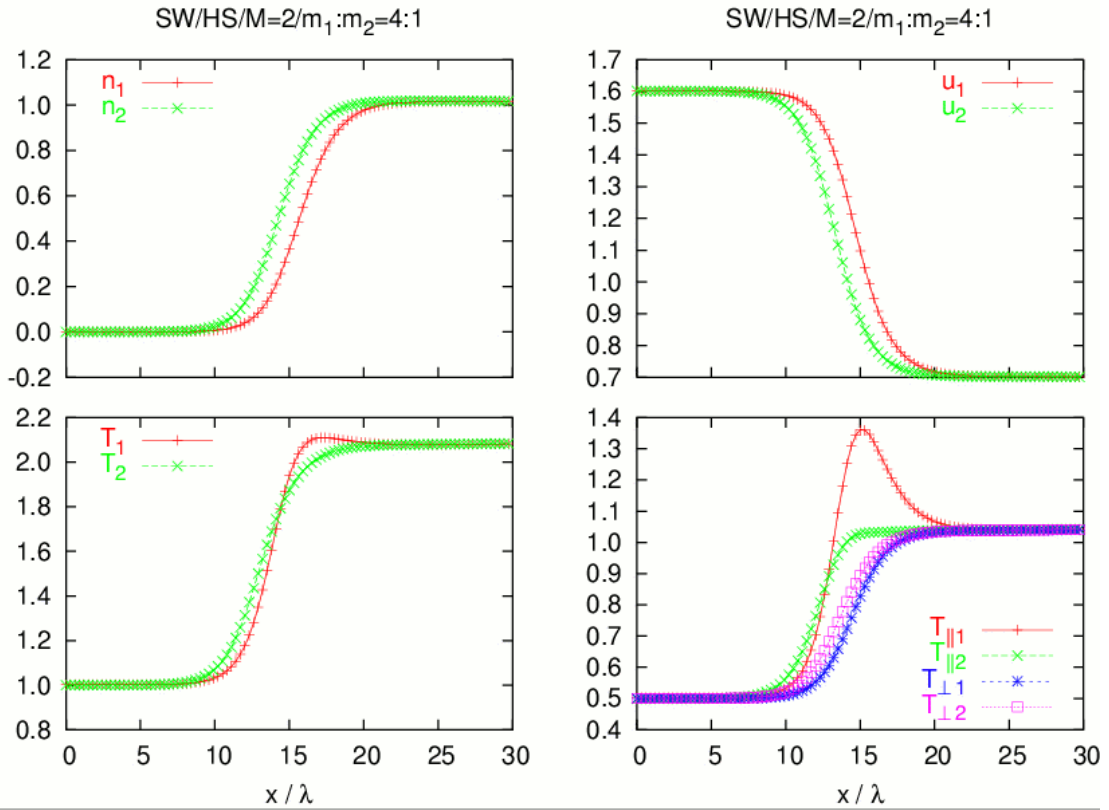
Figure 72 Profiles of normalized density, velocity, temperature and parallel and perpendicular temperatures for the shock wave in a binary gas mixture for M=2 and $m_1/m_2 = ¼$.

Figure 73 shows the results of simulations using the multi-species BGK Boltzmann solver for multi-component gas flow around a cylinder at Mach = 3 and Kn = 0.001 with 3 species of the following masses: $m_1 = 1$, $m_2 = 1.5$ and $m_3 = 2$. The collision diameters d_1, d_2 and d_3 assumed to be the same and equal to 1.
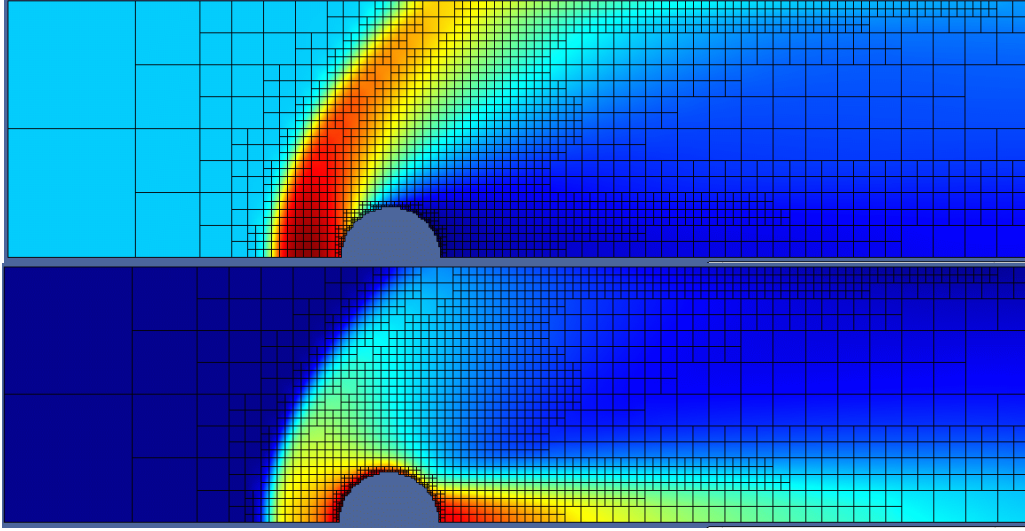
Figure 73 Multi-species BGK Boltzmann solver: spatial distributions of total gas density (top, 0.24<rho<8.97) and temperature (bottom, 1<T<5.3) for M = 3, Kn = 0.001, 3 species of masses: m_1 = 1, m_2 = 1.5 and m_3 = 2, with equal collision diameters.

5.1.5.   Multi-species Euler solver

The multi-species continuum solver has been implemented in UFS. The code enables user to automatically create any number of variables for solving continuum equations for each species and specify initial conditions, boundary conditions at the boundaries of computational domain and at solid body surfaces. The implementation is based on the multi-species BGK operator with an assumption of instantaneous equilibration of all mixture components.

Figure 74 shows results of simulations using the multi-species kinetic Euler solver for a flow around a cylinder at M = 3, with 3 species of the masses: $m_1 = 1$, $m_2 = 1.5$ and $m_3 = 2$, with equal collision diameters d_1, d_2 and d_3 =1.
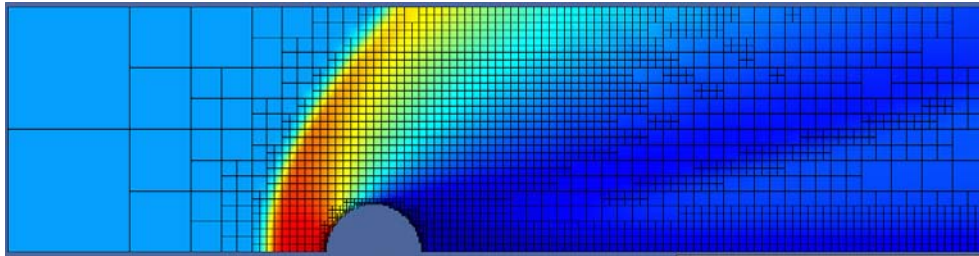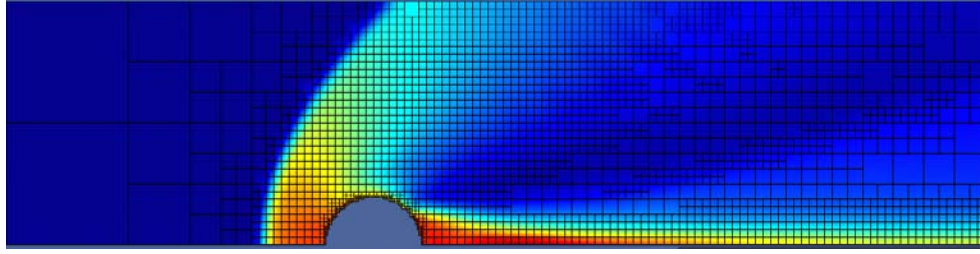
Figure 74 Multi-species kinetic Euler solver: Spatial distributions of total gas density (top, 0.22<rho<10.5) and temperature (bottom, 1<T<4.79) for M = 3, Kn = 0.001, 3 species of masses: $m_1 = 1$, $m_2 = 1.5$ and $m_3 = 2$, with equal collision diameters.

The coupling algorithm between the multi-species Euler and Boltzmann solvers has been developed for arbitrary gas mixtures.

5.2.   Rotationally Excited Molecules

5.2.1.   Wang-Chang-Uhlenbeck (WCU) solver

We have developed a Wang-Chang-Uhlenbeck (WCU) solver for molecular gases with rotational degrees of freedom following [72]. The WCU solver was tested for the shock wave (SW) structure in Nitrogen for a wide range of Mach numbers and compared with experimental cases of Alsmeyer (for M= 1.53, 1.7, 2, 2.4, 3.2, 3.8, 6.1, 8.4, 10) and Robben and Talbot experiment [73] for M=7.

Figure 75 compares experimental data by Alsmeyer with simulation results for M=1.53 and M=1.7. The computations were performed using 30 rotational levels for the first case and 32 levels for the second case. The number of levels was selected based on the temperature range of the considered problem. For small deviations from the room temperature, using 24 levels for Nitrogen was found to be sufficient. The typical CPU time was about 35 hours in both cases on a AMD64 3000 processor.
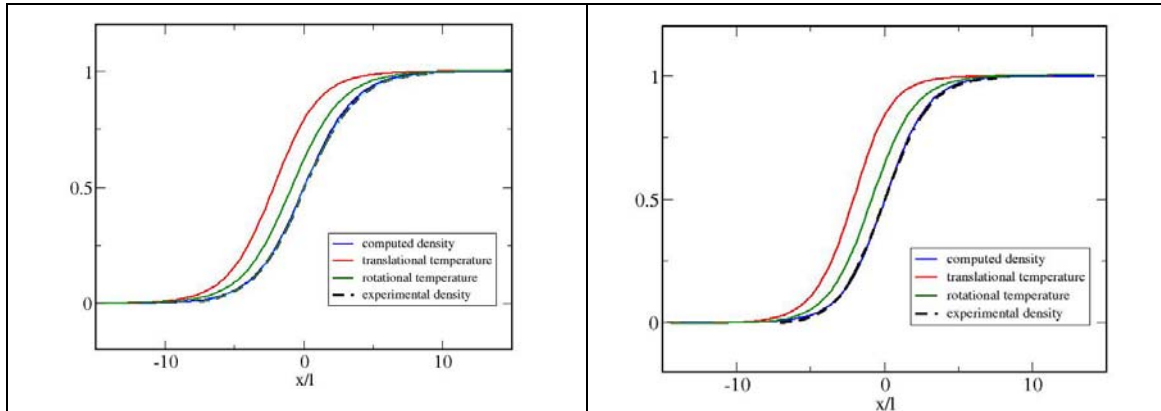
Figure 75 Shock wave structure in Nitrogen for M=1.53 (left) and M=1.7 (right)

Figure 76 shows rotational spectrum for 44 levels at several points of the wave front: $x = -\infty$, $x = x_c - 2\lambda$, $x = x_c - \lambda$, $x = x_c$, $x = x_c + \lambda$, $x = \infty$. Here x_c denotes the SW center defined as the point where the reduced gas density is equal to ½. On the x-axes is the number of the rotational level, on the y-axes is the population of the nth rotational level. It is seen that some peculiarity of the spectrum around 7-8 levels is observed at the second, third and fourth spatial points.

60
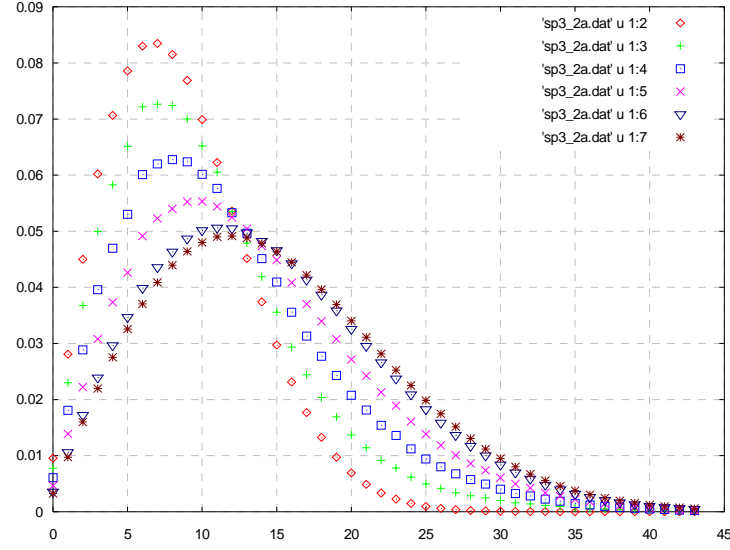
Figure 76 Rotational spectrum at different points of the shock wave at M=3.2.

Figure 77 shows distributions of gas density, translational and rotational temperatures obtained in our simulations for *M*=12.9. Our results are in good agreement with the experimental data by Robben and Talbot and computations of K. Koura by DSMC method [74].
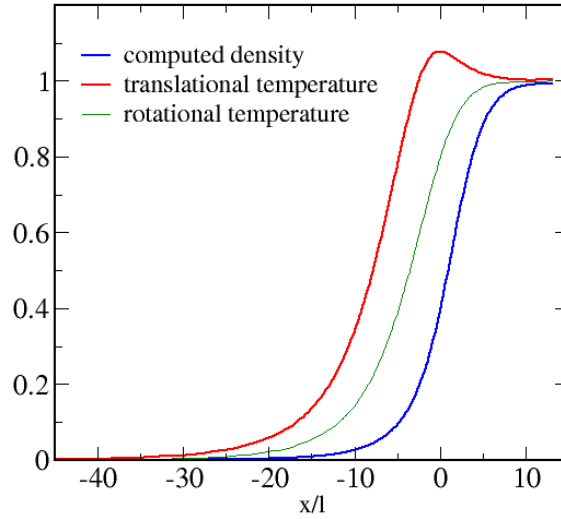
Figure 77 Shock wave structure in Nitrogen at M=12.9.

Figure 78 shows rotational spectrum for 25 levels at several points along the wave front. The center of SW is located at *X*=0. On the *x*-axes is the rotational level number, on the *y*-axes is the population of the rotational levels. It is clearly seen that the rotational equilibrium inside the SW doesn't exists for such a high Mach number.

61
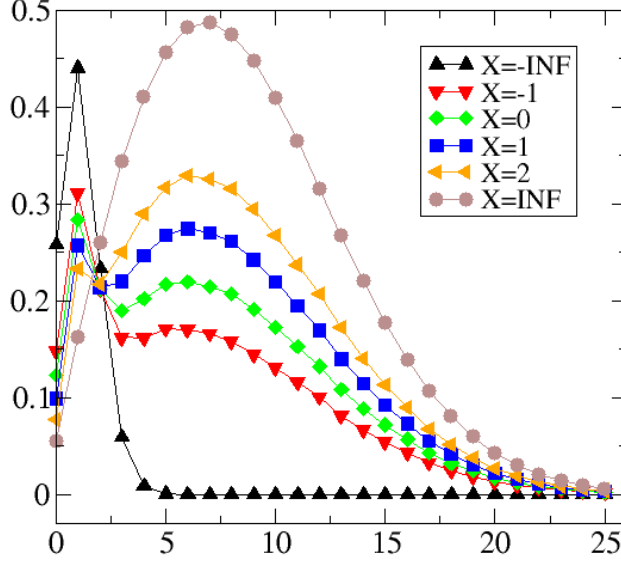
Figure 78 Rotational spectra at different points along the shock wave in Nitrogen at M=12.9.

The WCU model for rotationally excited molecules is rather expensive computationally because a separate kinetic equation is solved for each rotationally excited level of the molecule. For practical applications, we have implemented a simplified Rykov model, which was demonstrated in a number of papers (see [75] for further references)

5.2.2. Rykov Model

Rykov's model (R-model) for molecular gases with rotational degrees of freedom introduces two functions $f_0 = \int f de$ and $f_1 = \int e f de$, where f is the distribution function depending on rotational energy e. Then one obtains two equations

$$\frac{df_0}{dt} = \nu_r \left(f_0^r - f_0 \right) + \nu_t \left(f_0^t - f_0 \right) \tag{44}$$

$$\frac{df_1}{dt} = \nu_r \left(f_1^r - f_1 \right) + \nu_t \left(f_1^t - f_1 \right) \tag{45}$$

The right-hand side of each equation corresponds to a model collision integral. The macroscopic parameters (corresponding to rotational and translational movement of molecules) are obtained by integration of f_0 and f_1 over velocity space (details can be found in [75]). The R-model collision integral has been implemented for 3D and 2D cases (2D case takes into account the symmetry of the velocity space). The conservation of mass, momentum and total energy is enforced by introducing a procedure analogous to conservative correction used in the BGK solver.

The R-model was tested for rotational relaxation in nitrogen. Figure 79 shows the time dependence of the macroparameters during the relaxation of rotationally excited nitrogen molecules.
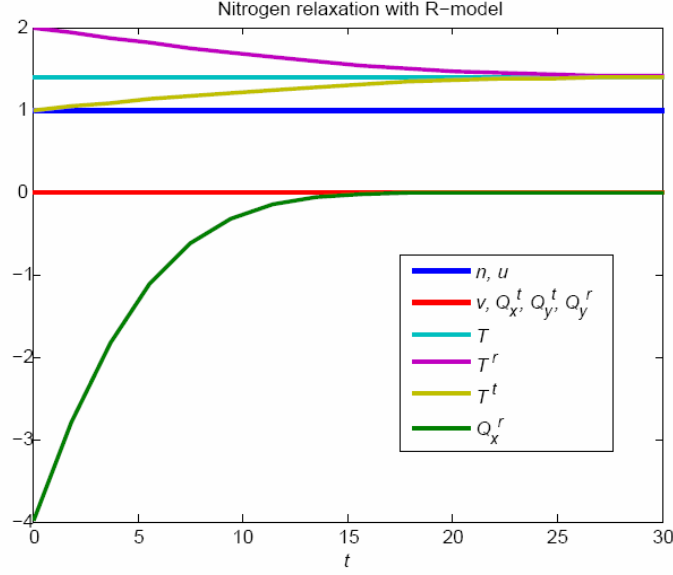
Figure 79. Time dependence of the macroparameters during the relaxation of rotationally excited nitrogen

5.3. Vibrationally Excited Molecules

We have extended the WCU solver for vibrationally excited molecules. The results for vibrational relaxation are shown in Figure 80 for the initial conditions: T_v=0.1 and T_{tr}=1. It is seen that the translational and vibration temperatures relax to the same values with the characteristic relaxation time depending on the V-T cross sections. The total V-T cross section is higher then the partial cross sections because of a number of permitted transitions. The problem is solved for 12 vibration levels, rotational levels are ignored.
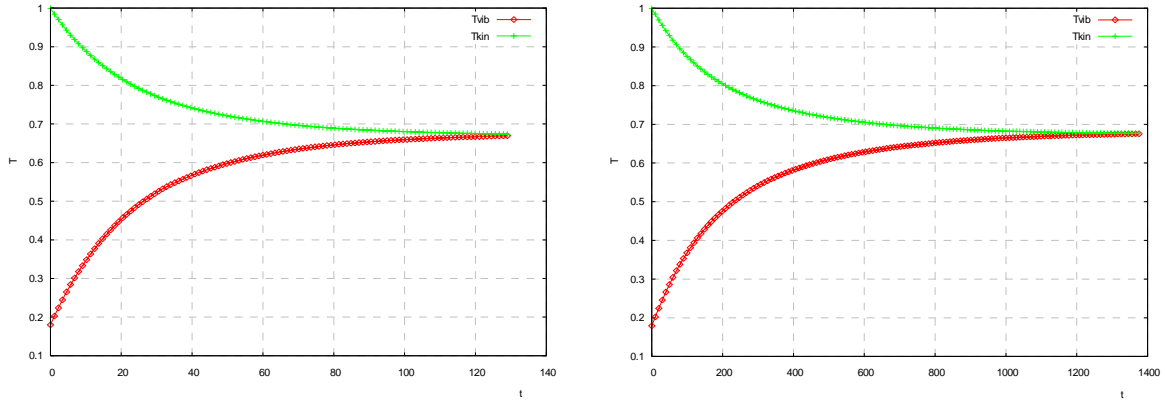
Figure 80 V-T relaxation for $P_{ij}^{kl} = 0.001, (k,l \neq i, j)$ and for $P_{ij}^{kl} = 0.0001, (k,l \neq i, j)$ (right)

5.3.1. Three-temperature BGK model

In order to account for both the rotational and vibrational energies in the Boltzmann solver, we have developed a 3-temperature (or 3T) BGK model. This model is based on the same ideology as the previously implemented Rykov model for the rotational energies.

In the presence of internal degrees of freedom, the kinetic equation can be written in the form:

$$\frac{\partial f}{\partial t} \;+\; \nabla_r \cdot (\xi f) \;=\; I^{el} + I^{in} \tag{46}$$

where I^{el} represents the elastic collision integral and I^{in} denotes the inelastic collision integral. For the treatment of inelastic collisions, we use a simplified relaxation model. The elastic collision integral is written in the BGK form:

$$I^{el} = \nu^{el}(f_m - f), \tag{47}$$

where

$$f_m = f_m^t(n,u,T_t) f_m^r(T_r) f_m^v(T_v) =$$

$$\frac{n}{(\pi T_t)^{3/2}(\pi T_r)^{K_r/2}(\pi T_v)^{K_v/2}} \exp[-(\xi-u)^2/T_t - K_r\xi_r^2/(2T_r) - K_v\xi_v^2/(2T_v)]. \tag{48}$$

Here T_t, T_r, T_v denote the translational, rotational, and vibrational temperatures defined from the relations:

$$nE_t = 1.5nT_t + nu^2 = \int f_m \xi^2 d\xi d\xi d\xi \tag{49}$$

$$nE_r = 0.5nK_r T_r = \int f_m \xi_r^2 d\xi d\xi d\xi \tag{50}$$

$$nE_v = 0.5nK_v T_v = \int f_m \xi_v^2 d\xi d\xi d\xi, \tag{51}$$

Here K_r and $K_v(T) = \dfrac{2\theta}{T\exp(\theta/T-1)}$ are the numbers of rotational and vibrational degrees of freedom (θ denotes the characteristic vibrational temperature).

The inelastic collision integral is presented in the form:

$$I^{in} = \nu^{trv}(f_m^* - f) + \nu^{tr}(f_m^{**} - f), \tag{52}$$

where

$$f_m^* = f_m^t(n,u,T^{eq}) f_m^r(T^{eq}) f_m^v(T^{eq}) =$$

$$\frac{n}{(\pi T^{eq})^{3/2+K_r/2+K_v/2}} \exp[-(\xi-u)^2/T^{eq} - K_r\xi_r^2/(2T^{eq}) - K_v^{eq}\xi_v^2/(2T^{eq})], \tag{53}$$

$$f_m^{**} = f_m^t(n,u,T^{eqr}) f_m^r(T^{eqr}) f_m^v(T_v) =$$

$$\frac{n}{(\pi T^{eqr})^{3/2+K_r/2}(\pi T_v)^{K_v/2}} \exp[-(\xi-u)^2/T^{eqr} - K_r\xi_r^2/(2T^{eqr}) - K_v\xi_v^2/(2T_v)], \tag{54}$$

Here T^{eq} is the equilibrium temperature of translational, vibrational and rotational degrees of freedom, $T^{eq} = \dfrac{3T_t + K_r T_r + K_v T_v}{3 + K_r + K_v^{eq}}$, and T^{eqr} is the equilibrium temperature of rotational and

translational degrees of freedom, $T^{eqr} = \dfrac{3T_t + K_r T_r}{3 + K_r}$.

For the numerical solution, Eq. (46) is reduced to a set of equations for three functions

$$f_0 = \int f d\xi_r d\xi_v, \tag{55}$$

$$f_1 = \int f \xi_r^2 d\xi_r d\xi_v, \tag{56}$$

$$f_2 = \int f \xi_v^2 d\xi_r d\xi_v. \tag{57}$$

Such a reduction is possible because the convection part of the kinetic equation does not contain derivatives with respect to vibrational and rotational energies of the molecules. After integration of Eq. (46) with weights $(1, \xi_r^2, \xi_v^2)$, we obtain:

$$\frac{df_0}{dt} = \nu^{el}(-f_0 + f_m^t(T_t)) + \nu^{trv}(-f_0 + f_m^t(T^{eq})) + \nu^{tr}(-f_0 + f_m^t(T^{eqr})) \tag{58}$$

$$\frac{df_1}{dt} = \nu^{el}(-f_1 + E_r f_m^t(T_t)) + \nu^{trv}(-f_1 + E_r^{eq} f_m^t(T^{eq})) + \nu^{tr}(-f_1 + E_r^{eqr} f_m^t(T^{eqr})) \tag{59}$$

$$\frac{df_2}{dt} = \nu^{el}(-f_2 + E_v f_m^t(T_t)) + \nu^{trv}(-f_2 + E_v^{eq} f_m^t(T^{eq})) + \nu^{tr}(-f_2 + E_v f_m^t(T^{eqr})) \tag{60}$$

The total (elastic and inelastic) collision frequency ν is defined as $\nu = \nu^{el} + \nu^{trv} + \nu^{tr}$. By introducing $\nu^{trv} = \nu / Z_v$, $\nu^{tr} = \nu / Z_r$, we obtain $\nu^{el} = \nu(1 - 1/Z_v - 1/Z_r)$, where Z_r and Z_v define the number of rotational and vibrational collisions per one elastic collision (which can be any functions of macroparameters such as temperature).

The set of 3 equations (58-60) resembles the Landau-Teller model for the relaxation of rotational and vibrational temperatures. In the UFS code, we have implemented two options for defining Z-numbers. One can specify them as constants or use experimental rates (such as the Millikan rates).

We have further implemented and tested this model in the kinetic 3T-Continuum solver. The coupling of the 3T-BGK and 3T-Continuum solvers has been tested and demonstrated for the 1D Shock Wave (SW) and 2D plume problems.

5.3.2. Shock Wave in Nitrogen

The developed 3T-UFS has been benchmarked for 1D SW simulations using the results presented in [76]. In that work, Mach = 5 SW has been simulated for nitrogen gas taking into account the rotational and vibrational energies using the BGK-NS solver and the DSMC solver. The values of Zr = 3 and Zv = 100 were used in that paper and in our simulations. We first carry out simulations using the 3T-Continuum Solver, the results for which are presented in Figure 81. One can see that the 3T-Continuum Solver result give sharp jumps of the macroparameters as the SW location and slow evolution of Trot and Tvib towards equilibrium with Trot reaching equilibrium quicker than Tvib. The results of the 3T-Continuum Solver are close to those of the BGK-NS presented in [76] considering that the Sutherland law for viscosity has been using in that paper with unclear parameters.
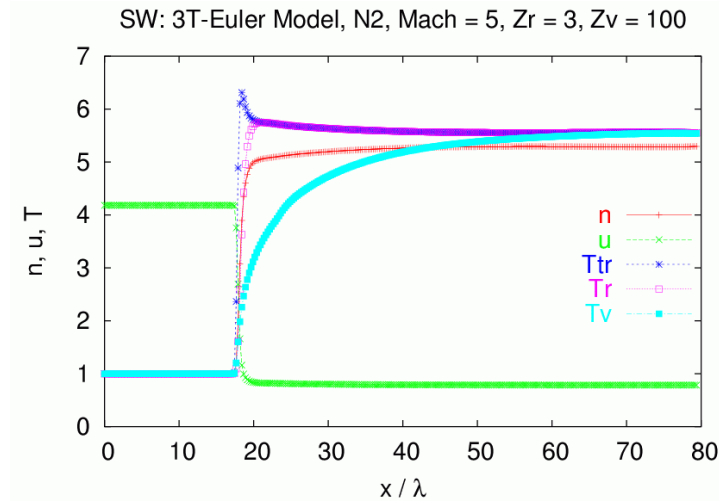
Figure 81. 1D shock-wave profiles of macroparameters obtained using the developed 3T-Continuum solver.

We next carry out simulations for the same conditions using the developed 3T-BGK model in the Boltzmann solver. The results are presented in Fig. 82. One can see that now there is significant spread of SW parameters into the upstream direction in particular of Tvib. This spread of macroparameters is close to that obtained using the DSMC simulations in [76]. Also, the parallel and perpendicular temperatures (their difference demonstrates departure from translational equilibrium) are close to those presented in [76].
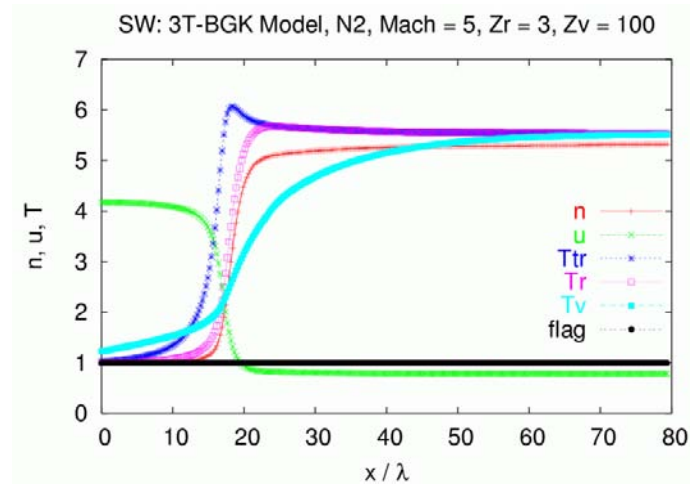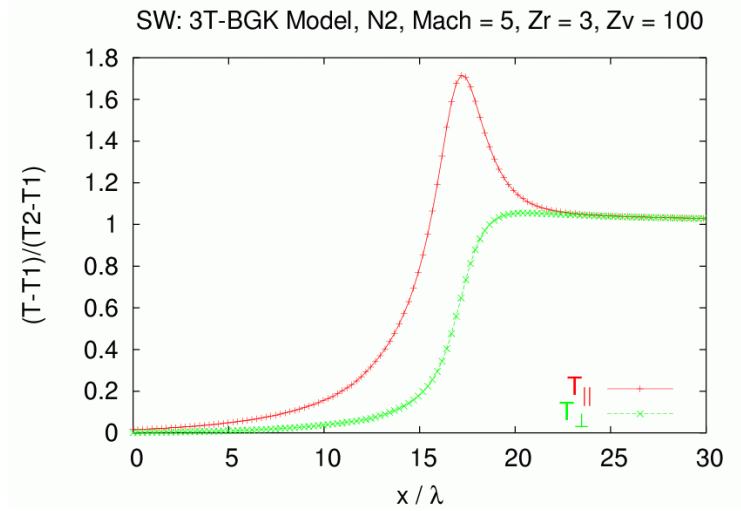
Figure 82. 1D shock-wave profiles of macroparameters and parallel and perpendicular temperatures obtained using the Boltzmann Solver with the 3T-BGK model.

We finally demonstrate the UFS capabilities for this problem by using coupled solution of the 3T-BGK solver with the 3T-Continuum solver. The results are presented in Figure 83. The Boltzmann solver was used only in the upstream region and in the region around the SW (see kinetic flag in Figure 83). The 3T-Continuum Solver was used in the extended downstream region where slow evolution of Tvib takes place. One can see that the results are very close to those obtained using the 3T-BGK Boltzmann Solver with the UFS run requiring almost 4 times less memory and having much faster convergence.
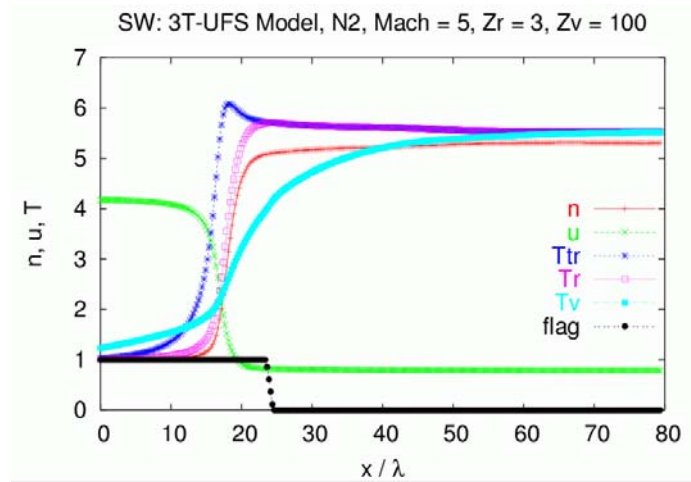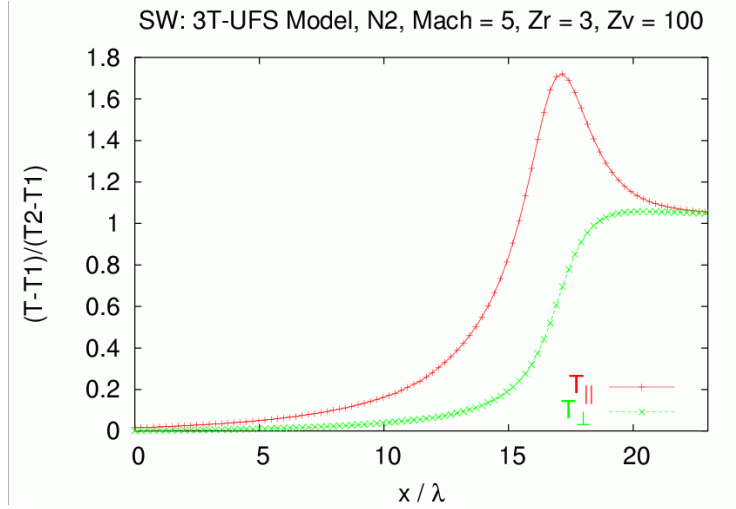
Figure 83. 1D shock-wave profiles of macroparameters, kinetic flag, and parallel and perpendicular temperatures obtained using UFS with coupling of the 3T-BGK and 3T-Continuum solvers.

5.3.3. 3 Temperature Model for a mixture of molecular and atomic gases

When more than one species present in a gas, one needs to take into account momentum and energy exchanges between them. If there are chemical reactions, the model needs to take into account also changes in mass density of each species. The momentum and energy exchanges between molecular and atomic species in a gas are taken into account according to the Morse and Oguchi model described in Ref. [77]. The collisional integral for a mixture of atomic A and molecular A_2 species is written in the following form

$$D_t^{A_2} f_{A_2} = \sum_{B=A,A_2} \nu_{A_2B}^{el} \left(M_{A_2B}^{el} - f_{A_2} \right) + \nu_{A_2B}^{trv} \left(M_{A_2B}^{trv} - f_{A_2} \right) + \nu_{A_2B}^{tr} \left(M_{A_2B}^{tr} - f_{A_2} \right) \tag{61}$$

$$D_t^A f_A = \nu_{AA} \left(M_{AA} - f_A \right) + \nu_{AA_2}^{el} \left(M_{AA_2}^{el} - f_A \right) + \nu_{AA_2}^{trv} \left(M_{AA_2}^{trv} - f_A \right) + \nu_{AA_2}^{tr} \left(M_{AA_2}^{tr} - f_A \right) \tag{62}$$

where the *M*s denote the Maxwellian distribution functions calculated at corresponding equilibrium temperatures and each term represents different type of collisional process.

The validation of the developed 3T-BGK model has been carried out by simulating flow past cylinder for N_2 gas for different Mach and Knudsen numbers. The results presented in Figure 84 and Figure 85 are for Mach = 3 and Kn = 0.05. One can see in Figure 85 that the vibrational temperature starts to grow well behind the shockwave and that the 3 temperatures equalize downstream far from the cylinder.
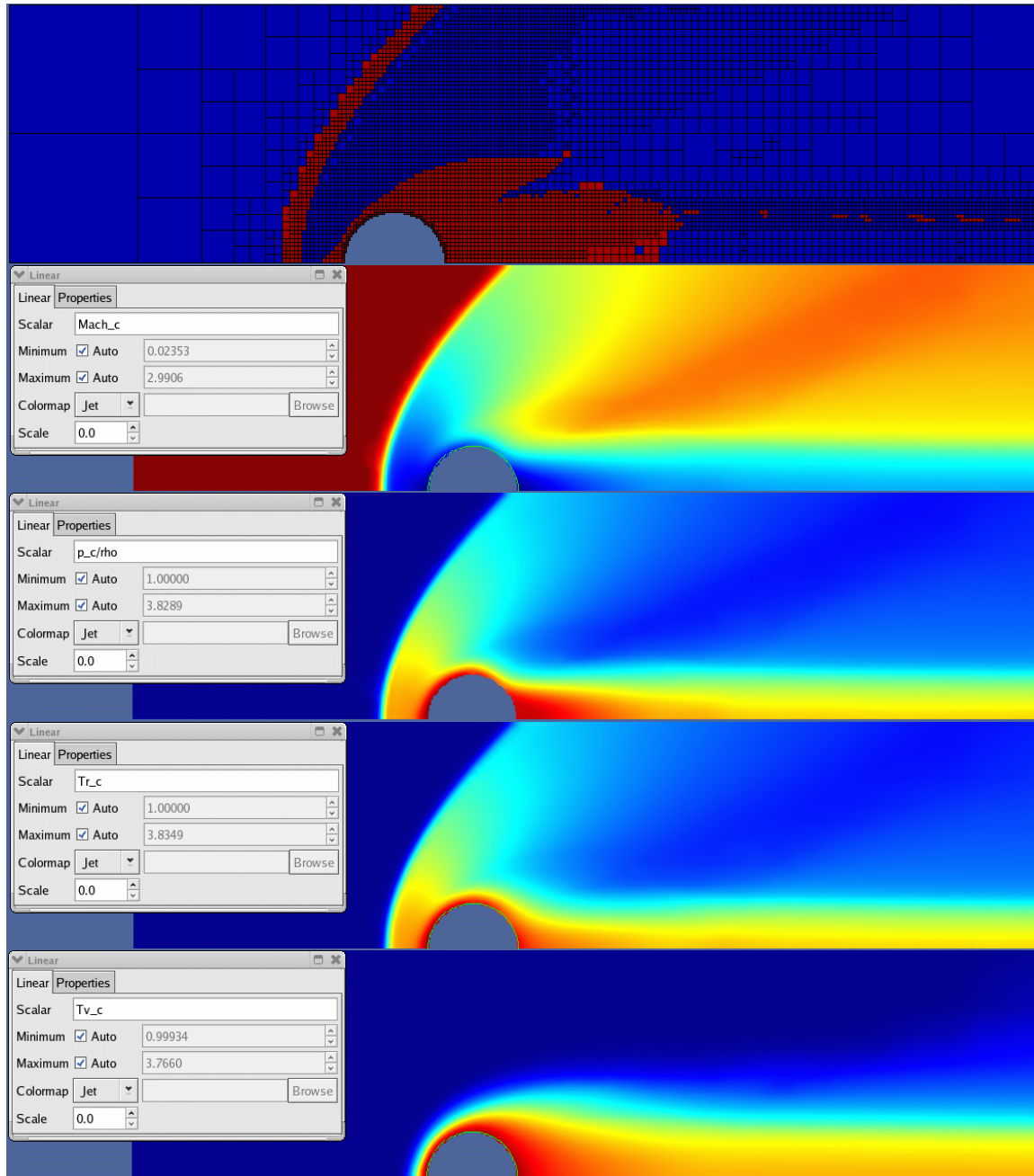
Figure 84. Flow past cylinder, Mach = 3, Kn = 0.05. Shown are the computational mesh and the kinetic flag (in red color), the Mach number profiles and the profiles of translational, rotational and vibrational temperatures.

8572/F
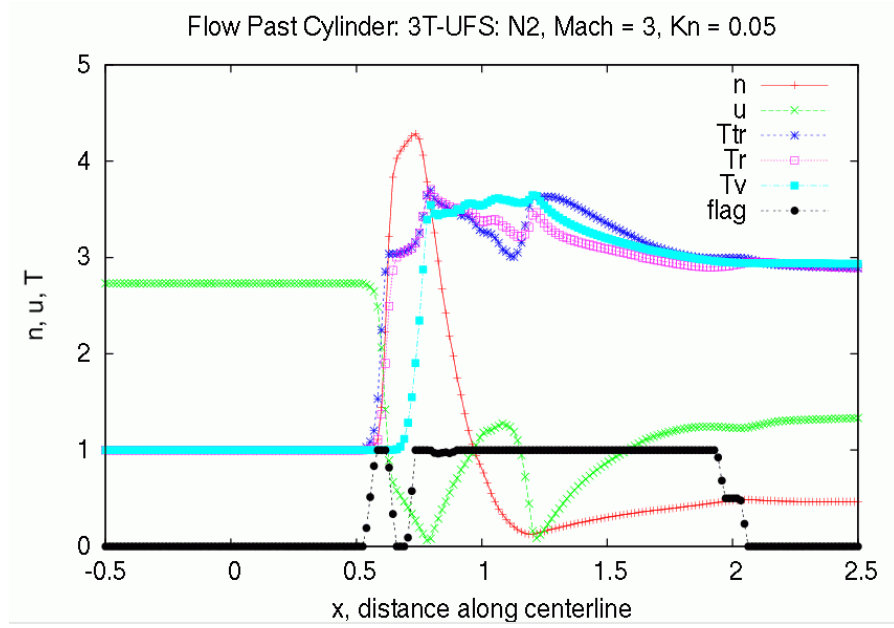
Figure 85. Flow past cylinder for Mach = 3 and Kn = 0.05. Shown are the profiles along the centerline of the kinetic flag, density, velocity, translational, rotational and vibrational temperatures.

The 3T-BGK model has also been tested for the Shock Wave (SW) problem. Figure 86 shows the results for the SW problem at Mach=2 for a mixture of a molecular and an atomic gases.
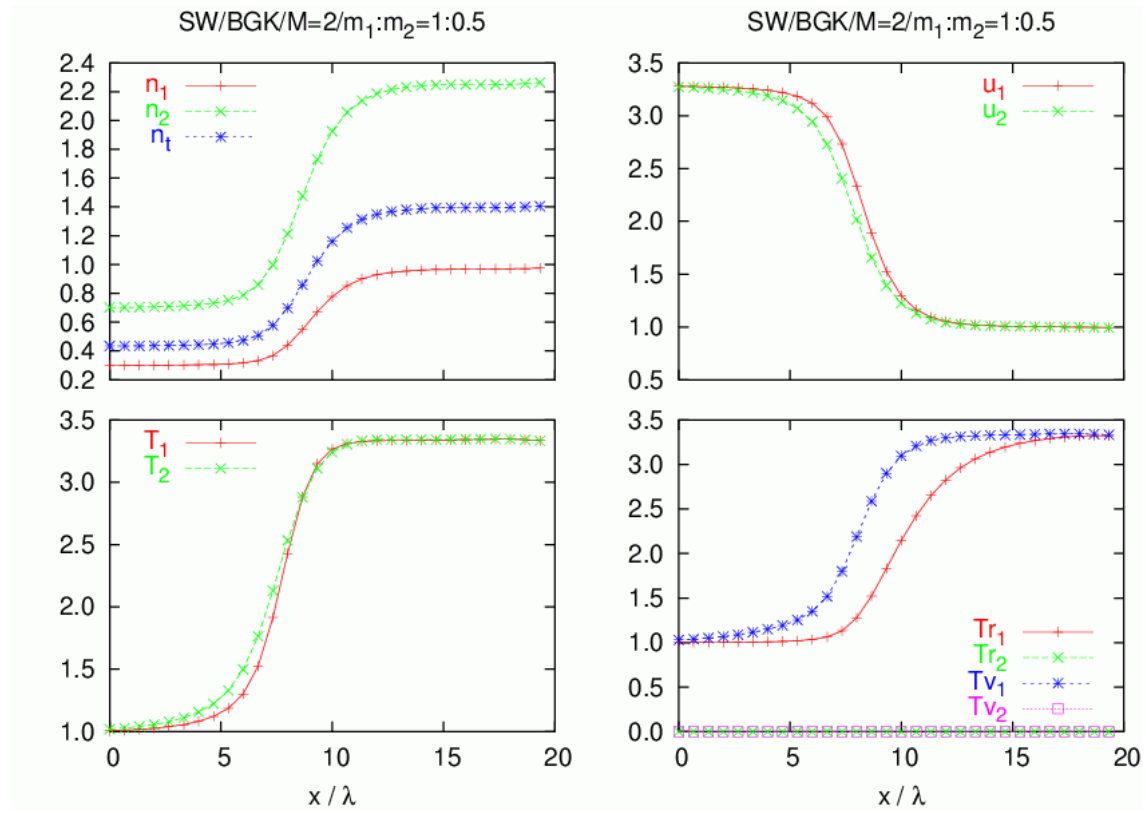
Figure 86. Profiles of density, velocity, translational temperature, rotational and vibrational temperature for the molecule for a 1D SW in a mixture of atomic-molecular gases.

70

5.3.4. Hypersonic Nitrogen flow past a blunt body

The low enthalpy case for a flow past an axisymetric blunt body at Mach=16 has been investigated. The case is described in Ref. [78]. For these conditions, the UFS-3T model was used which takes into account the internal energies of molecules. Model N_2 molecule was used for simulations, which approximates the airflow experimental conditions. The geometry of the body and 2D distrubution of flow parameters is shown in Fig 87. The flow parameters along the streamline are shown in Fig. 88. The shock wave position agrees well with NS simulations presented in Ref. [78]. Also, the pressure distribution obtained using UFS agrees well with the NS results and experimental results from Ref. [78] (see also Figure 89).
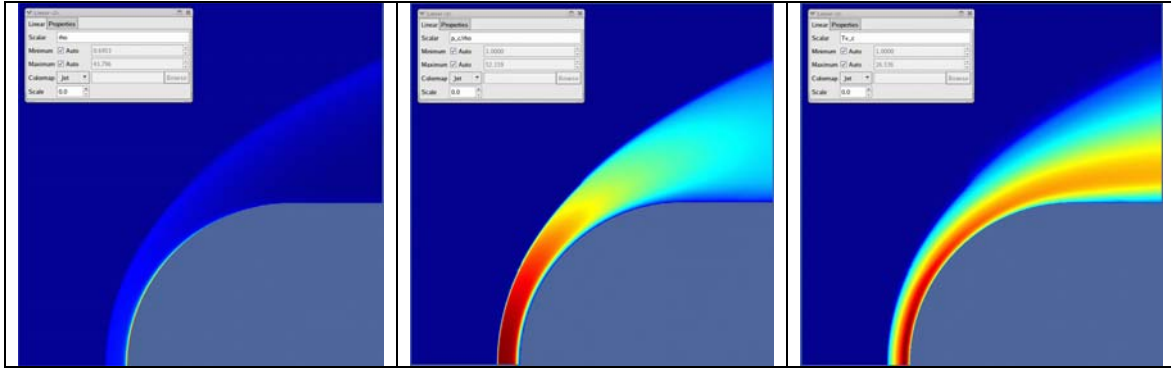
Figure 87. Profiles of macroparameters along stagnation streamline for Mach=16 flow past a blunt body.
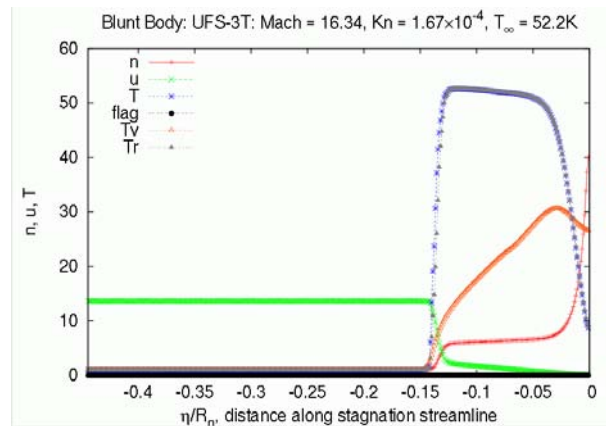
Figure 88. Profiles of macroparameters along stagnation streamline for Mach=16 flow past a blunt body.

71
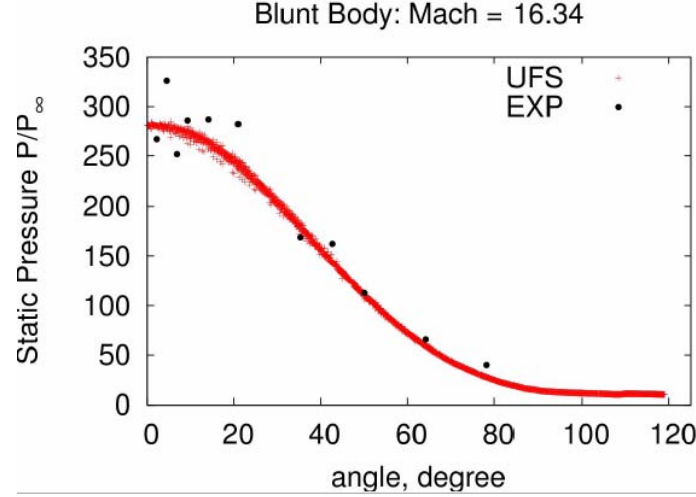
Figure 89. Comparison of static pressure results obtained with UFS and experimental data presented in Ref. [78].

We have also carried out simulations for a plain, 2D geometry. The results in Figure 90 show that the shock wave stands much farther from the cylinder surface compared to the axi-symmetric case.
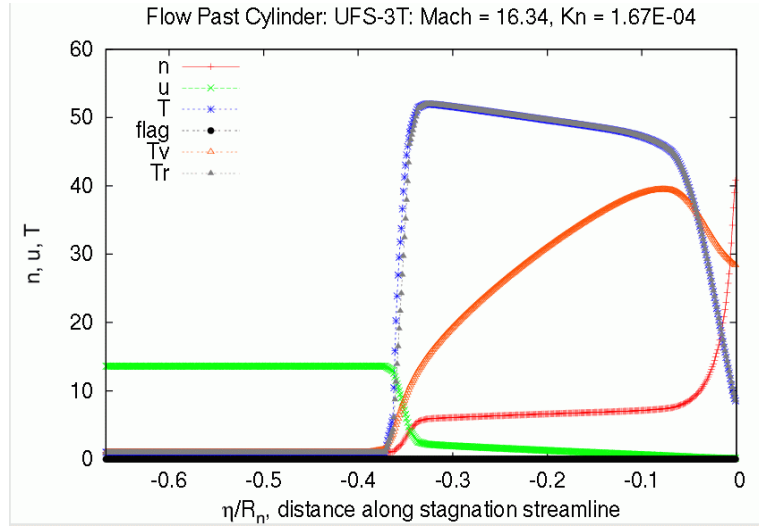
Figure 90. Profiles of macroparameters along stagnation streamline for Mach=16 flow past circular cylinder for a 2D, plain case.

Details regarding UFS evaluation for computing heat flux in hypersonic flows can be found in [79]. It was concluded that using kinetic solvers (Boltzmann solver and CFD gas kinetic schemes) in combination with Cartesian mesh offers notable improvements of the heat flux calculations compared to the traditional NS solvers and comparable to DSMC accuracy. Boltzmann solver gives smooth heat fluxes for spatial grids with cell sizes of the order of local mean free path or larger, provided that spatial grids with gradual stretching are used near the surfaces of the body.

The optimization with respect to the size of the kinetic domain (on a given spatial grid) has also been studied in [79]. It was observed that for a small size of the kinetic domain, unphysical (e.g., non-monotone) profiles can be obtained near the body. For an optimal size of the kinetic domain, reliable heat fluxes are obtained with minimal computational cost. It was also observed that using the kinetic Navier-Stokes solver instead of the kinetic Euler solver allows reducing the size of kinetic domain.

5.4. Chemical Reactions

A chemistry module has been added to the kinetic Euler solver for reacting gas mixtures. In this particular module, 17 reaction steps have been implemented between major air species O, O2, N, N2 and NO. Figure 91 shows results of a relaxation problem with the following set of chemical reactions:

$$O_2 + M \longleftrightarrow 2O + M$$

$$N_2 + M \longleftrightarrow 2N + M \tag{63}$$

$$NO + M \longleftrightarrow N + O + M$$
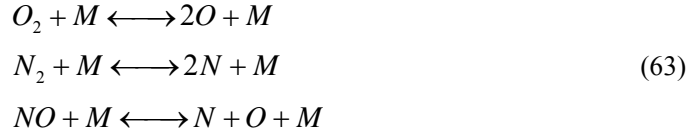
where $M(O_2, O, N_2, N, NO)$. The initial densities ρ_0 of species are (in kg/m^3): $O_2 = 1.E - 3; O = 2.E - 5; N_2 = 2.E - 3, N = 2.E - 4, NO = 2.E - 3$
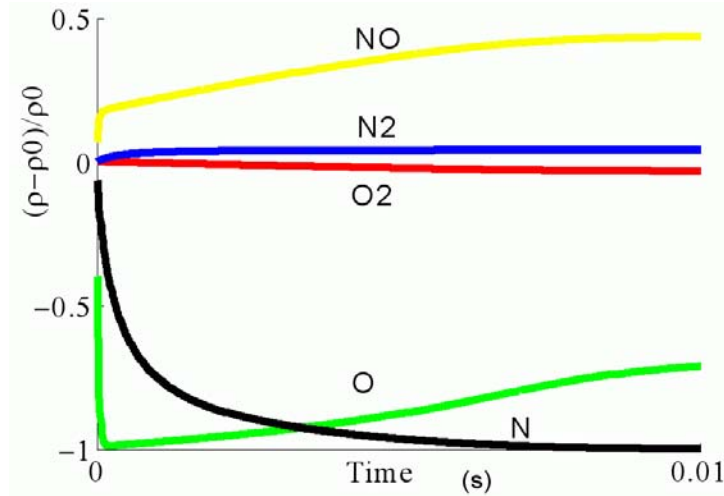
Figure 91 Time evolution of gas species due to chemical reactions.

We have extended the multi-component kinetic Euler solver for reactive gas mixtures following the work [80] taking into account changes in the internal energy. The model assumes that the translational and rotational temperatures are the same and that each molecular species has its own vibrational temperature T_v. Figure 92 shows results of 2D simulations for supersonic air flow around a cylinder at M=2. The incoming gas density is $\rho = 0.1$ kg/m^3. It is known that due to slow V-T relaxation, vibrational temperature lags behind the translational temperature and in our case remains high behind the cylinder. Figure 92 shows distributions of species density, *u*-velocity, translational and vibrational temperature of different molecules along the central streamline. It is seen that the vibrational temperature of different molecules is different at low gas density.
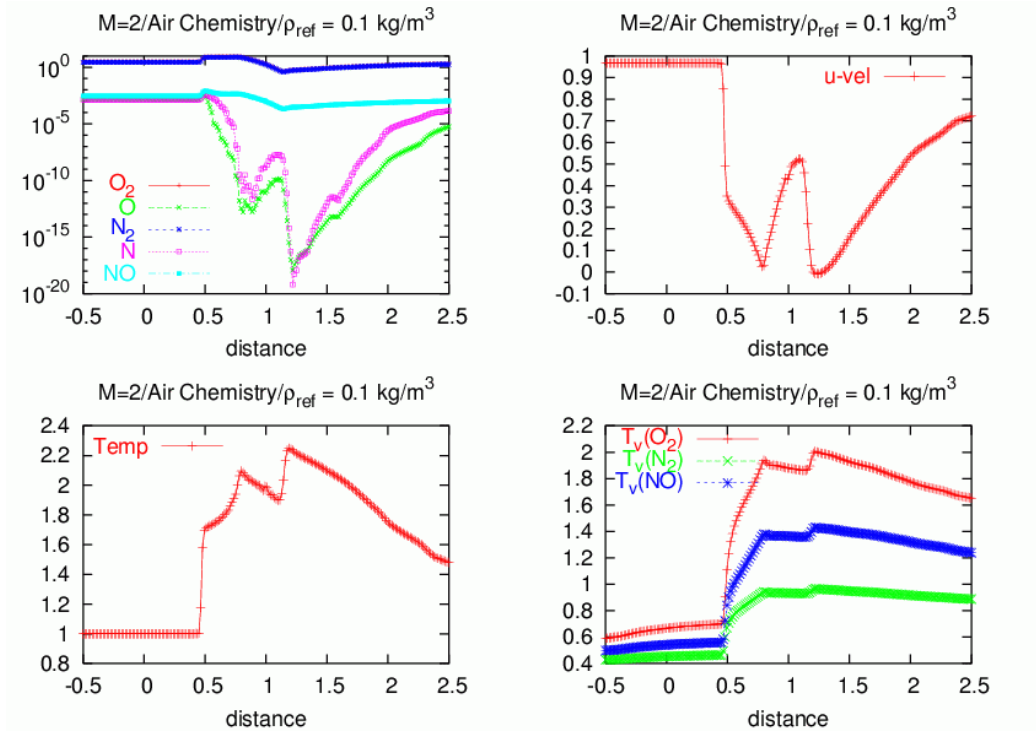
Figure 92 Distributions of species density, u-velocity, translational and vibrational temperature of different molecules along the central streamline.

In order to validate UFS for 1D SW structure, we have carried out simulations similar to those presented by Surzhikov [81] for 1D SW structure in reacting air. Simulations are performed only for the region behind the SW since it is difficult to impose correct boundary conditions at the SW boundaries for a reacting mixture taking into account the vibrational energies. The results in Ref. [81] are for high-speed flows of 11.36 km/s when the temperature in the SW jumps up to 60000 K. We have carried out simulations of SW structure behind the SW front for $M = 15$ and temperature jump of about 10,000 K. The results are presented in Figure 93. One can see that all 3 vibrational temperatures T_v equilibrate within a distance of about 10 cm. The species densities also change over the same distance. Simulations for higher temperatures (such as those in Ref. [81]) will require a more robust chemistry module, which will account for very high values of the reaction rates at large temperatures.

8572/F
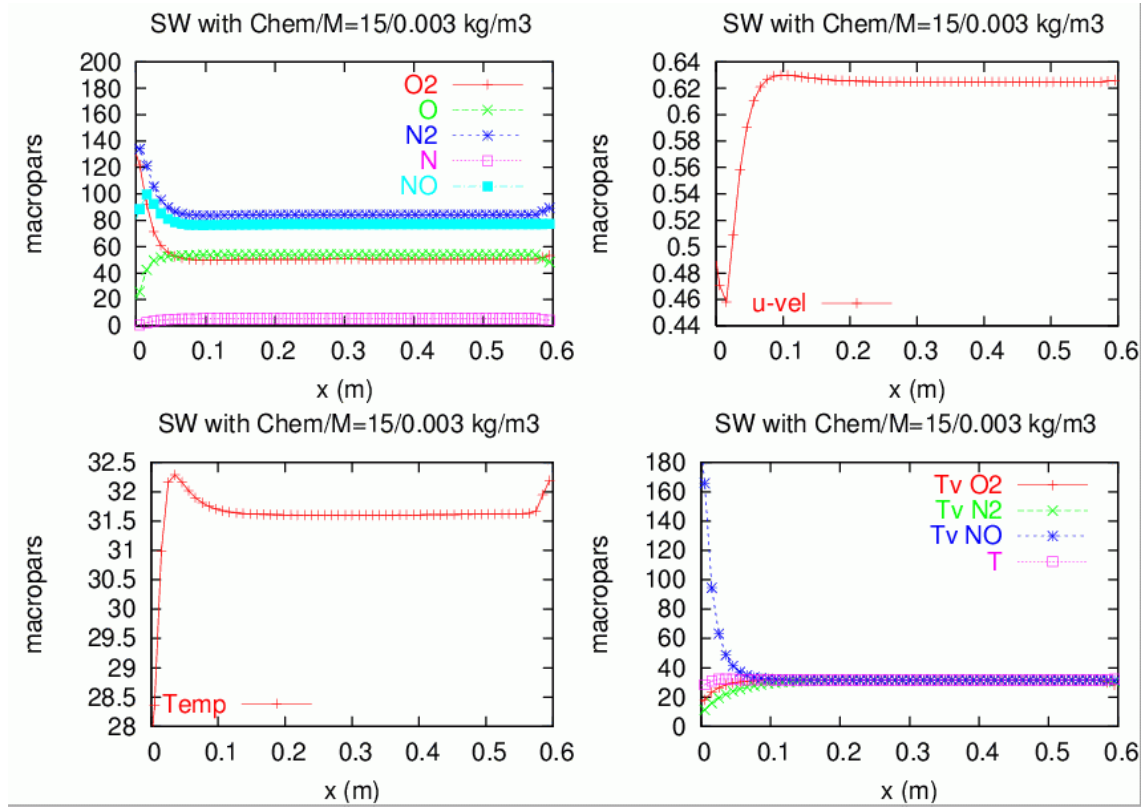
Figure 93 Distributions of species density, u-velocity, translational and vibrational temperature of different molecules for 1D SW structure behind the shock at Mach =15 .

Development of general-purpose chemistry in the UFS framework is planned in the future. We have evaluated the CANTERA code [82] which has established itself as a reliable and user friendly chemistry modeling tool with extensive database for various gas mixtures. We have developed an interface between a UFS-like C code and the CANTERA code and demonstrated feasibility of coupling UFS and CANTERA codes in the future.

6. CONCLUSION

During this Phase II SBIR Project, we have developed a Unified Flow Solver with adaptive mesh and algorithm refinement based on direct numerical solution of the Boltzmann equation coupled to kinetic schemes of gas dynamics. Our strategy allowed easy coupling of the continuum and Boltzmann solvers in a hybrid code with automatic domain decomposition. We have demonstrated the UFS capabilities for several one-component gas flows and confirmed that our hybrid method results in significant savings by limiting expensive kinetic solutions only to the regions where they are needed. We have shown that UFS can automatically introduce or remove kinetic patches to maximize accuracy and efficiency of simulations. We have extended the kinetic solver to molecular gases with rotational and vibrational degrees of freedom. We have also extended the UFS components to reactive gas mixtures. With some extra efforts, it seems feasible to produce an efficient solver for unified simulation of practical problems of polyatomic gas mixtures of different degrees of rarefaction.

7.   PUBLICATIONS

7.1.   Journal Articles

V.I.Kolobov, R.R.Arslanbekov, V.V.Aristov, A.A.Frolova, and S.A.Zabelok, Unified Solver for Rarefied and Continuum Flows with Adaptive Mesh and Algorithm Refinement, J. Comp. Phys. 223 (2007) 589-608

V.I.Kolobov, S.A.Bayyuk, R.R.Arslanbekov, V.V.Aristov, A.A.Frolova, and S.A.Zabelok, Construction of a Unified Continuum/Kinetic Solver for Aerodynamic Problems, AIAA Journal of Spacecraft and Rockets, vol. 42, No. 4, 598 (2005).

7.2.   Conference Presentations

V.I. Kolobov, H.Q. Yang, S.A. Bayyuk, V.V. Aristov, A. Frolova, S. Zabelok, "Unified Methods for Continuum and Rarefied Flows", AIAA-2004-1177, presented at 42nd Aerospace Sciences Meeting and Exhibit. Reno, NV, Jan 5-8, 2004.

V.I.Kolobov, R.R.Arslanbekov, V.V.Aristov, A.A.Frolova, and S.A.Zabelok, Unified Flow Solver for Aerospace Applications, 44th AIAA Aerospace Sciences Meeting and Exhibit, 9-12 January 2006, Reno, Nevada (2005), AIAA-2006-988

V.V.Aristov, A.A.Frolova, and S.A.Zabelok V.I.Kolobov, S.A.Bayyuk, R.R.Arslanbekov, in 24th International Symposium on Rarefied Gas Dynamics, AIP Conference Proceedings, vol **762**, page 96 (2005)

V.V. Aristov, A. A. Frolova, S. A. Zabelok, V. I. Kolobov and R. R. Arslanbekov. Unified Flow Solver Combining Boltzmann and Continuum Models for Simulations of Gas Flows for the Entire Range of Knudsen Numbers. Fourth Int. Conf. on Computational Fluid Dynamics, July 10-14, 2006, Ghent, Belgium.

V.I.Kolobov, R.R.Arslanbekov, V.V.Aristov, A.A.Frolova, S.A.Zabelok, and F.G.Tcheremissine, Unified Solver for Rarefied and Continuum Flows in Multi-Component Gas Mixtures, Rarefied Gas Dynamics: 25 International Symposium, St. Petersburg, Russia, July 2006

V.V.Aristov, A.A.Frolova, S.A.Zabelok, V.I.Kolobov and R.R.Arslanbekov, Simulations of Low Speed Flows with Unified Flow Solver, ibid

S.A. Zabelok, V.V. Aristov, A.A. Frolova, V.I. Kolobov and R.R. Arslanbekov, Parallel implementation of the Unified Flow Solver, ibid

F.G. Tcheremissine, V.I.Kolobov and R.R.Arslanbekov, Simulation of Shock Wave Structure in Nitrogen with Realistic Rotational Spectrum and Molecular Interaction Potential, ibid

R. R. Arslanbekov and V. I. Kolobov, Simulation of Low Pressure Plasma Processing Reactors: Kinetics of Electrons and Neutrals, ibid

V.V.Aristov, A.A.Frolova. The Tang-Toennies potentials for the Boltzmann collision integrals, ibid

V.V.Aristov, V.A.Rykov. The Boltzmann Equation for a Gas with Rotational Degrees of Freedom on the Basis of a Statistical Model, ibid.

E.Josyula, R.R.Arslanbekov, V.I.Kolobov and S.F.Gimelshein, Testing of the Unified Flow Solver for Nozzle and Plume Flows, AIAA-2007-0209.

V.Kolobov, R.Arsanbekov and A.Vasenkov, Coupling Atomistic and Continuum Models for Multi-Scale Simulations of Gas Flows, Y.Sri et al. (Eds):ICCS 2007, Part I, LNCS 4487, pp 858-865 (2007)

V.V.Aristov, A.A.Frolova. S.A.Zabelok, V.I.Kolobov and R.R.Arslanbekov, Multi-Scale Simulations of Gas Flows wit Unified Flow Solver, Y.Sri et al. (Eds):ICCS 2007, Part I, LNCS 4487, pp 850-857 (2007)

R.Arslanbekov, V.Kolobov, A.Frolova, S.Zabelok, Evaluation of Unified Kinetic/Continuum Solver for Computing Heat Flux in Hypersonic Blunt Body Flows, AIAA-2007-4544

8572/F

8. REFERENCES

1   C. Cercignani, *The Boltzmann Equation and its Applications*, Springer-Verlag, (1988)

2   S. M. Yen, Numerical solution of the nonlinear Boltzmann equation for nonequilibrium gas flow problems, Ann. Rev. Fluid Mech. 16, 67 (1984)

3   V.V. Aristov, *Direct methods of solving the Boltzmann equation and study of nonequilibrium flows*, Dordrecht, Kluwer Academic Publishers (2001).

4   G.A.Bird, *Molecular Gas Dynamics and the Direct Simulation of Gas Flows*, Oxford, Clarendon Press (1994).

5   M.S. Ivanov and S.F. Gimelstein, Computational Hypersonic Rarefied Flows, Annu. Rev. Fluid Mech.30, 469 (1998)

6   E.S. Oran et al, DSMC: Recent Advances and Applications, Ann. Rev. Fluid Mech. 30, 403 (1998)

7   A.L. Garcia, et al., Adaptive Mesh and Algorithm Refinement Using Direct Simulation Monte Carlo", J. Comp. Phys. 54, 134 (1999).

8   H.S. Wijesinghe, et al., 3-Dimensional Hybrid Continuum-Atomistic Simulations for Multiscale Hydrodynamics", Proceedings of IMECE 2003 (2003).

9   N. Crouseilles, P. Degond and M. Lemou, Hybrid kinetic/fluid models for non-equilibrium systems, C.R. Acad. Sci. Paris, Ser 1336, 359 (2003)

10   A.E.Beylich, Solving the kinetic equation for all Knudsen numbers, Phys. Fluids 12, 444 (2000)

11   A.E.Beylich, Kinetics of thermalization in shock waves, Phys. Fluids 14, 2683 (2002)

12   P. Le Tallec and F. Mallinger, Coupling Boltzmann and Navier-Stokes Equations by Half Fluxes, J. Comp. Phys. 136, 51 (1997)

13   J.-F. Bourgat, P. Le Tallec, and M.D. Tidriri, Coupling Boltzmann and Navier Stokes Equations by Friction, J. Comp. Phys. 127, 227 (1996)

14   S. Tiwari, Coupling of the Boltzmann and Euler Equations with Authomatic Domain Decomposition, J. Comp. Phys. 144, 710 (1998)

15   A. Klar, H. Neunzert and J. Struckmeier, Transition from Kinetic Theory to Macroscopic Fluid Equations: A Problem for Domain Decomposition and a source for New Algorithms, Preprint

16   S. Tiwari and A. Klar, An adaptive domain decomposition procedure for Boltzmann and Euler equations, J. Comp. Appl. Math. 90, 223 (1998)

17   K. Xu, A gas-kinetic BGK scheme for the Navier-Stokes equations and its connection with artificial dissipation and Godunov method, J. Comp. Phys. 171, 289 (2001).

18   T.Ohwada, S.Fukata, Simple derivation of high-resolution schemes for compressible flows by kinetic approach, J.Comp. Phys 211 (2006) 424

[19] http://gfs.sourceforge.net

[20] S.Popinet, Gerris: a tree-based adaptive solver for the incompressible Euler equations in complex geometries, J. Comp. Physics 190, 572 (2003)

[21] C. Cercignani, The Boltzmann Equation and its Applications, Springer-Verlag, (1988).

[22] S.P.Popov and F.G. Cheremisin, A conservative method for solving the Boltzmann equation with centrally symmetric interaction potentials, Comp. Math. Math. Phys. 39, 156 (1999)

[23] V.V.Aristov, A.A.Frolova. The Tang-Toennies potentials for the Boltzmann collision integrals, Rarefied Gas Dynamics: 25 International Symposium, St. Petersburg, Russia, July 2006

[24] *Lecture Notes on the discretization of the Boltzmann Equation*, Eds.N.Bellomo and R.Gatignol, World Scientific, 2003.

[25] D.B. Goldstein, B.Sturtevant, and J.E. Broadwell,Investigation of the motion of the discrete velocity gases, In *Proceedings of the16th International Symposium on RGD, in Series: Progress in Astronautics and Aeronautics, vol118, Muntz EP et al Eds,* 100 (1989)

[26] C.Buet, A discrete velocity scheme for the Boltzmann operator of rarefied gas dynamics", Trans. Theo. Stat. Phys. 25, 33 (1996)

[27] Rogier, F., and Schneider, J.A., A direct method for solving Boltzmann equation, Transport Theory Stat. Phys., 23 (1-3), pp.313-338, (1994)

[28] Z.Tan and P.L. Varghese , The $\Delta - \varepsilon$ method for the Boltzmann equation, J. Comp. Phys. 110, 327 (1994)

[29] F.G.Tcheremissine, Solution to the Boltzmann Kinetic Equation for High-Speed Flows, Comp Math Math Phys, 46, 315 (2006)

[30] N.N.Korobov, Trigonometric sums and their applications, Mir, Moscow (1898)

[31] P.Degond, L.Pareschi and G.Russo, Eds., Modeling and Computational methods for kinetic equations, Birkhauser 2004

[32] L.Preziozi and L.Rondoli, Conservative Discretization of the Boltzmann Equation and the Semicontinuous Model, in *Lecture Notes on the Discretization of the Boltzmann Equation*, Chapman Hall/CRC Press 2002

[33] C.Buet, S.Gordier, and P.Degond, Regularized Boltzmann operators, Computers Math. Applic. 35, 55 (1998)

[34] D.Gorsch, Generalized Discrete Velocity Models, Mathematical Models and Methods in Applied Sciences 12, 49 (2002)

[35] H.Alsmeyer, Density profiles in argon and nitrogen shock waves measured by the absorption of an electron beam, J. Fluid. Mech. 74, 497 (1976)

[36] E.P.Muntz and L.N.Harnett, Molecular velocity distribution function measurement in a normal shock wave. Phys. Fluids, 12, (1969) 2027-2035.

[37] E.Josyula K.Xu, and D.C.Wadsworth, Testing continuum and non-continuum descriptions in high speed flows, in 24th International Symposium on Rarefied Gas Dynamics, AIP Conference Proceedings **762**, 1217 (2004)

[38] Y.Sone, Kinetic theory and fluid dynamics, Burkhausen, Boston 2002

[39] D.I.Pullin. Direct simulation methods for compressible inviscid ideal gas flow, J. Comp. Phys. 34, 231 (1980).

[40] R.D.Reitz, One dimensional compressible gasdynamics calculations using the Boltzmann equations. J. Comp. Phys. 42, 108 (1981).

[41] V.V.Aristov and F.G.Tcheremissine, Solving the Euler and Navier-Stokes equations on the basis of the operator splitting of the kinetic equations, Doklady USSR Acad. Sci. 272, 555 (1983)

[42] V.V.Aristov and F.G.Tcheremissine, The kinetic numerical method for rarefied and continuum gas flows, In *Rarefied Gas Dynamics*, O.M.Belotserkovskii et al. eds., Plenum Press, N.Y., V.I, p.269 (1985)

[43] V.V. Potkin, A kinetic scheme for gas-dynamic equations in Lagrange coordinates, J. Comp. Math. Math. Phys. 15, 227 (1975).

[44] J.C. Mandal and S.M. Deshpande, Kinetic flux vector splitting for Euler equations, Comput. Fluids 23, 447 (1994).

[45] S.Y. Chou, D. Baganoff, Kinetic flux-vector splitting for the Navier-Stokes equations, J. Comp. Phys. 130, 217 (1997).

[46] T. Ohwada, On the construction of kinetic schemes, J. Comp. Phys. 177, 156 (2002).

[47] T. Ohwada and S.Kobayashi, Management of discontinuous reconstruction in kinetic schemes, J. Comp. Phys. 197, 116 (2004).

[48] C.Kim and A.Jameson, A robust and accurate LED-BGK solver on unstructured adaptive meshes, J. Comp. Phys. 143, 598 (1998).

[49] Q.Li, S. Fu, K. Xu, A compressible Navier-Stokes flow solver with scalar transport, J. Comp. Physics 204, 692-714 (2005)

[50] L. Mieussens, Discrete-Velocity models and numerical schemes for the Boltzmann-BGK equation in plane and axisymmetric geometries, J.Comput. Phys. 162, 429 (2000)

[51] W.J.Coirier, *An Adaptively Refined Euler and Navier-Stokes Solution on an Unstructured Quadtree-Based Grid*, Ph.D. Thesis, Aerospace Engineering Department, The University of Michigan, (1994)

[52] W.J.Coirier, A Cartesian, Cell-Based Approach for Adaptively-Refined Solutions of the Euler and Navier-Stokes Equations", NASA TM 106786 and AIAA-95-0566 (1995)

[53] F.E.Ham, F.S.Lien, and A.B.Strong, A Cartesian Grid Method with Transient Anisotropic Adaptation, J. Comp. Phys., 179, 469 (2002)

[54] G.J.Maslach and S.A.Schaaf, Phys Fluids 6, 315 (1963)

[55] G.Bird, Sophysticated vs simple DSMC, Rarefied Gas Dynamics, Int Symposium (2006)

[56] Q. Li, S. Fu, K. Xu, "Application of Gas-Kinetic Scheme with Kinetic Boundary Conditions in Hypersonic Flow," AIAA Journal 43, 2170 (2005).

[57] J.N.Moss and G.A.Bird, DSMC Simulations of Hypersonic Flows with Shock Interactions", AIAA Journal 43, 2665 (2005)

[58] K.Xu and Z.Li, Microchannel flow in the slip regime: gas-kinetic BGK—Burnett solutions, J. Fluid Mech. 513, 87 (2004)

[59] R.L.Bayut, PhD thesis, MIT 1999

[60] E.Josyula, R.R.Arslanbekov, V.I.Kolobov and S.F.Gimelshein, Testing of the Unified Flow Solver for Nozzle and Plume Flows, AIAA-2007-0209.

[61] K.Morinishi, Computers & Fluids, 70 303 (2005)

[62] J.N.Moss et al, Low-Density Aerodynamics of the Inflatable Reentry Vehicle Experiment (IRVE), AIAA Paper 2006-1189

[63] O M Belotserkovskii, A M Oparin, and V M Chechetkin, *Turbulence: New Approaches*, Cambridge International Science Publishing (2005)

[64] I.N. Larina and V.A. Rykov, Investigation of the Rarefied Gas Flow around a Circular Cylinder in Stationary and Oscillatory Regimes, Fluid Dynamics **41**, 152 (2006)

[65] P.Andreis, K.Aoki and B.Pertrame, A consistent BGK-type model for gas mixtures, Journal of Statistical Physics 106, 993 (2002)

[66] E.Goldman and L.Sirovich, Equations for gas mixtures, Phys Fluids 10, 1928 (1967)

[67] V.V Aristov, A Steady State, Supersonic Flow Solution of the Boltzmann Equation. Phys. Letters A. **250** (1998) 354-359

[68] M.N.Shneider, Neutral molecular beam formation and deceleration induced by optical lattices, RGD 25 Proc, St Petersburg, Russia, 2006.

[69] S.Kozuge, K.Aoki, S.Takata, Shock-Wave structure for a binary gas mixture: finite-difference analysis of the Boltzmann equation for hard-sphere molecules, Eur. J. Mech. B 20, 87 (2001)

[70] A.Raines, European J. Phys. B 21, 599 (2002)

[71] R.R.Arslanbekov and V.I. Kolobov, Simulation Low Pressure Plasma Processing Reactors, Rarefied Gas Dynamics: 25 International Symposium, St. Petersburg, Russia, July 2006

[72] F.G.Cheremisin, Doklady Physics 47, 872 (2002)

[73] F. Robben and L. Talbot, Experimental Study of the Rotational Distribution Function of Nitrogen in a Shock Wave, Phys. Fluids 9, 653 (1966)

[74] K.Koura, Direct simulation Monte Carlo study of rotational nonequilibrium in shock wave and spherical expansion of nitrogen using classical trajectory calculations. Phys. Fluids, 14, 1689 (2002).

[75] V.A.Rykov, V.A.Titarev and E.M.Shakhov, J. Comp. Math. Math. Phys..47, 144 (2007)

[76] C. Cai, D. Liu and K. Xu Non-equilibrium Shock Structure Computation with a Kinetic BGK Scheme, AIAA-2007-609

[77] R. Yano, K. Suzuki and H. Kuroda, "Formulation and numerical analysis of diatomic molecular dissociation using Boltzmann kinetic equation", Phys. Fluids **19**, 017103 (2007).

[78] E. Josyula, D. Gaitonde and J. Shang, "Non-equilibrium hypersonic flow solutions using the Roe Flux-Difference Split Scheme," AIAA 91-1700

[79] R.R.Arslanbekov, V.I.Kolobov, A.Frolova, S.Zabelok, and E.Josyula, AIAA-2007-4544

[80] E.Josyula and W.F.Bailey, J. Spacecraft Rockets 40, 845 (2003)

[81] S. Surzhikov, I. Sharikov, M. Capitelli and G. Colonna, Kinetic Model of Non-Equlibrium Radiation of Strong Air Shock Waves, AIAA 2006-586.

[82] http://www.cantera.org/

8572/F